ELDOR Spectroscopy on Co-Chaperone DnaJ and BLUF Domain BlrB

Im Fachbereich Physik der Freien Universität Berlin
eingereichte Dissertation

vorgelegt von
Richard W. W. Brosi

Fachbereich Physik der Freien Universität Berlin
Mai 2012

Erster Gutachter: Prof. Dr. Robert Bittl
Zweiter Gutachter: Prof. Dr. Peter Hegemann
Tag der mündlichen Prüfung: 4. Juli 2012

Zusammenfassung

Proteine sind eine Grundlage für die Entwicklung von Leben. Durch ihre vielfältigen strukturellen und chemischen Eigenschaften ermöglichen sie die Bildung verschiedenster biologischer Organismen. Kenntnis der Struktur eines Proteins ist eine wertvolle Basis für die Erforschung seiner Funktion. Proteinkristallstrukturen können mit sehr hoher Auflösung ermittelt werden, aber sie bilden nicht immer den Proteinzustand in Lösung ab. Um von der Kristallstruktur Rückschlüsse auf Mechanismen ziehen zu können, ist es hilfreich, seine Anordnung in Lösung zu kennen und somit eventuelle Konformationsänderungen bestimmen zu können. Durch Anbringen von paramagnetischen Spinmarkierungen an bestimmten Positionen des Proteins kann man mit Elektronen Paramagnetischer Resonanz (EPR) durch deren selektive Wechselwirkung auf die Lösungsstruktur zurückschließen, was im Rahmen dieser Arbeit angewandt wurde.

DnaJ aus *Thermus thermophilus* ist Teil eines Hitzeschutz-Systems, das es diesem Bakterium ermöglicht, bei bis zu 75°C zu überleben. DnaJ identifiziert andere, beschädigte Proteine und stimuliert daraufhin die Reparaturaktivität seines Chaperon-Partners. Zusammen formen sie außerdem einen Speicherkomplex, der sich bei Hitzeeinfluss sofort zersetzt und direkt eine hohe Reparaturaktivität der Komponenten ermöglicht. Im Rahmen dieser Arbeit wurde DnaJ im Vergleich zu einer kürzlich gewonnenen Kristallstruktur untersucht und geprüft, ob sich ein Unterschied zwischen dem Protein in Lösung und im zusammengesetzten Komplex ergibt. Es äußert sich Variabilität der Quartärstruktur sowohl für isoliertes DnaJ als auch für im Komplex gebundenes.

BlrB ist ein lichtempfindliches Flavoprotein aus dem Purpurbakterium *Rhodobacter sphaeroides*. Mit seinem Flavinkofaktor, einem häufig in der Natur anzutreffenden Molekül (Vitamin B_2 ist Ribo-Flavin), durchschreitet es einen reversiblen Zyklus der Lichtanregung, der im aktiven Zustand die Farbe des Chromophors leicht verändert. Dies ist ein Hinweis auf eine Reorientierung der polaren Wechselwirkungen in seiner Bindungstasche. Die Motivation dieser Arbeit liegt zum Einen in der sterischen Überprüfung der vorhandenen Kristallstruktur in Lösung und zum Anderen in der Untersuchung des Einflusses der Lichtreaktion auf die äußere Konformation des Proteins. Aus den gewonnenen Erkenntnissen wurde ein Modell für den Prozess der Signalweitergabe in BLUF-Domänen erarbeitet.

Abstract

Proteins are building blocks of life. By their interaction with one another, they make most complex and diverse biological organisms possible. Knowledge of a protein's structure is a valuable basis for investigation and interpretation of its function. Most often, such information is attained by X-ray crystallography. This, however, does not always represent the protein's state in solution, as it is found within a cell.

To be able to understand the protein mechanism it is necessary to examine, which parts of this structural model are conserved in solution and whether there are crucial differences in its conformation. With the aid of paramagnetic spin probes attached to specific protein sites, electron paramagnetic resonance (EPR) provides a snapshot of the protein's solution ensemble. EPR has been utilized in this work to examine two different proteins, *Thermus thermophilus* DnaJ and *Rhodobacter sphaeroides* BlrB.

DnaJ is part of a heat chaperone system that identifies and repairs other damaged proteins, its cognates are found in prokaryotes as well as in eukaryotes including humans. In this work, a recently obtained crystal structure of *Thermus thermophilus* DnaJ is scrutinized and it is examined whether the formation of a stable standby complex specific to this organism leads to conformational changes in DnaJ that could point at its substrate interaction mechanism. The structure of the examined domains is found relevant, but the orientation of the domains is different and indicates unspecific, hydrophobic substrate interaction.

BlrB is a photosensing BLUF protein using a flavin cofactor that is very common in nature (vitamin B_2 is ribo-flavin). It undergoes a reversible photocycle that slightly rearranges the hydrogen bond network of its binding pocket in the excited state. The purpose of this work is to review the protein's available crystal structure and to study, in how far the light activation has an effect on the protein's tertiary structure. On the basis of this experimental information and in correlation with literature data, a mechanism for the signal transduction in BLUF proteins is proposed.

Contents

Chapter 1

Introduction

Proteins are building blocks of life. By means of their structural and chemical properties, they allow for the most diverse and complex reactions to constitute any biological organism. Knowledge of a protein's structure is a valuable basis for investigation and interpretation of its function. This structure is most often and to highest precision attained by X-ray crystallography. This, however, does not always represent the protein's state in solution as it is found within a cell.

To be able to understand the protein mechanism it is necessary to examine, which parts of this structural model are conserved in solution and whether there are crucial differences in its conformation. With the aid of paramagnetic spin probes attached to specific protein sites, electron paramagnetic resonance (EPR) provides a snapshot of the protein's solution ensemble. EPR methods have been utilized in this work to examine two different proteins.

For protein-protein interactions like those between chaperones and their substrate or inter-domain reactions in biological systems like blue-light sensors[1], it is inherently difficult to assign complete structural conformations by crystallography, as the compressed crystal conditions often do not allow the protein to maintain its active quaternary structure conformation. Out of this reason, the crystallization of complete full length protein often is not even possible, but only separate domains can be processed. In all these cases, explicit knowledge of the solution structure is necessary to understand the signal transduction mechanisms or the repair reaction parameters.

This work is focused on the analysis of spin labeled protein samples with Electron Double Resonance (ELDOR) spectroscopy, an EPR method for detection of the distance dependent interaction between two electron spins, and its subsequent conclusions on the protein structure in solution. As the dipolar interaction between two paramagnetic centers is distance dependent ($\omega \propto 1/r^3$), the measurement of their interaction determines specific interspin distances within a protein in its solution ensemble. To attach the necessary spin probes for this research, double or single cysteine mutants, which offer a specific binding site for paramagnetic spin labels, have been expressed by coworkers.

Research was performed on two biological systems, the first of which is *Thermus thermophilus* (*T. thermophilus*) DnaJ, part of the DnaJ/DnaK heat chaperone system that helps this bacterial organism to survive at temperatures of 75°C. It identifies other damaged proteins and consequentially stimulates its repair chaperone partner. Its cognates are found in prokaryotes as well as eukaryotes including humans and they provide necessary conditions for refolding of denatured substrate protein in watery surrounding[2]. In *T. thermophilus* in the presence of a specific assembly factor DafA, they additionally form a precursor complex, which readily dissociates upon heat stress to instantly provide sufficient repair capability.

A recently obtained crystal structure of DnaJ shows its domains in a defined conformation. In other organisms the central region, called the GF-domain for its most predominant residues, was seen in complete disorder and still retains functional relevance, namely in defining the substrate specificity of DnaJ. It is therefore necessary to investigate this protein in its watery solution ensemble to determine the physiological relevance of the crystal structure conformation. A subsequent analysis of the storage complex formed between DnaJ and DnaK in the presence of an assembly factor DafA can demonstrate in how far DnaJ changes its conformation therein.

A BLUF domain (from Blue Light sensing Using Flavin) is a protein domain susceptible to light which binds a flavin cofactor, an organic molecule very common in nature. The domain undergoes a reversible photocycle that slightly changes the cofactor's color, indicating a rearrangement of its binding pocket

in the excited state. The BLUF domains' light reaction to the active state of the cofactor binding pocket is subject of intense research.

The purpose of this part is to review the available crystal structure of the isolated BLUF domain BlrB from *Rhodobacter sphaeroides* (*R. sphaeroides*) and to study, in how far the completed light activation has an effect on the protein's tertiary structure. Such information would be valuable for the study of the different BLUF domain's further signal transduction pathway, which is not yet fully understood. In another organism, where the BLUF domain is linked to a C-terminal effector associated with cyclic nucleotide signaling, a quaternary rearrangement is suggested by crystallography and mutation studies[3]. It is thus essential to investigate BlrB[4] in its solution ensemble by ELDOR spectroscopy and also to examine possible conformational changes upon illumination.

In a nutshell, the aim of this work is to determine whether the observed GF-domain conformation of DnaJ is relevant in solution and in how far the assembly into a complex with DnaK and the DafA substrate affects GF as well as the rest of DnaJ. For BlrB, the evaluation of the crystal structure and the measurement of the protein's light state conformation are means to propose a mechanism of signal transduction.

At first, a brief account of the current knowledge about both biological systems with respect to the focus of this work is given in chapter 2. Subsequently, an explanation of the interactions between electron spins and their surrounding follows, which is the foundation for EPR spectroscopy (chapter 3). Chapter 4 expands on the experimental procedures of EPR and ELDOR spectroscopy as well as illustrates the properties of the biological samples. It also describes how to interpret the ELDOR experiments, which are the fundamental results of this work. They are presented and discussed in a separate chapter for each system, DnaJ in chapter 5 and BlrB in chapter 6. Finally, a short summary concludes the thesis.

Chapter 2

Biological Systems

2.1 DnaJ

Bacterial DnaJ proteins and their eukaryotic homologs Hsp40 (Heat shock protein 40) are essential partners of the DnaK/Hsp70 chaperone proteins and are geminately preserved in prokaryotes[2,5] as well as in eukaryotes including mammals and humans[6,7,8]. Functionally diverse species of this chaperone machinery have been found in nearly all cell components, the cytosol, inside the mitochondria, in the nucleus or in the endoplasmic reticulum[9,10].

The central function of DnaK/Hsp70 is to bind selectively to hydrophobic areas of unfolded or denatured protein substrate of different origin. In this state, it facilitates correct folding of nascent polypeptide substrate during ongoing translation[11] or prevents the aggregation of the protein substrate by reducing its free concentration[7,12]. As a stress response to heat shock or other disruptive factors, the strong chaperone-substrate interaction alleviates refolding of denatured proteins[9,13,14]. In some cases, it provides safe transport of the hydrophobic substrate from the ribosome to other parts of the cell within the process of cell growth[15].

However, DnaK/Hsp70 cannot catalyze this reaction by itself as it is lacking the necessary ATPase activity and without ATP cleavage, DnaK remains in a closed conformation with lower affinity and high exchange rates for apolar substrates[17]. Its co-chaperone DnaJ activates the DnaK ATPase turnover and thus enables it to undergo a conformational change to an opened form, which has the

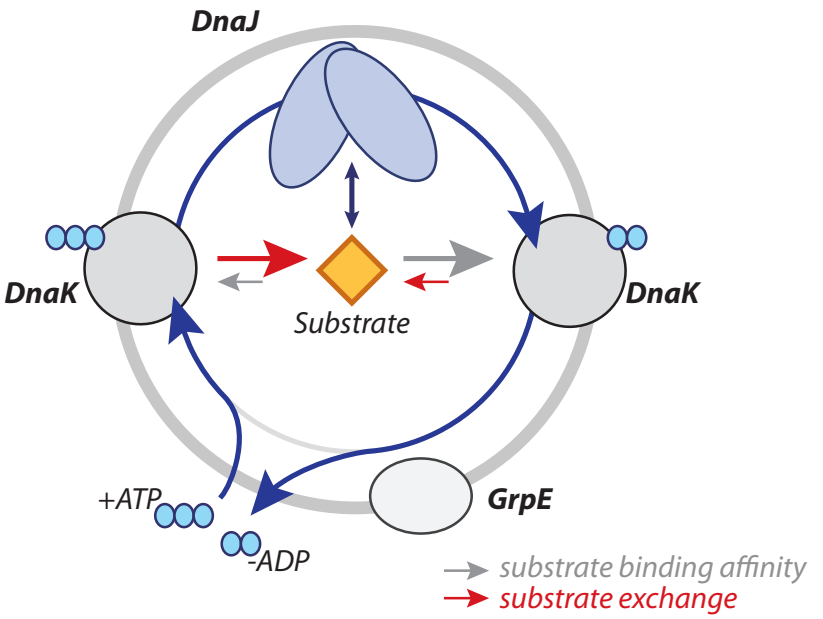

Figure 2.1: *Illustration of the putative DnaK/DnaJ/GrpE chaperone cycle, originally from Bukau 1998[16]. To the left, DnaK has a high binding and exchange rate with the substrate. DnaJ activates DnaK's ATPase activity allowing the substrate to bind tightly and to refold. Afterwards, GrpE triggers the release of ADP, so new ATP can be bound and the substrate can be released.*

aforementioned effects on the substrate[18]. The whole cycle (figure 2.1) is then completed by DnaK's interaction with GrpE, a second co-chaperone that facilitates nucleotide exchange in DnaK[19,20]. Release of the bound protein with reversion to the closed state is the consequence[16,21]. DnaJ's stimulation of DnaK's ATPase activity is dependent on the presence of a suitable substrate. The actual mechanism of its identification by DnaJ remains elusive, while its biological effect is well investigated[10,22,23,24].

To achieve full folding efficiency on strongly denatured proteins or nascent peptides, several DnaK activity cycles are required. Thus, the selectivity of this chaperone system is mainly achieved by the specificity of the corresponding DnaJ. There are certain DnaK proteins that are paired with different DnaJ partners in different types of tissue, which alters the target protein substrate to which the system is specific[25,26].

DnaJ/Hsp40 has been classified into three types based on sequence criteria. The DnaJ proteins discussed in this work are of type II and consist of three domains, Type III DnaJ has an additional zinc binding motive and type I DnaJ omits the linker region between the N- and the C-terminal domains. No complete structural information of any DnaJ is available to this date.

The N-terminal domain of DnaJ is called J-domain. Several NMR-structures of this domain from *E. coli* DnaJ[27,28] as well as human Hsp40[29] exist. It has been found to contain the binding interface to DnaK and be responsible for the stimulation of ATPase activity[12,30]. It also has been implicated as a factor for DnaK specificity[31].

The C-terminal domain of DnaJ forms a V-shaped homodimer as seen by X-ray crystallography and it directly interacts with the substrate[32,33]. It is presumed to carry an influence on the structural rigidity of the N-terminus as compared to isolated J-domain in *E. coli*[34].

The linker domain is the major point of interest for this work, as it has been found completely disordered by NMR experiments[27,28,35,36], but responsible for DnaJ/Hsp40's substrate specificity in yeast[37] as well as for the modulation of ATPase activation in *E. coli* DnaK[38]. It contains a Glycine-Phenylalanine-rich motive and hence is called GF-domain.

DnaJ from *Thermus thermophilus* (*T. thermophilus*), an extremely heat tolerant bacterium, is investigated in this work. In this organism, functionality must be achieved at very high temperatures (75°C). In consequence, *T. thermophilus* DnaK in itself has weak ATPase activity, which nevertheless is substantially enhanced by its DnaJ co-chaperone[5,21,39,40]. The formation of a precursor/storage complex between DnaJ and DnaK in the presence of the small DnaJ-assembly factor A (DafA) furthermore enables fast stress response. DafA denatures from heat shock and loses its conformation to which DnaJ and DnaK have high affinity. The complex dissociates and thus, the DnaJ/DnaK system can instantly bind to other proteins (see figure 2.2).[41] As DnaK substrate binding and complex formation are competing effects, an increased concentration of DafA in the cell medium effectively reduces the amount of substrate bound[21,39,41,42].

If the mechanism leading to the complex formation could be understood in more detail, it has the potential to be used on cognate Hsp40/70 systems as drug delivery system. In recent research, the loss of Hsp70 was reported to aggra-

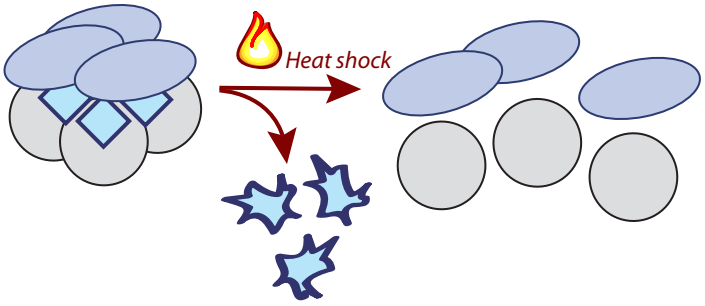

Figure 2.2: *Heat shock destroys the precursor complex, thus rendering both DnaJ and DnaK able to bind/select other denatured proteins in the cell medium. Taken from Watanabe 2004*[41].

vate pathogenesis in neurodegenerative diseases[43], even though no increase in fibrillar aggregates, the presumed cause of the disease, has been observed[44].

2.2 BlrB

BLUF domains (Blue Light Using Flavin) are one of three predominant flavin based blue light sensor families alongside photolyases/cryptochromes and phototropins/LOV domains (from Light-Oxygen-Voltage)[1,45].

Several BLUF domain X-ray structures have been reported[3,4,46,47,48,49,50]. All have in common a central β-sheet with five strands and two parallel α-helices constituting the flavin binding pocket. The flavin binds with its isoalloxazine moiety between α_1 and α_2. The conformation of the C-terminal part is different in different organisms, but is mostly of helical structure and located on the other side of the β-sheet.

BLUF domains have been identified as key sensors for photoavoidance reactions in the cyanobacterium *Synechocystis* as well as in the unicellular organism *Euglena gracilis*[51]. They were originally found in the purple proteobacterium *Rhodobacter sphaeroides* (*R. sphaeroides*)[52,53]. This organism can perform photosynthesis under oxygen deprivation when its AppA-BLUF domain (from Activation of Photo-pigment and PUC expression A) initiates anti-repression of photosynthetic gene expression upon light activation. *R. sphaeroides* also pos-

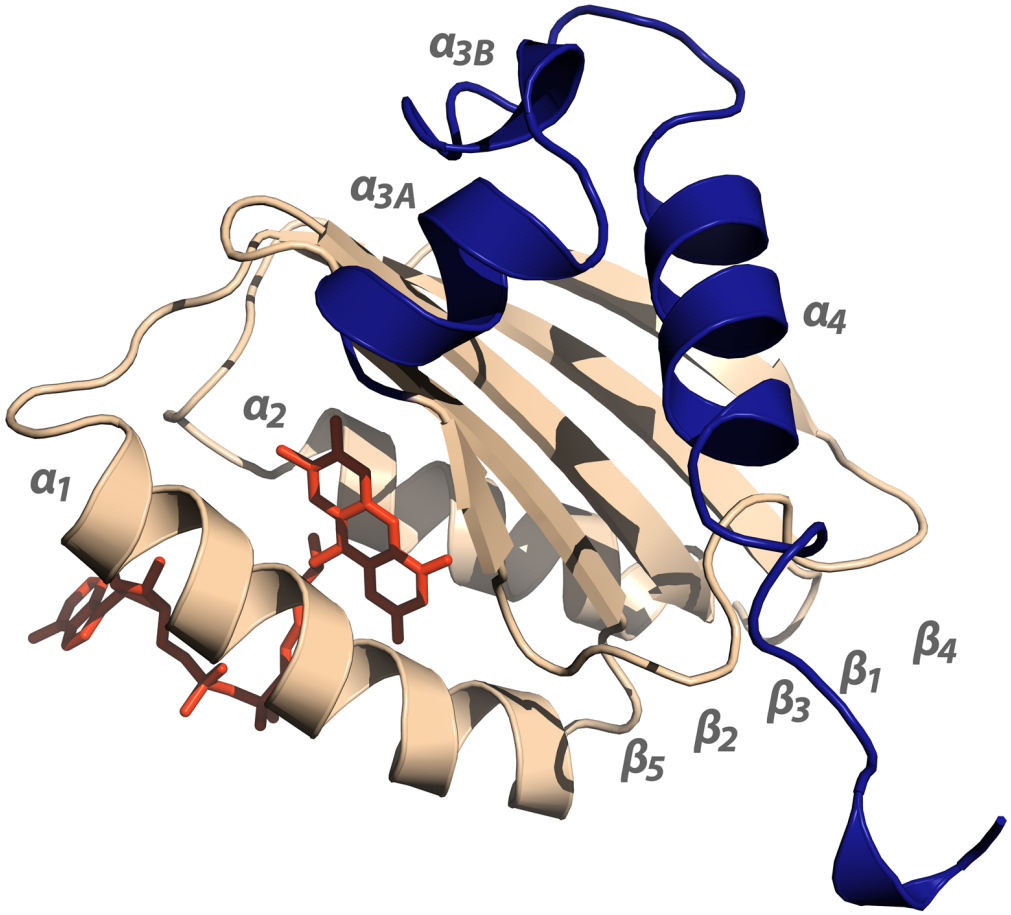

Figure 2.3: *Crystal structure of* R. sphaeroides *BlrB (PDB 2BYC). It consists of 140 amino acids forming a five stranded beta sheet and two parallel helices (the 'Body', wheat) and a C-terminal predominantly helical appendix (the 'Tail', blue). Inside the cavity between* α_1 *and* α_2*, it incorporates either Riboflavin, FMN or mostly FAD (red). The molecular weight is 16.4 kDa for the protein including the FAD cofactor.*

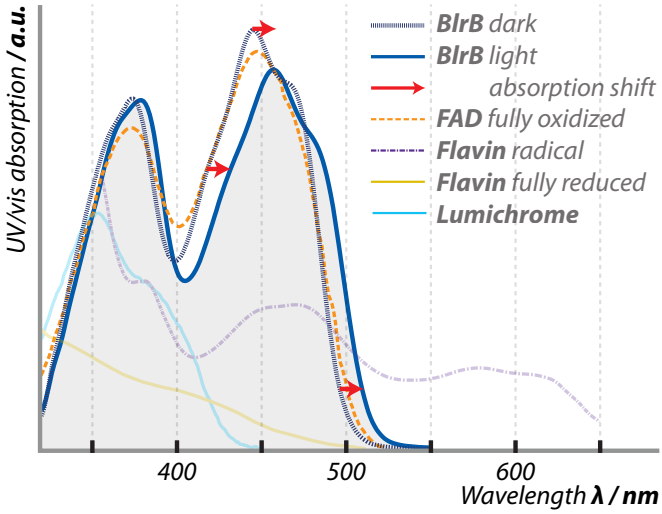

Figure 2.4: *UVvis spectra of BlrB in dark and light state, clearly showing the red-shift of the right absorption band. Reference spectra of unbound flavin in different oxidation states are shown in addition. (Taken from Zirak 2006[58].)*

sesses two additional BLUF domains, BlrA and BlrB (from Blue light receptor A/B). The function of their signaling capability is yet unknown. For BlrB, its C-terminal domain has been found crucial to the protein's structural integrity,[54] but in contrast to AppA, where structural information on the dark resting state as well as a light activated form are available[55], BlrB could only be examined by crystallography in its dark state[4]. BlrB is subject of the second part of this work, its crystal structure is depicted in figure 2.3.

A variety of BLUF domains has been discovered, predominantly in prokaryotes[1,56]. Several are directly linked to effector domains like in *Klebsiella pneumoniae* BlrP1, which comprises a BLUF domain and an EAL phosphodiesterase domain at its C-terminus[3] or the photoactive adenylyl cyclase (PAC) from *Euglena gracilis*[51]. These effector domains are involved in the signaling cascade by cyclic nucleotide second messengers. Other isolated BLUF domains (which contain no effector domain) form oligomers, even involving 10 to 15 monomers of *Synechocystis* PixD (also known as Slr1694)[50] and PixE (Slr1693), which dissociate into smaller units upon blue light illumination[57].

In BLUF domains, the illumination with blue light causes the absorption band

centered at 450 nm of the fully oxidized, bound flavin to red-shift as shown in figure 2.4. The mechanism leading to this light induced change is still under debate, but it involves a short lived radical pair intermediate consisting of an anionic flavin radical and an oxidized amino acid[59,60]. The cofactor most likely receives the electron from a nearby, highly conserved tyrosine (Y9 in BlrB)[61]. In consequence, the hydrogen bond network in the flavin binding pocket is reorganized[62]. The actual absorption shift is probably caused by a change of the hydrogen bonds between the flavin C_4=O-group and a glutamine residue (Q51 in BlrB). This residue either undergoes a half turn flip of its amide group[48] or a tautomerization of its carbonyl to a hydroxyl group[63]. Then, a proton is transferred from the tyrosine residue[64], reoxidizing the flavin cofactor and concluding the light-induced reaction.

The active signaling state varies considerably in stability from organism to organism. Decay times from seconds for BlrB to 17 minutes in AppA are documented.[58,65] The changed conformation also has repercussions on the overall structure of the protein. Wu 2008/2009[47,54] and Grinstead 2006[49] observed changes in the beta sheet and C-terminus of BlrB, BlrP1 and AppA with NMR, respectively.

A related issue is the position and function of methionine and tryptophan in β_5 (W92 and M94 in BlrB) on the pyrimidine side of the flavin. The tryptophan has been found in two different conformations in AppA[55] and in Slr1694 crystals[50], one of which is inside the binding pocket, the other surface-oriented. It has been speculated whether the methionine and the tryptophan residues switch places upon light activation. In subsequent mutation studies, the tryptophan residue could be rejected as essential partner for the successful light activation of the flavin chromophore[66]. It could still be a steric factor for the C-terminal conformation, though.

Flavin Cofactor

Flavins are ubiquitous in nature. On the basis of vitamin B_2 (riboflavin), the common cofactors FMN (flavin mononucleotide) and FAD (flavin adenine dinucleotide) are formed (see figure 2.5). BLUF domains are functional with any of the three flavin identities as extensions of the ribityl side chain are not necessary

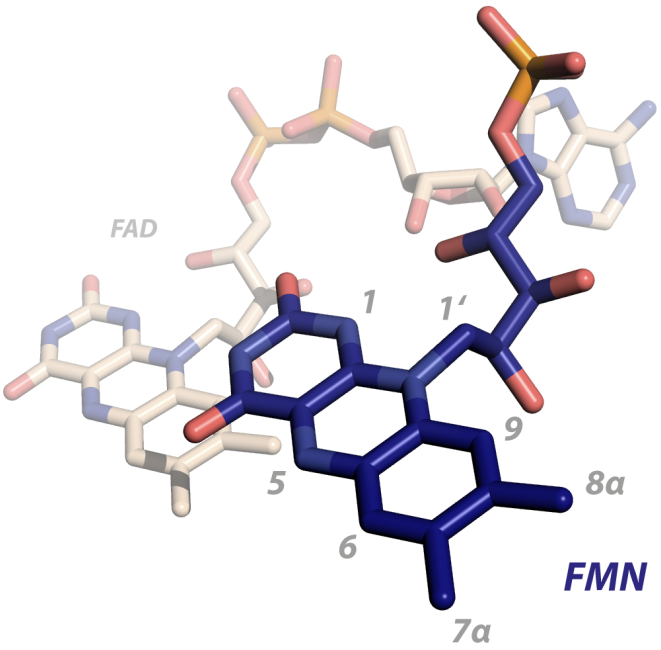

Figure 2.5: *Flavin Mono Nucleotide (FMN, blue) with its UIPAC numbering, beginning at the isoalloxazine ring, and denoting the ribityl side chain with a hyphen. Nitrogens are at positions 1, 3, 5 and 10, oxygens (red) are bound to C_2 and C_4 as well as to several carbons in the ribityl chain. The phosphate group at its end can be attached to an adenine nucleotide, forming Flavin Adenine Dinucleotide (FAD, in background).*

for its function in these proteins[67].

Flavin can undergo a wide variety of redox reactions as it can exist in three different redox states: the fully reduced hydroquinone form, the radical semiquinone form and the fully oxidized state. Furthermore, the semi- and hydroquinone forms have two different physiologically relevant protonation states[68,69]. The different redox states of flavin are of distinct color. While the fully oxidized flavin is of strong yellow color, the semiquinone radical form is deep purple, the anionic radical red and the fully reduced state is again yellow, but very pale. The distinct color difference of the neutral semiquinone stems from an additional broad absorption feature between 500 and 630 nm (see 2.4).

The illumination of a flavin cofactor stimulates the transition into an excited state (FMN*/FAD*), which is an exceedingly potent electron acceptor. Therefore, such a light activation commonly causes an electron transfer to the flavin,

thus produces a radical intermediate. This metastable radical state then leads to the formation of a covalent bond in LOV domains[70], to a different redox state in photolyases and cryptochromes or the said reconformation of the binding pocket in BLUF causing the absorption red-shift of the again fully oxidized flavin. The latter demonstrates the cofactor's high sensitivity for changes in its environment, which also has been demonstrated for its semiquinone form by EPR in *Avena sativa* LOV2[71].

Its abundance in living organisms makes BLUF proteins and other flavin based protein domains a promising system for optogenetics, as the cofactor can be readily incorporated into proteins such BLUF proteins expressed by a living organism on the basis of artificially introduced genes. Successful studies have used artificially inserted photoactivated nucleotidyl cyclases[72,73,74], with a BLUF domain at its N-terminus.

Chapter 3

EPR

The following chapter provides the fundamental theory of EPR with a focus on those interactions which are relevant for this work in conjunction with their effect on experimental realization. Several excellent volumes about EPR, especially pulsed EPR, like Schweiger and Jeschke[75], Carrington and McLachlan[76] or Weil, Wertz and Bolton[77] can expand further on the details of this method.

Paramagnetic species possess a permanent magnetic dipole moment as a consequence of the spin angular momentum of an unpaired electron. In an external magnetic field the projection of any angular momentum along the field axis is quantized[78], the resulting energy splitting is subject to the Zeeman effect[79].

With Electron Paramagnetic Resonance (EPR), which first was used by Zavoisky as a spectroscopic method in 1944[80,81], it is possible to investigate the transitions between these different energy levels that follow the resonance condition

$$h\nu = g_e \mu_B |\boldsymbol{B}_0| \tag{3.1}$$

for a free electron. $h\nu$ is the transition energy, g_e is the free electron g-factor with $g_e \approx 2.002319$[82], $\mu_B = \frac{e\hbar}{2m_e}$ is called the Bohr magneton and $\boldsymbol{B}_0$ the external magnetic field.

3.1 Spin Hamiltonian

In EPR only transitions between different spin states are induced, hence the spin dependent portion of the complete Hamiltonian should be the only contribution to the detected transition energy. Still, in real samples the spatial dependence or the coupling of the spin angular momentum S to the orbital angular momentum L does not vanish. In consequence, one introduces parametric values like the g-matrix. For a system with one electron it is described by the *spin Hamiltonian*

$$\mathcal{H}_0 = \mathcal{H}_{EZ} + \mathcal{H}_{HF} + \mathcal{H}_{NZ}. \tag{3.2}$$

Electron and nuclear spin are subject to the Zeeman effect ($\mathcal{H}_{EZ}$ and $\mathcal{H}_{NZ}$) and the interaction between electron and nuclear spin leads to the hyperfine structure ($\mathcal{H}_{HF}$). $\mathcal{H}_{NZ}$ is small compared to $\mathcal{H}_{EZ}$. Further terms, like the nuclear quadrupole interaction for nuclear spins $I > 1/2$, are not relevant for this work.

For systems with more than one unpaired electron or radical spin, the interaction between them is relevant and the basis for the following experiments. Two spins S_A and S_B have the interaction $\mathcal{H}_{EE}$ in addition to their isolated spin Hamiltonians $\mathcal{H}_0(S_A)$ and $\mathcal{H}_0(S_B)$.

$$\mathcal{H}_0(S_A, S_B) = \mathcal{H}_0(S_A) + \mathcal{H}_0(S_B) + \mathcal{H}_{EE} \tag{3.3}$$

These Hamiltonians show the main advantage of EPR: As there are only one or few radical spins within a studied sample, the restriction to electron spin transitions and their interaction to the surrounding signifies an intrinsic, controllable simplification of the studied system.

Zeeman Interaction

Any angular momentum of charge induces a magnetic dipole moment that interacts linearly with an external magnetic field $\boldsymbol{B}_0$:

$$\mathcal{H}_{EZ} = \mu_B \boldsymbol{B}_0 \mathbf{g} \boldsymbol{S} / \hbar \tag{3.4}$$

The interaction of electron $\boldsymbol{S}$ with the orbital angular momentum $\boldsymbol{L}$ gives rise to the spin-orbit coupling (LS-coupling). It is the reason for deviations

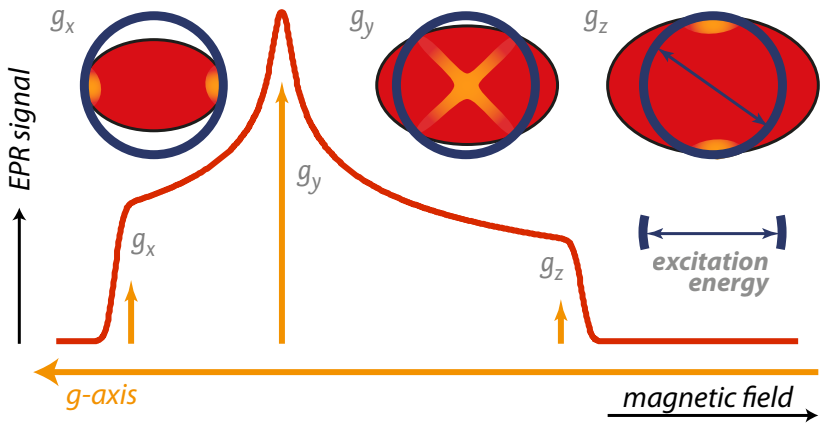

Figure 3.1: *Calculated X-band EPR spectrum of an anisotropic g-matrix (shown as red ellipsoid in the respective Hilbert space). Depending on the magnetic field, different sub populations of the sample are excited. Only at g_z and g_x a single orientation can be isolated, as they are connected with a minimum/maximum energy level splitting. With increasing magnetic field, the ellipsoid grows proportionally according to the Zeeman effect and is intersected by the constant excitation energy sphere at the resonating sub populations shown in orange.*

from the free electron g-factor g_e and is taken into account with the introduction of the orientation dependent $\mathbf{g}$-matrix. The Zeeman interaction is sensitive to variation of the orbital holding the unpaired electron. Influences from the surrounding hydrogen bonds and other effects on this orbital emerge as changes in this $\mathbf{g}$-matrix.

An EPR spectrum of a powder sample is the superposition of spectra for all possible g values in the sample, the relative amplitude is proportional to the excited population (see figure 3.1). If instead the sample is liquid, fast motion of the molecules leads to cancellation of the anisotropy.

$\mathcal{H}_{EZ}$ is the dominant term of the Hamiltonian, thus $\mathbf{g}$ in its diagonal form defines the orientation of the molecular coordinate system, whereas $\mathbf{B}_0 = (0, 0, B_0)$ defines the laboratory frame.

In case of the nuclear Zeeman interaction $\mathcal{H}_{NZ}$, no empiric $\mathbf{g}$-matrix is used, but I and g_n are specific for each nucleus:

$$\mathcal{H}_{NZ} = -\mu_n g_n \boldsymbol{B}_0 \boldsymbol{I}/\hbar \tag{3.5}$$

Protons have a spin quantum number of 1/2 and $g^{^1H} = 5.58$, resulting in the largest nuclear Zeeman interaction of only $0.00152 \times \mathcal{H}_{EZ}$. The nuclear magnetic moments are so much smaller than the electron's due to the nuclear mass. Deuterons (^2H) and nitrogens (^{14}N, natural abundance of $N_{14} = 99.632\%$) have a spin of 1 and $g^{^2H} = 0.847$, $g^{^{14}N} = 0.403$.

Hyperfine Interaction

The hyperfine interaction between the electron and the nuclear spin can be expressed by

$$\mathcal{H}_{HF} = \boldsymbol{S}\mathbf{A}\boldsymbol{I} \tag{3.6}$$

and is split into a sum of the isotropic Fermi contact term $\mathcal{H}_{iso}$ and the electron-nuclear dipole-dipole interaction $\mathcal{H}_{ENdip}$.

$$\mathcal{H}_{HF} = \mathcal{H}_{iso} + \mathcal{H}_{ENdip} \tag{3.7}$$

The isotropic component is

$$\mathcal{H}_{iso} = A_{iso}\boldsymbol{SI} = \frac{2}{3}\frac{\mu_0}{\hbar} g_e \mu_B g_n \mu_n |\Phi_0(r_n)|^2 \boldsymbol{SI}. \tag{3.8}$$

Hence measuring the isotropic couplings of several nuclei which interact with the electron spin yields information on the spatial spin distribution within this radical species. The data can then be correlated to other structural information like a crystal structure.

By use of the correspondence to the classical dipole-dipole interaction we can state

$$\mathcal{H}_{ENdip} = \frac{\mu_0}{4\pi\hbar} g_e \mu_B g_n \mu_n \left(\frac{3(\boldsymbol{Sr})(\boldsymbol{rI})}{r^5} - \frac{\boldsymbol{SI}}{r^3} \right) \doteq \boldsymbol{S}\mathbf{A}_{dip}\boldsymbol{I}, \tag{3.9}$$

where $\boldsymbol{r}$ is the connection vector between the electron and the nucleus. If this interaction is integrated over the whole electronic distribution, all anisotropy is absorbed into the traceless, symmetric coupling matrix $\mathbf{A}_{dip}$.

For different isotopes the complete hyperfine interaction is proportional to the respective g_n assuming constant $\mathbf{A}_{dip}$ (e.g. deuterated samples would have all hyperfine interaction scaled by a factor of 1/6.51 compared to protonated samples).

Electron-Electron Interaction

Weak coupling

The most important interaction for this work is the dependency between two weakly coupled electron spins S_A and S_B, which contains two effects.

$$\mathcal{H}_{EE} = \mathcal{H}_{EEdip} + \mathcal{H}_{exch} \tag{3.10}$$

The dipolar part can be described analogously to the hyperfine interaction (see below). The contact term is replaced by the Heisenberg exchange, as two electrons coming into close overlap have the possibility for exchange.

$$\mathcal{H}_{exch} = -2J\boldsymbol{S}_A\boldsymbol{S}_B \tag{3.11}$$

Within proteins, it can be approximated by an exponential $J(r) = J_0 e^{-\beta r}$ with $\beta \approx 15\,\mathrm{nm}^{-1}$. It becomes relevant at distances below 1.5 nm[I] or in case of strong electron de-localization.

$$\mathcal{H}_{EEdip} = \boldsymbol{S}_A\mathbf{D}\boldsymbol{S}_B = -\frac{1}{r^3}\frac{\mu_0}{4\pi\hbar}g_A g_B \mu_B^2 \left(\frac{3(\boldsymbol{S}_A\boldsymbol{r})(\boldsymbol{S}_B\boldsymbol{r})}{r^2} - \boldsymbol{S}_A\boldsymbol{S}_B\right) \tag{3.12}$$

Regarding the dipolar part $\boldsymbol{r}$ is the connection vector between the two electrons. If the electron spins are primarily oriented along $\boldsymbol{B}_0$ so the high-field approximation applies, the dipole-dipole interaction matrix is given in its diagonal form within the lab frame by

$$\mathbf{D} = \frac{1}{r^3}\frac{\mu_0}{4\pi\hbar}g_A g_B \mu_B^2 \begin{pmatrix} -1 & & \\ & -1 & \\ & & 2 \end{pmatrix} = \begin{pmatrix} -\omega_{dd} & & \\ & -\omega_{dd} & \\ & & 2\omega_{dd} \end{pmatrix} \tag{3.13}$$

In a powder sample, all orientations of the interspin vector are present, therefore the observed coupling follows a Pake pattern

$$\mathcal{H}_{EEdip} = \omega_{dd}(1 - 3cos^2\theta)\boldsymbol{S}_A\boldsymbol{S}_B \tag{3.14}$$

[I]The size of $J(1.5\mathrm{nm})$ is already three orders of magnitude smaller than $J(1.0\,\mathrm{nm})$, $J(2.0\,\mathrm{nm})$ already six orders of magnitude. In absolute terms, dipolar interaction is predominant from $r = 1.4\,\mathrm{nm}$ and above.

with θ as the angle between the external magnetic field and the interspin vector $\boldsymbol{r}$. Thus, even in absolutely rigid molecules with two spins, a distribution of resonance frequencies is observed. This dipolar broadening is strongly dependent on the interspin distance r and can be used for evaluation of $r < 1.5\,\mathrm{nm}$ but is safely neglected above 1.8 nm. A typical weakly coupled sample like a doubly nitroxide labeled protein with $r > 1.8\,\mathrm{nm}$ will have field independent contributions to the Hamiltonian which are governed by $\mathbf{A}_{dip}$ anisotropy. Figure 3.7 shows a comparison of isolated dipolar Pake patterns for different r to a nitroxide X-band EPR spectrum ($\nu \approx 9.4\,\mathrm{GHz}$).

Under the further assumption of $g_A = g_B = g_e$ and $\nu_{dd} = \frac{1}{T_{dd}} = \frac{\omega_{dd}}{2\pi}$, one can simplify equation 3.13 to a direct relation between the observed dipolar frequency ω_{dd} and the distance r between the A and B spin.

$$r \approx \sqrt[3]{\frac{52.0\mathrm{MHz}}{\nu_{dd}}}\mathrm{nm} = \sqrt[3]{52.0\frac{T_{dd}}{\mu\mathrm{s}}}\mathrm{nm} \tag{3.15}$$

Strong coupling: Zero-field splitting

For strongly coupled electron spins the system is described by one group spin $\boldsymbol{S}$ with $\boldsymbol{S} > 1/2$. This is expressed by the fine-structure term

$$\mathcal{H}_{EE} \rightarrow \mathcal{H}_{ZFS} = \boldsymbol{S}\mathbf{D}_{ZFS}\boldsymbol{S}. \tag{3.16}$$

For high spin systems this interaction is often dominant at low fields, but it is not relevant to this work.

3.2 Bloch Equation

To understand the mechanisms of EPR spectroscopy, we employ the pseudo classical description of the sample magnetization and its time evolution. This approach is viable for experiments on large ensembles of spins, as it is the case with all standard EPR spectrometers.

The macroscopic magnetization $\boldsymbol{M}$ is the sum over all molecular magnetic moments $\boldsymbol{M} = \frac{1}{V}\sum \boldsymbol{\mu}$. The time evolution is given by its derivative in the

equation of motion

$$\frac{d}{dt}\boldsymbol{M} = \gamma \boldsymbol{M} \times \boldsymbol{B}_0 \tag{3.17}$$

$$\frac{d}{dt}\boldsymbol{M} = \gamma \begin{pmatrix} M_y(t)B_0 \\ -M_x(t)B_0 \\ 0 \end{pmatrix} \Rightarrow \boldsymbol{M}(t) = R_z(\omega_0 t)\boldsymbol{M}(0) \tag{3.18}$$

This solution describes the rotation or precession of the initial magnetization $\boldsymbol{M}(0)$ with the rotation matrix $R_z(\varphi)$[II] around the z-axis with the Larmor frequency $\omega_0 = g_e \mu_B B_0/\hbar = -\gamma B_0$.

In the presence of an additional time dependent magnetic field of circular polarization with $\boldsymbol{B}_1 = B_1(cos(\omega_{mw}t), sin(\omega_{mw}t), 0), \omega_1 = -\gamma B_1$, which is used to excite the spins, it is most convenient to switch into a new basis system rotating around $\boldsymbol{z} = \boldsymbol{e}_{B_0}$ with ω_{mw}. By introducing the offset frequency $\Omega = \omega_0 - \omega_{mw}$, the Bloch equation in the rotating frame becomes

$$\frac{d}{dt}\boldsymbol{M} = \gamma \begin{pmatrix} -\Omega M_y(t) \\ \Omega M_x(t) - \omega_1 M_z \\ \omega_1 M_y \end{pmatrix} \tag{3.19}$$

If ω_{mw} is not equal to the Larmor frequency ω_0, and thus $\Omega \neq 0$, the Bloch equation describes again an additional precession around $\boldsymbol{z}$, as in the fixed laboratory frame case. Together with $\omega_1 > 0$, it leads to a nutation around an effective field. Its inclination ϑ is determined by the quotient of both frequencies, $\vartheta = tan^{-1}(\omega_1/\Omega)$.

Linearly polarized microwave, which is commonly used in EPR spectrometers, is a superposition of two counter-rotating circularly polarized fields, where only one can be in resonance with the rotating frame, but the other will be off

[II] $R_z(\varphi) = \begin{pmatrix} cos\varphi & -sin\varphi & \\ sin\varphi & cos\varphi & \\ & & 1 \end{pmatrix}$

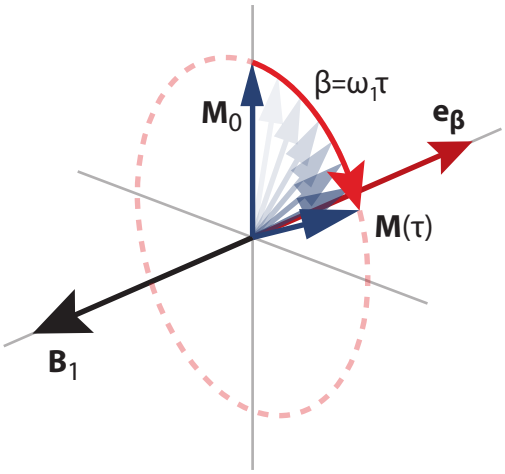

Figure 3.2: *Rotation of the overall magnetization M perpendicular to the B_1 axis of the microwave pulse. The rotation angle β is proportional to the pulse length τ.*

resonant by $2\omega_{mw}$. $\Omega = 2\omega_{mw} \gg \omega_1$ leads to a tiny contribution to ϑ, hence the far off resonant component has a negligible effect on the ensemble magnetization.

In the important on-resonant case, with $\beta = -\gamma B_1 \tau$ and $\Omega = 0$, only a precession around the rotating x-axis $\boldsymbol{e}_{x,rot}$ remains, which is described by the rotation matrix $R_{x,rot}$.[III]

$$\boldsymbol{M}(t) = R_{x,rot}(\omega_1 t)\boldsymbol{M}(0), \frac{\boldsymbol{B}_1}{B_1} = \boldsymbol{e}_{x,rot} \tag{3.20}$$

The axes in the rotating frame will from now on be called $x, rot = x$ and $y, rot = y$ for simplicity.

3.3 Pulsed EPR

By switching the resonant $\boldsymbol{B}_1$ field on and off after a certain time τ, this microwave pulse will rotate the magnetization by a flip angle $\beta = \omega_1 \tau$ (see figure 3.2). For slightly off-resonant spin packets, this is still a valid approximation, as $\Omega \ll \omega_1$ causes an insignificant precession around $\boldsymbol{B}_0$. The more off-resonant

[III] Analogously, if $\boldsymbol{B}_1$ is oriented along $y, rot \Rightarrow \boldsymbol{M}(t) = R_{y,rot}(\omega_1 t)\boldsymbol{M}(0)$

the excitation frequency, the stronger the deviation of the rotation axis from the xy-plane. In pulse EPR slightly off-resonant magnetization will always be excited, because the Fourier transformation of the rectangular pulse time window, which acts as grating, creates a Sinc function diffraction pattern of the excited spin population

$$P(\Omega) = |\frac{sin(\Omega\tau)}{\Omega\tau}| \tag{3.21}$$

with a FWHM linewidth of $\Delta\nu \approx 1.2/\tau$. From now on, the rotation matrices will be distinguished by their effective flip angle and bandwidth while τ, τ_1, τ_2 will be used as delay times.

It would even be of interest to excite the sample with such high bandwidth pulses that the whole spectrum could be gained from the Fourier transform of its instantaneous answer,[IV] the so-called free induction decay (FID), which is the microwave current induced by the preceding magnetization in the coupling antenna. The width of a nitroxide spin label spectrum, however, would imply gating[V] the necessary microwave power with such rapidness (picoseconds) that is not possible with modern day equipment.

It is therefore necessary to vary one parameter of the resonance condition (Equation 3.1) and compose the spectrum from those single measurements. Stepwise increase of the external field $\boldsymbol{B}_0$ is most feasible.

To increase the sensitivity of the pulse experiment, use of resonators is mandatory. In consequence, the excitation power remains at the sample for a longer time and the direct FID cannot be measured without also risking destruction of the detector (see section 3.7).

Erwin Hahn first suggested[83] the possibility to delay the detection of the system's answer by applying a $\pi/2$-pulse $R_x(\pi/2)$ and after a delay time τ a π-pulse $R_x(\pi)$ (see figures 3.3 and 3.4). After another τ interval, this pulse sequence creates a spin echo in xy plane which contains the information of the FID. This Experiment is repeated at different magnetic fields and is therefore called *Field Swept Echo* (FSE). It is thus possible to separate the spin signal from

[IV] In Fourier-transform EPR (FT-EPR), spectra are acquired this way. Usually this is only feasible for very narrow EPR signals, not for nitroxides.

[V] Opening and closing of a switch to quickly connect to cw microwave for a short time, thus generating a pulse.

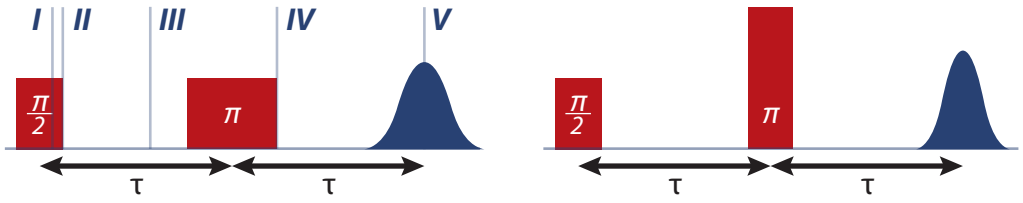

Figure 3.3: *Hahn echo sequence diagram. The echo emerges at time 2τ after the center of the first pulse. The π rotation angle can be achieved with a twice as long pulse of the same power* (left) *of with a pulse of same length but proportionally higher power* (right)*. In the left diagram, the time positions for figure 3.4 are noted.*

remaining $\boldsymbol{B}_1$ pulse power. The integral over the whole echo is in proportion to the number of spins in resonance at $\boldsymbol{B}_0$ and ω_1.

The signals measured in the xy plane are still in the rotating frame, hence they are always modulated onto the carrier frequency ω_{mw}. Quadrature detection is employed as a means of creating sum and difference frequencies of this signal path and a second, equally long reference pathway. The sum frequency subsequently is filtered, leaving only the difference frequency, which is Ω. This renders the measurement very sensitive, as the resonance case marks the point of origin with $\Omega = 0$.

3.4 Signal Relaxation

Until now we only have discussed the mechanisms of spin magnetization without relaxation.

The decay of excited magnetization $\boldsymbol{M}$ back into its ground state $\boldsymbol{M}_0$ is a fundamental effect in EPR and has to be taken into account to understand the limits of experimental viability. An excellent publication on this topic is Poole and Farach 1971 [84].

In contrast to nuclear magnetic resonance (NMR), the time constants of relaxation in EPR are of the same order of magnitude as the length of short one-digit pulse sequences. This is however outweighed by the specificity of EPR for radical species, which allows conclusive information to be acquired with a small number of pulse operations on the spin population.

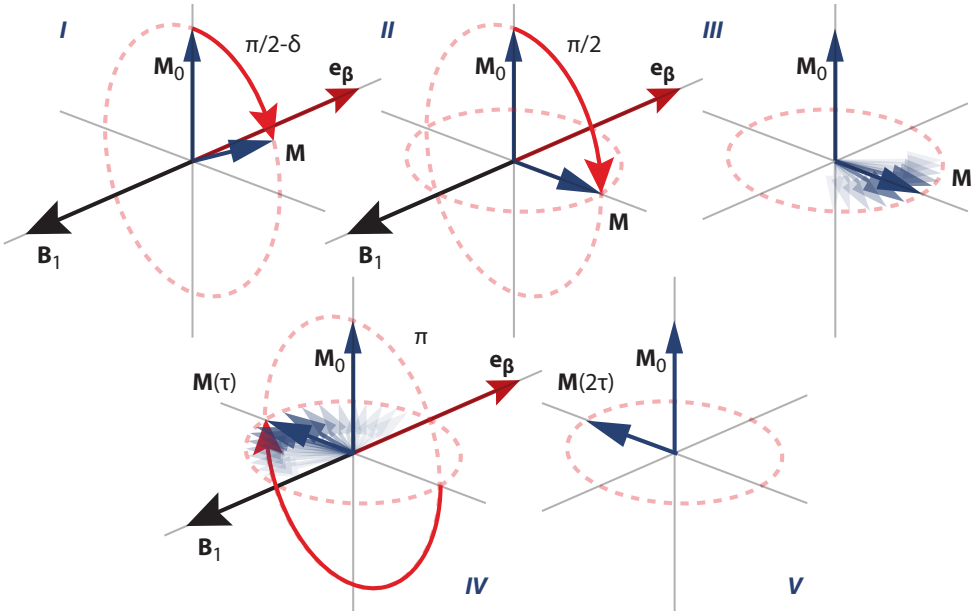

Figure 3.4: *Magnetization during Hahn Echo sequence. The time positions I to V are marked in the pulse sequence in figure 3.3. The refocusing within the xy plane can be repeated several times by additional π pulses.*

Bloch Equation with Relaxation

If we consider reorientation of $\boldsymbol{M}$ back into its preferred state $\boldsymbol{M}_0 = M_0 \boldsymbol{e}_{B_0} = (0, 0, M_0)$, the Bloch equation is modified to

$$\frac{d}{dt}\boldsymbol{M} = \gamma(\boldsymbol{M} \times \boldsymbol{B}) + \mathcal{R}(\boldsymbol{M}_0 - \boldsymbol{M}) \tag{3.22}$$

with $\mathcal{R} = [(1/T_2, 0, 0); (0, 1/T_2, 0); (0, 0, 1/T_1)]$ defining T_1, the longitudinal spin-lattice relaxation and T_2, the transversal spin-spin relaxation, which are phenomenological parameters defined by the environment of the spin. This equation of motion has the time dependent solution

$$\boldsymbol{M}(t) = R_z(\omega_0 t) e^{-\mathcal{R}t} \boldsymbol{M}(0) + (1 - e^{-\mathcal{R}t}) \boldsymbol{M}_0 \tag{3.23}$$

It describes the magnetization $\boldsymbol{M}(t)$ in a spiraling motion with its angular orientation continually progressing to $\boldsymbol{M}_0$ in $z-$direction.

Longitudinal relaxation

Longitudinal relaxation with its decay time T_1 is responsible for the reorientation of the macroscopic magnetization back into its preferred orientation along z. Every single excited electron that relaxes undergoes a spin flip, therefore changing its m_s; energy is transferred.

This spin-flip relaxation, however, is no spontaneous emission[85]. Its time scale is too large to offer an explanation: With $T_1 = 1/\Gamma_1 \propto 1/\omega^3$, one would expect a T_1 of more than a million hours at W-Band frequency ($\approx 100\,\mathrm{GHz}$). Instead, the decay is caused by coupling of the spins to a phonon bath (thus *spin–lattice relaxation*). Direct transitions are predominant at low temperatures while indirect Raman transitions are most frequent at high temperatures. Both effects increase T_1 exponentially, their superposition has an absolute minimum at intermediate temperature. The exact value is system specific.

Transversal relaxation

Transverse relaxation is the loss of coherence within the excited spin packet (loss of phase information). It is caused by spin flip-flop processes which retain energy within the spin system, but destroy phase information (hence *spin–spin*

relaxation). All T_1 processes also destroy the coherence of the affected spins to the packet. In powder samples, T_2 is nearly always shorter than T_1 for this reason.

Every experiment in pulsed EPR is based on non-ideal pulses where the phase memory time T_m is the relevant decay parameter for transversal relaxation. It includes additional relaxation effects, especially the inhomogeneity of $\boldsymbol{B}_1$ inside the sample. Due to sample properties as well as due to cavity geometry, the pulse power is concentrated in the center of the spin sample, but diminishes in direction of the boundaries (see later figure 3.10 for a qualitative sketch). It leads to different effective flip angles within the excited spins, thus reducing the effective magnetization.

In addition, microwave pulses applied to an excited spin system cause instantaneous relaxation, which is the occurrence of different Larmor frequencies within a spin packet after pulse excitation. In a fraction of the excited spins A, another surrounding spin B has been flipped in addition. The dipolar influence of spin B on spin A modulates its Larmor frequency in proportion to its distance (see equation 3.13) and thus adds to the dephasing of the excites spins A. Spin B can be another electron spin or a nuclear spin, especially protons are abundant in many biological samples. For the most part protons relax via transversal relaxation among each other, increasing the fluctuations of the local field at the electron spin A with $1/T_m \propto \sqrt{g_n^3 \sqrt{I(I+1)}}$, dominating the relaxation[75]. Theoretically a completely deuterated biological sample could prolong this T_m contribution by a factor of 13. With solvent exchange as discussed in chapter 2, a 1.5 to 4 time increase of T_m can be achieved, depending on the sample.

Sample concentration linearly effects this dipolar background interaction as the mean distance between spins is reduced. This leads to a trade-off between signal intensity and relaxation time.

As transversal magnetization contains several effects that are determined by technical parameters in a complex way via dipolar interaction, it is reasonable to keep most of its influence constant during an experiment. The four pulse ELDOR experiment used in this work is a *constant time* experiment that only varies one pulse, but keeps the the pulses acting on spin A and the acquisition of the signal at constant positions to eliminate the influence from this statistical dipolar interaction (see below).

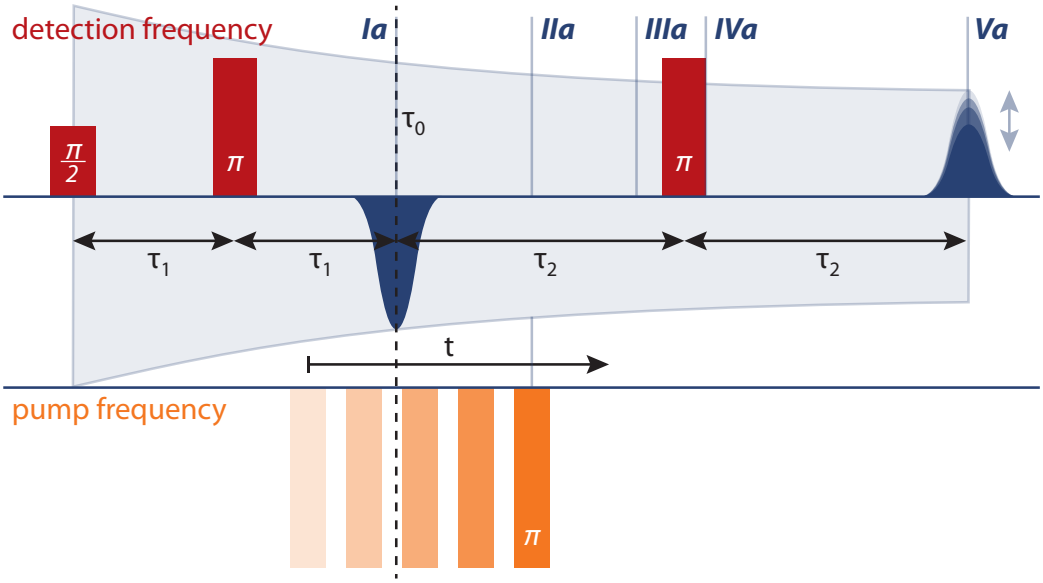

Figure 3.5: *ELDOR/DEER sequence. Its pulse sequence is based on a Hahn echo, which is later refocussed by the detection pulse of the same frequency at a constant time. Time positions for figure 3.6 are noted.*

3.5 Pulsed ELDOR

Electron-electron double resonance experiments were first introduced by Mims et al. in 1959[86] to investigate relaxation mechanics and concentration dependent effects. The principle of utilizing the r^{-3}-dependence of the electron-electron dipolar interaction to determine the spatial arrangement of spins A and B with different resonance frequency was employed by Milov et al. in the 1980s[87,88,89]. The basic experiment consists of three pulses, two of which comprise the Hahn echo sequence for spins A. The third pulse is of a different frequency resonant with specific spins B and is applied in between. This experiment can determine the dipolar interaction between spins A and the selected spins B, which can be converted to a distance.

One important early application was the determination of the distance between Tyrosine D and the water-oxidizing Mn-Cluster in Photosystem II by Kawamori et al.[90,91].

Martin et al.[92] augmented this method in 1998 by introducing a four pulse

experiment, 4-pulse electron double resonance or DEER (from Double Electron-Electron Resonance), which is the main technique used in this work to determine the distance distribution of selectively attached spin labels in proteins. The measurements in frozen solution are used for refinement of proposed crystal structures and distinction between different conformations.

The experiment makes use of the distance dependence of the dipolar interaction as follows: The detection spins A are excited with a Hahn echo sequence and this echo is refocused again by another π pulse of the same frequency. The spins B are flipped in between by the ELDOR π pulse of different frequency (also called pump pulse). This B spin flip changes the local field at all positions A and affects A's Larmor frequency by $\omega_{dd} \propto r^{-3}$ for the remainder of the experiment (see equation 3.13)[VI]. In consequence, the refocused detection spin A is shifted by a phase $\omega_{dd}(t - \tau_0)$, modulating the second echo by $cos(\omega_{dd}(t - \tau_0))$.

The ELDOR pulse is then stepped in time (see figure 3.5) and produces an oscillating time trace with acquisition at the constant position $2\tau_1 + 2\tau_2$. The merit of 4-pulse ELDOR in contrast to the abovementioned 3-pulse sequence without the refocused echo is the inclusion of τ_0 in the experimental trace without crosstalk between two different pulses inside the cavity at the same time – the pump pulse can pass the first echo without overlap to the detection pulses. As with all methods where Fourier transformation from the phase space to the local space occurs, knowledge of the zero-time and -amplitude is essential ($\rightarrow$ phase problem in x-ray crystallography).

As the positions of the detection pulses are constant, the influence of T_m on the A spins is always the same, regardless of the pump pulse position[VII]. In consequence, the ideal ELDOR/DEER experiment separates the dipolar coupling $\mathcal{H}_{EEdip}$ between A and B from other interactions. For samples with defined geometry like the aforementioned radicals embedded inside Photosystem II, the distance r between A and B can often already be read from the single oscillating frequency via equation 3.15 to $r \approx (52 T_{dd}/\mu\mathrm{s})^{1/3}\mathrm{nm}$. However, spectra of bio-

[VI] If one spin direction is called α and the other β, the flip of the B spin changes the observed transition from $|\beta\alpha\rangle \leftrightarrow |\alpha\alpha\rangle$ to $|\beta\beta\rangle \leftrightarrow |\alpha\beta\rangle$, which are separated exactly by ω_{dd}, with $\omega_{dd} \ll |\omega_A - \omega_B|$

[VII] T_1 is usually much longer than T_m in spin labeled proteins, so that its influence due to the variable position of the ELDOR pulse can be neglected.

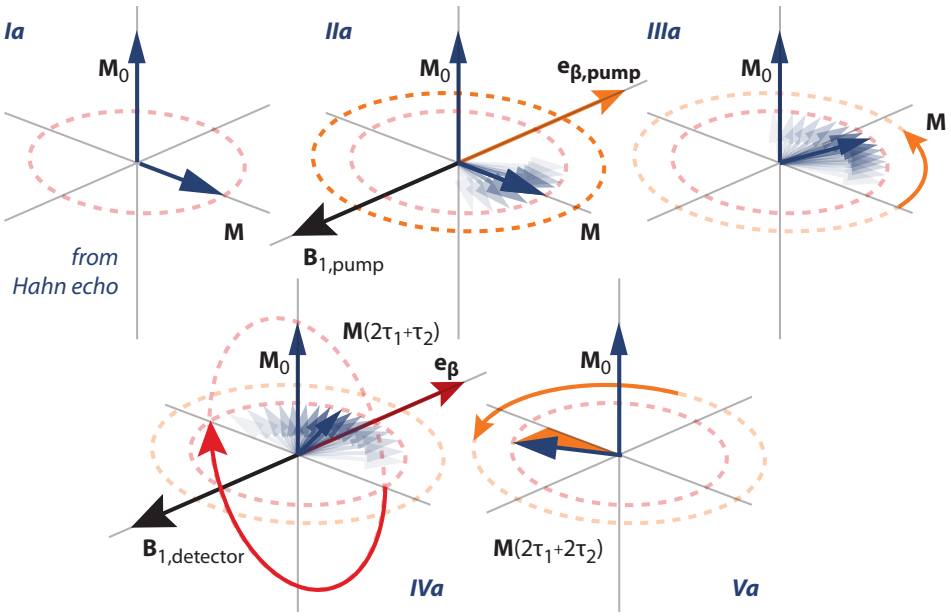

Figure 3.6: *Magnetization starts with the Hahn Echo from figure 3.4. The points in time Ia to Va are marked in figure 3.5. The pump pulse (orange) changes the local field of the detector spin, and thus its Larmor frequency. Thus, the magnetization precesses even within the rotating frame and at the time of acquisition, it has obtained a phase, reducing its recorded projection.*

logical samples with attached artificial spin labels are usually much broader and the fitting is more involved (see chapter 4).

ELDOR is always measured in frozen solution, because the dipolar matrix $\boldsymbol{D}$ is baseless and would be distorted to a stochastic residual anisotropy at higher temperatures due to random dynamics. Frozen solution captures neighboring proteins in their homogeneous distribution without the possibility for motional narrowing. They contribute as an exponential decay background factor

$$B(t) = e^{-kt^{d/3}} \tag{3.24}$$

with $d = 3$ for solutions, smaller for lipids, and k as fitting parameter to the designated part of the overall ELDOR trace $V_{ELDOR}(t) = B(t)F(t)$ used for background determination with the overall modulation depth

$$\Delta = 1 - B(0)/F(0). \tag{3.25}$$

With the assumption of completely excited Pake patterns, which is approximately achievable for $r > 1.5\,\text{nm}$ (see figures 3.7). The dipolar evolution function $D(t)$ itself is the integral over all possible orientations θ of the interspin vector and is expressed for one length r as

$$D(t) = \frac{F(t)}{F(0)} = 1 - \int_0^{\pi/2} d\theta \lambda(\theta)[1 - cos(\omega_{dd}(\theta)t)]sin(\theta) \tag{3.26}$$

The dipolar frequency from equations 3.13 and 3.14 is

$$\omega_{dd} = 2\pi\nu_{dd} = \frac{1 - 3cos^2(\theta)}{r^3}\frac{\mu_0}{4\pi\hbar}g_A g_B \mu_B^2. \tag{3.27}$$

The field swept powder spectrum of a nitroxide labeled protein can be considered as an inhomogeneous line consisting of individual spin systems of different orientation (see figure 3.7). When all orientations of the interspin vector $\boldsymbol{r}$ are excited, the Fourier transformation of the background corrected time trace $F(t)$ becomes a Pake pattern with width $2\omega_{dd}$ (see equation 3.14). In real samples, a perfect Pake pattern is seldom observed due to unequal excitation of different sub-orientations. Usually, the perpendicular component $\omega_\perp$ is best pronounced (figure 3.8).

Apart from this intrinsic Pake-broadening of the transition frequency, which mainly causes the first drop of the modulation envelope, further dampening is

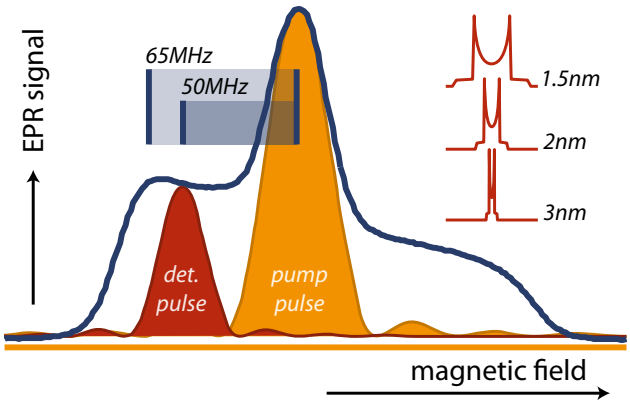

Figure 3.7: *Pulse bandwidth distribution under typical FSE of a spin labeled protein. The ELDOR pulse (32 ns) and the detection pulses (20 ns,40 ns) are optimally 50 to 65 MHz apart to ensure weak coupling (i.e. minimize overlap), but also to avoid orientation selection*[93]. (inset) *Exemplary Pake patterns for intrinsic dipolar broadening in homogeneously oriented samples for different interspin distances.*

a result of a flexible interspin distance. A broad distance distribution leads to a faster decay of the modulation than a rigid sample of one distance.

The modulation depth Δ of the ELDOR trace is dependent on the amount of spins interacting[94,95]. If other experimental factors, like labeling efficiency of the sample or bandwidth and distance of the pulses are constant, Δ would be 0.5 or less (if not all possible combinations are excited and/or labeled) for two spins interacting. If the modulation depth is larger than 0.5, the sample is a trimer or even an oligomer.

For the measurement of the modulation depth, the knowledge about the zero level is critical. To this end, a phase cycle is introduced, where a negative modulated echo is subtracted from a positive one, thereby eliminating a constant offset. With the same principle, additional echoes, which cross and distort the detected echo signal, can be suppressed by increasing the amount of cycled pulses[VIII].

Figure 3.7 illustrates the intrinsic spectral overlap of finite pump and detector pulses in the frequency domain. This leads to certain percentage of detection

[VIII] A double phase cycle would therefore include four scans: The first phase cycle (two scans) and then these two scans with otherwise cycled setup.

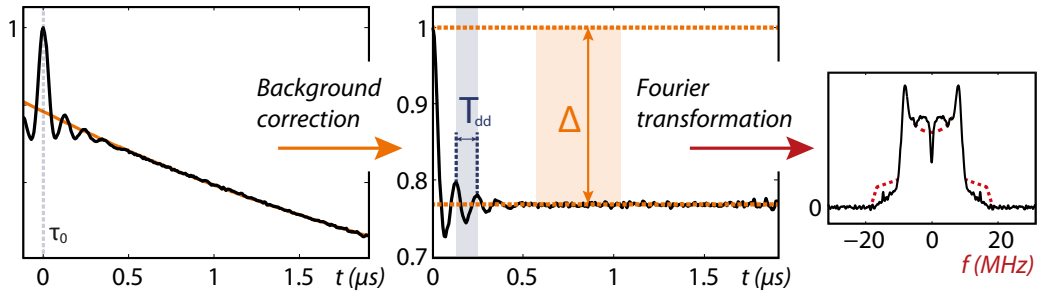

Figure 3.8: (left) *An exemplary ELDOR spectrum, as recorded, normalized. In orange, the fitted background function* $B(t)$. (center) *Dipolar evolution function* $D(t)$ *with modulation depth* Δ *and oscillation period* T_{dd}. (right) *Fourier spectrum of the time evolution function. In red, the actually expected Pake pattern for complete excitation. For details, see text.*

spins excited by both the ELDOR and detection pulses. For these, the experiment is not a constant-time experiment and the small probability of each microwave pulse flipping a surrounding nuclear spin (particularly protons), that in turn additionally modifies the Larmor frequency of this detector spin, does not lead to a constant factor anymore, but depends on the ELDOR pulse position. It is therefore advisable to take the mean of this additional nuclear oscillation by stepwise increase of the initial Hahn echo pulse distance up to one full proton oscillation, which is still short in the overall time window but cancels the proton contribution. This process is called nuclear averaging.

3.6 cw EPR

In continuous wave EPR (cw EPR), $dM/dt = 0$ gives a steady state solution to the Bloch equation in form an absorptive and a dispersive Lorentzian, with the absorption peak having an FWHM of $2/T_2$. Irradiation with $\boldsymbol{B}_1$ is constant and assumed weak. The external magnetic field is stepped as in the FSE experiment and the steady state response is measured. The constant irradiation leads to a very narrow bandwidth of simultaneous excitation: For this reason the sensitivity of cw EPR is generally lower than that of pulsed EPR, which makes it necessary to modulate the magnetic field with a lock in frequency (usually 100 kHz) to separate the signal from stray electromagnetic interactions and statistical noise.

The detected spectrum therefore corresponds to the local slope (the derivative) of a directly measured field swept spectrum. The amplitude of the field modulation has to be chosen according to the spectral width, in order not to flatten sharp features.

Irradiation and detection occur at the same time, which makes it necessary to critically couple the resonator to the microwave, so that incoming and outgoing waves cancel and the detection can still be sensitive. Any resonance of the spin system then additionally modifies the impedance of the resonator: As energy is absorbed, incoming and reflected power don't equilibrate anymore and the difference to zero can be measured as diode current.

Room temperature cw EPR

In liquid samples, especially at ambient temperature, motional narrowing causes the off-diagonal elements of the g-matrix to average to zero. The motional correlation time of the electron spin τ_c is a defining parameter of the spectral shape.

In the simplest case of a very small molecule, the spin-rotational coupling is given by the rotation of the whole molecule. For rather spherical proteins, τ_c can be approximated via the Stokes-Einstein-relation with R_g the effective radius of gyration and η the viscosity of the solvent.

$$\tau_c = \frac{4\pi\eta R_g^3}{3k_BT}, \tau_c \propto \eta \tag{3.28}$$

Figure 3.9 demonstrates the evolution of an X-band cw-EPR spectrum from fast motion down to the rigid limit. For this example, the same parameters were used as for the later simulation of measured spin labeled DnaJ, the time constants are comparable. Fast motion of the spin label leads to three narrow and equidistant nitroxide resonances, while slower tumbling results in a continuous broadening of the outer lines. The fast spectra have an overall width of 3 mT, while the rigid spectra extend over 6.8 mT.

The effect of motional narrowing with a given τ_c is constant regarding its effective width. A W-band cw-EPR spectrum is far broader than an X-band spectrum due to the Zeeman interaction. Therefore fast moving spin samples that show sharply narrowed lines in X-band (9.4 GHz) can often be characterized more exactly in W-band (94 GHz) where their spectral shape is still in a

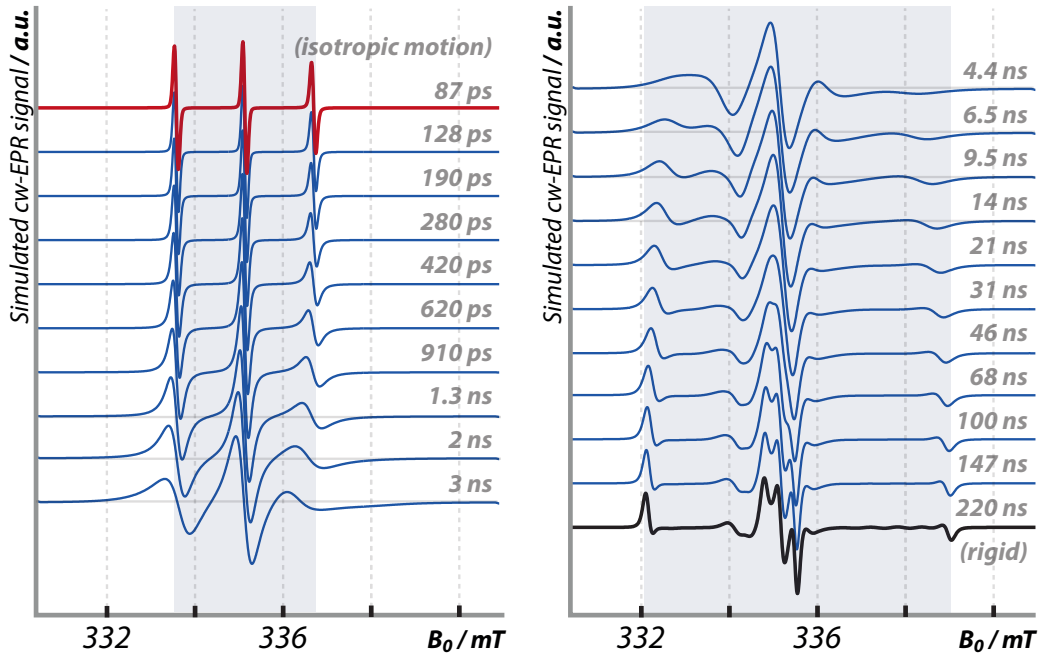

Figure 3.9: *Exemplary simulation of anisotropic motion of a nitroxide. The rotational correlation time τ_c is varied from the rigid limit (black) to the narrow lines of isotropic motion (red). Note the drastic reduction of the outer lines' splitting from slow to fast rotation. The simulation was done with EasySpin chili, the spectra were normalized to a constant maximum amplitude for clarity.*

transitional state. A good example is given in White et al. 2007[96]. For the labeled samples examined in this work, X-band has been ideal.

As soon as a spin label is bound to a protein, it cannot rotate isotropically, but has a complex energy landscape of possible conformations (rotamers) it can assume with variable probability determined by the surrounding. Hence, its anisotropic motion can be understood as multi-site exchange between all its rotameric conformations, the motional correlation time τ_c as inverse of a diffusion rate. A very flat energy landscape, which can be completely flooded by room temperature kT, allows very rapid exchange between orientations, high diffusion, and thus fast motion with small τ_c. A landscape with only a few allowed states within kT introduces additional anisotropy as conformational exchange is reduced, leading to distinct shoulders in the spectrum. Usually, a reduced diffu-

sion between two distinct sub-populations of rotamers lead to strong observed anisotropy[97]. In any case, a longer correlation time τ_c is the consequence.

In addition, the side chain as well as the whole protein can move. This is reflected in experimental cw-EPR spectra as complex spectral shapes that are in first order linear combinations of different isotropic τ_c spectra. The evaluation of the main components together with a discussion of residual amplitude in the spectrum can provide significant insight into the protein surrounding of the spin label.

3.7 EPR spectrometer

A common EPR spectrometer is built up of three main components, a) the microwave bridge and its control unit, b) the resonator cavity (usually equipped with a cryostat for sample temperature control), and c) the magnet with its power supply and its field control unit (for cw, also the field modulation coil and the lock-in detection system).

For Q-band, X-band and below, a water-cooled electromagnet is used. W-band requires a superconducting main magnet (3.5 T) for the resonance condition with $g = g_e$ to be fulfilled. Here, field stepping is done with a separate set of room temperature coils; both fields combine to $\boldsymbol{B}_0$. In any of these setups, the homogeneity of the external magnetic field is an important prerequisite for successful EPR measurements, as differences or a gradient of $\boldsymbol{B}_0$ evoke different Larmor frequencies, thus a broadening of the signal.

Resonator cavity

The cavity fulfills two main tasks. It keeps the energy of the microwave pulse at the sample for a certain time to increase their interaction. By its geometry and combination of materials, it prevents the $\boldsymbol{E}_1$-field of the microwave from penetrating the sample[IX] while concentrating the (weaker) $\boldsymbol{B}_1$ part at exactly this position. Three archetypes exist: The *box cavity* is the simplest construction

[IX] Especially in watery biological samples, but also other specimen with abundant dipolar molecules, too much $\boldsymbol{E}_1$ within would lead to strong heating and dampening of the microwave, and therefore to distortion/decay of the EPR signal.

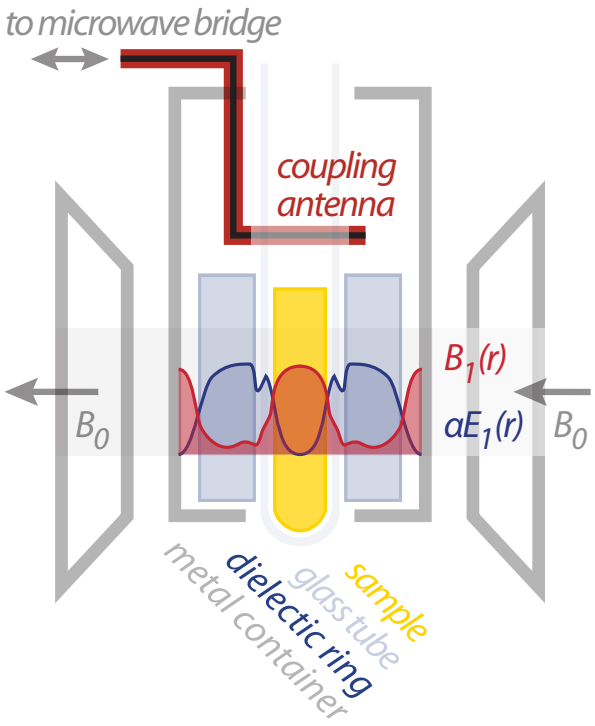

Figure 3.10: *Qualitative sketch of the microwave intensity along the radial axis of a dielectric ring oscillator.* $\boldsymbol{E}_1$ *is drawn into the dielectric, while the* $\boldsymbol{B}_1$ *intensity necessary for pulsed EPR is focused at the sample position.*

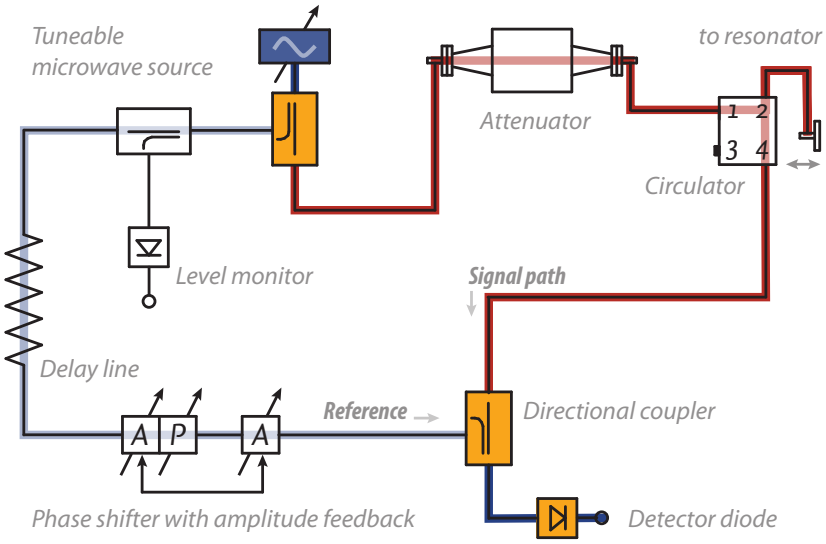

Figure 3.11: *Diagram of a cw-EPR microwave bridge. Shown are the signal path in red and the reference path in blue. For details, see text.*

used in cw EPR. It guides the microwave of according frequency by the geometry of its main mode, the sample is placed at the knot position of $\boldsymbol{E}_1$. The *split ring* or *loop gap resonator* visually implements the LC-circuit with the sharp split acting as a capacitor, concentrating most of $\boldsymbol{E}_1$, while the sample is placed in the center of the one-loop coil. This design has been expanded to different geometries with several loops and gaps to improve the coupling to the microwave antenna as well as the $\boldsymbol{B}_1$-separation. The pulse experiments in this work have used a *dielectric ring resonator* (see figure 3.10). Here $\boldsymbol{E}_1$ is concentrated inside the dielectric ring medium around the sample, while the $\boldsymbol{B}_1$-field is maximized at the location of the sample.

In every case, geometry is always a defining factor – consequentially, any such resonator is only suitable for a small range of microwave frequencies.

Microwave bridge

The required functions of a microwave bridge differ depending on its use in cw or pulsed EPR. From the sketch of the cw microwave bridge (figure 3.11), the splitting of the microwave into a signal path and an equally long reference path-

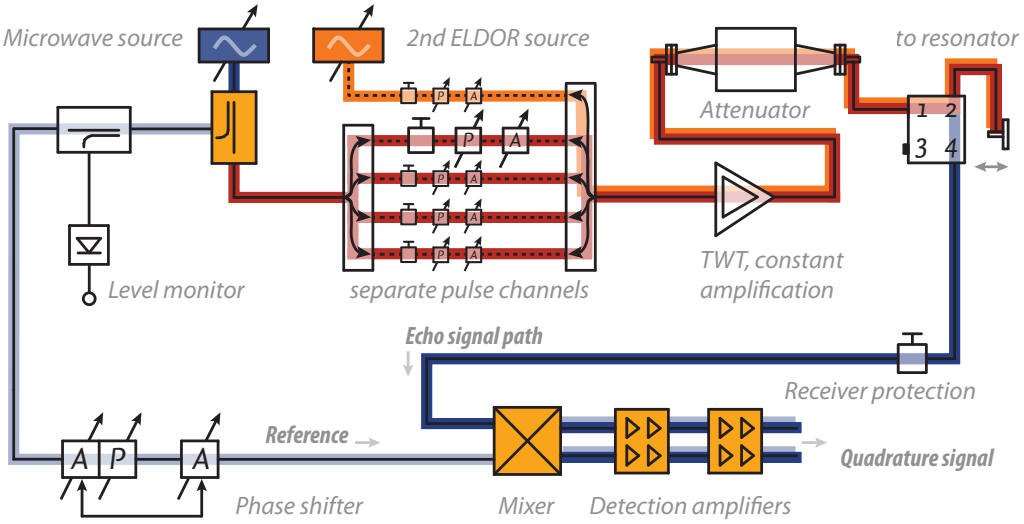

Figure 3.12: *Diagram of an EPR pulse bridge. In addition to the microwave source for primary pulses and reference, a second ELDOR source is coupled into the signal pathway, which can be tuned to a different frequency (orange). For details, see text.*

way is evident. With this technique phase noise of the microwave source can be suppressed by subtracting both pathways from one another before detection. Maintaining a constant amplitude is important for this operation, therefore a level monitor has to be included. To account for any phase shifts due to different sample/resonator geometry, a mechanically adjustable delay line is built into the reference path together with an active feedback to sustain the amplitude.

Overall the matched impedance (*critical coupling*) can be lost by either an unstable microwave frequency (which is counteracted by cooling the source) or the cavity moving out of resonance due to thermal motion caused by ambiance effects – which cannot be completely prevented in a normal laboratory. Hence, a feedback frequency control is mandatory for long-time measurements to track the cavity and actively regulate the microwave frequency accordingly.

In a pulse spectrometer bridge (figure 3.12) the reference path with constant, weak irradiation is still present for downsampling of the incoming echoes at the mixer (see above). The pulse and signal pathway is equipped with several separate channels for pulse generation, which can be timed as well as adjusted in phase and amplitude independently from one another. Here, a second, unrefer-

enced microwave is added from the external ELDOR source. The ELDOR pulse therefore has no fixed phase relation to the remainder of the sequence.

The short pulse lengths make it necessary to use an external high power traveling wave tube (TWT) amplifier[X], which has a constant amplification factor. This maximal power defines the shortest pulse length to achieve a chosen flip angle with and simultaneously sets the limit maximal bandwidth that can be reached with the spectrometer.

The high power of the pulses makes is indispensable to protect the detector while the power has not yet decayed within the cavity. Commonly, PIN diodes are used as fast switches for this purpose as well as for the pulse creation.

Compared to cw irradiation, even relatively long pulses have a much higher bandwidth, so a larger population of spins is excited in each experiment. For this reason, pulsed EPR has a higher sensitivity than cw EPR.

To achieve reasonably fast relaxation of the pulse power, the resonator's impedance is not matched, but overcompensated (*overcoupled*). Still, the *dead time* after a pulse before any signal can be detected, cannot be reduced to zero and is the second, technical reason for the ELDOR/DEER sequence to contain a refocusing π-pulse. Three-pulse ELDOR cannot detect the spectrum from τ_0 on, but can only start acquisition after the dead time.

A further motivation for overcoupling is the increase in bandwidth that is absorbed by the resonator and can reach the sample. This is relevant for ELDOR experiments on labeled proteins, where the two microwave frequencies 50 to 65 MHz apart from each other are used.

The detection of the echo that was emitted at a later time from the resonator/sample is qualitatively similar to the cw setup. A mixer transmits only the difference frequency between reference and echo signal, this information is then enhanced by Video amplifiers and recorded.

[X]The TWT works by feeding the microwave into a coil around an electron beam, which in turn is bunched with increasing strength by the electromagnetic field created by the circumscribing microwave. The reciprocal action of the bunched beam on the coil then amplifies the microwave. In front of the beam dump, the coil connects to an output.

Chapter 4

Methods and Materials

This chapter describes the EPR methods as well as the biological sample conditions of DnaJ and BlrB used in this work. Furthermore, it includes a summary of results from the cooperating group at the *Max Planck Institut für Medizinische Forschung, Heidelberg* (MPIMF) on which the analysis of the EPR experiments are partly founded (crystallographic data) or which provide complementary information for the interpretation of the ELDOR results (Small Angle X-ray Scattering – SAXS and UV/visible absorption measurements of BlrB). In the final section, the consequences of different label pair geometries on the measured distance distribution are explained.

4.1 Experiments

Instrumentation

Pulse spectrometers A commercial *Bruker Elexsys 680* X/W-band combination equipped with an external ELDOR source *Bruker E580-400U* and a *Bruker ER4118X-MD-5* dielectric ring resonator was used for most of the pulsed ELDOR experiments. The microwave pulses were amplified by an *Applied Systems Engineering 117X-1 TWT* 1 kW traveling wave tube amplifier. A *Bruker B-E25* magnet was combined with a *Bruker ER 083 (200/60)* magnet power supply. Sample cooling was provided by an *Oxford CF935* cryostat for liquid helium, controlled by an *Oxford ITC 503S* temperature controller.

Several spectra were measured on a similar *Bruker Elexsys 580* X/Q-band

combination with built-in ELDOR source and a *Bruker ER 073* magnet/*Bruker ER 083 CS* power supply combination. Again, a *Bruker ER4118X-MD-5* dielectric ring resonator and a *Applied Systems Engineering 117X* TWT were used.

X-band cw spectrometer A custom assembled X-band cw spectrometer was used for room temperature cw experiments, that consisted of commercial single components. An *AEG-ESR 20 XT* magnet was controlled by a *Bruker B-H 15* field control unit and supplied by a *Bruker ER 081S* power supply. The microwave bridge *Bruker ER 046 XK-T* was controlled by a *Bruker ER 048 R* bridge control unit and the microwave frequency was recorded by an *Agilent 53181A* frequency counter. A *Stanford Research SR810 DSP* lock-in amplifier provided field modulation. The Bruker *Super-HQ* box cavity is mounted on an *Oxford ESR 910* finger cryostat, again controlled by an *Oxford ITC 503S*.

ELDOR

Optimizing relaxation The transversal phase memory time T_m determines the maximum length of the acquired ELDOR trace and hence the maximum interspin distance up to which reliable information can be extracted from the ELDOR spectrum (see equation 3.15). It is therefore important to maximize this parameter.

Lower temperature significantly prolongs T_1 as well as T_2/T_m. Instead of measuring in frozen solution just below the freezing temperature, conditions of 80 K to 50 K are ideal[98]. Below 50 K, gains from T_m increase are suppressed by long T_1 and the associated reduced repetition rate of the experiment.

Grain boundaries are a major factor in spin relaxation. Creating a glassy sample by quick-freezing a biological sample solution with a high percentage of glycerol resulted in an increase of T_m by a factor of 1.3 to 2.

To measure long distances, it is also helpful to minimize the interactions between the electron spin and surrounding nuclear spins. *Deuterating* the solvent (water and glycerol) yielded a further increase of T_m by a factor of 1.5 to 4. This procedure introduces a strongly pronounced deuteron ESEEM modulation already on the first echo signal in comparison to a protonated sample. The oscillation is elongated by the ratio between their free Larmor fre-

quencies ($\omega_H/\omega_D \approx 6.51$), which makes a correct placement of the primary echo sequence mandatory. The first maximum of the deuteron ESEEM is at $\tau_1 \approx 330 - 360$ ns, therefore the initial pulse delay was chosen accordingly.

Experimental parameters For the pulsed ELDOR experiments, the following parameters were used:

initial pulse delay τ_1	200 ns for protonated buffer,
	360 ns for deuterated buffer
detector π-pulse length	40 ns
pump π-pulse length	32 ns
length of time trace τ_2	between 2 and 7.8 µs

The pump-pulse was centered at the maximum of the nitroxide EPR spectrum with its power adjusted for best inversion efficiency of the B-spins (see figure 3.7). The detection frequency was 60 MHz higher, thus exciting spins in the left shoulder of the spectrum as A-spins. The power was set to optimize the echo signal intensity right below saturation. The repetition time of the experiment was 4 ms. The video amplification with a bandwidth of 50 MHz was optimized for maximal signal resolution without clipping.

A two-step phase cycle for the $\pi/2$-pulse excluded any receiver offset, nuclear modulation was suppressed by an eight-step progressive extension of the initial Hahn echo by 8 ns in each step.

Room temperature cw-EPR

The room temperature cw-EPR spectra were recorded with 20 dB microwave attenuation to measure below saturation, with 300 ms conversion time, 100 kHz lock-in frequency, 0.1 mT modulation amplitude and 10 mV lock-in sensitivity.

4.2 Calculations

The analysis of the spectra was done in MATLab with different sets of tools. DeerAnalysis[99] was utilized for ELDOR trace evaluation and determination of the distance distribution, Easyspin[100] for all simulations of cw-EPR spectra, and MMM[101] for rotamer calculations from the crystal- and model structures. A structure variation program written by Thomas Barends[I] was used for the DnaJ intra dimer distance modeling, a self-written substantial modification for the modeling of BlrB based on ELDOR results (see below).

ELDOR analysis

Background correction The first important aspect of ELDOR trace analysis is the separation of the background from the dipolar interaction within the studied molecules. We assume a d-dimensional homogeneous distribution of spins causing an exponential background decay.

$$V_{ELDOR} = B(t)F(t),\ B(t) = exp(-kt^{d/3}). \tag{4.1}$$

The dimensionality d is always 3 for soluble samples, which is the case for DnaJ as well as for BlrB. As explained in Mims 1972[102] and Bode et al. 2007[95], $k \propto c$, the sample concentration. This is due to the fact that the amount of interacting spins at every distance statistically increases with increasing c. It especially has to be regarded when samples of different concentration are compared with respect to their modulation depths (see following section).

From a single experimental time trace, $B(t)$ can only be definitely assigned when all modulation frequencies ω_{dd} have mixed to zero within the length of the time trace τ_2. This mixing occurs less rapidly for narrow than for broad distributions. As the length of the time trace is limited, the mixing is not complete for narrow long distances and the background $B(t)$ is difficult to assign when additional shorter distances are superimposed.

In such cases, distortions may arise in the ELDOR fit from an incorrectly determined normalized dipolar evolution function $D(t) = F(t)/F(0)$. These artifacts have the strongest influence on peaks at longer distances down to about

[I] Max Plack Institut für Medizinische Forschung (MPIMF), Heidelberg

5 nm. Due to the cubic relation between oscillation period and distance, positions below 4 nm are very resilient against deviating background assignment. In this work, the background has been simulated from the data in the second half of the time trace, unless obvious reasons required otherwise.

As required by the Sampling Theorem[103], τ_2 defines a maximum observable oscillation period. The phase of all ELDOR oscillations is intrinsically zero at τ_0, hence the maximum observable half period determines the maximum resolved interspin distance ($r = \sqrt[3]{52.0\,\tau_2/s}$) under perfect conditions (see equation 3.15).

In non-ideal experiments with existing noise however, time traces contain significantly less accurate information for longer oscillations as the Fourier resolution is diminished with the ratio between τ_2 and T_{dd}.

Together with the reliability of the background correction, this is reflected by the introduction of confidence intervals of different levels of information depending on τ_2.[99] In this work, they are depicted above each distance distribution with dark blue being most reliable and red allowing only qualitative argumentation.

Modulation Depth Closely related to the background is the information about the modulation depth $\Delta = 1 - B(0)/F(0)$. According to Milov et al.[104], for a small number N of spins within one molecule (or dimer/oligomer/cluster) the expression for the ELDOR trace changes to

$$D(t) = \frac{1}{N}\sum_{A}^{N}\{\prod_{A\neq B}^{N}(1-\lambda(1-\langle cos\,\omega_{dd}^{A,B}t\rangle))\} \tag{4.2}$$

where λ is assumed constant and $\{\ldots\}$ is the integration over $\theta^{A,B}$ and $r^{A,B}$. With $\langle cos\,\omega_{dd}^{A,B}T_{dd}/2\rangle = 0$, it is possible to gather information about the average number of discrete spins N interacting with the detection spin A from 4.2[94,95]. The modulation depth Δ then fulfils[104,105]

$$\Delta = 1 - (1-\lambda)^{N-1} \tag{4.3}$$

$$\Rightarrow N = \frac{ln(1-\Delta)}{ln(1-\lambda)} + 1 \tag{4.4}$$

To compare several measurements, it is necessary to either know the excitation efficiency λ by calibration or to make sure it is constant in all compared

spectra by constant measurement conditions. In X-band measurements of nitroxide samples, a pulse excites only a fraction of all spins (see figure 3.7) leading to a small excitation efficiency $\lambda \ll 1 \Rightarrow ln(1-\lambda) \approx -\lambda$.

$$\Rightarrow \frac{N_1}{N_2} \approx \frac{1-\Delta_1}{1-\Delta_2} \tag{4.5}$$

Using equation 4.5, it is possible to estimate populations within one sample if the modulation depths for separate contributions to the distance distributions can be isolated. In the case of one small distance to spins B_{short} in a cluster with several spins of significantly larger r, this is approximately possible by comparing the depth of the first oscillation dip with the oscillation depth at long times (preferably at the end of the time trace at τ_2). In this case the dipolar interaction between A and B_{short} within its first oscillation is not yet under strong influence from the remaining B spins.

Tikhonov Regularization For narrow interspin distance distributions, data analysis using only Fourier transformation is feasible.

The Fourier transform of the dipolar evolution function $D(t)$ constitutes a single Pake pattern where the splitting ω_{dd} is prominent and can readily be converted into a mean distance (see equation 3.15). For biological samples, this is especially the case for naturally occurring paramagnetic species like Tyr^D in Photosystem II[90,91]. For small molecules in solution, however, even a rigid stick molecule with radical spins at each end shows significant flexibility, thus changing the distance depending on the relative angle, which leads to a broadening of the observed distribution[106].

In common biological samples with attached spin labels not only the mean distance, but its complete distance distribution $P(r)$ is of interest, as its width and shape strongly depends on the immediate surrounding of each spin as well as on the folding and dynamics of the protein. It is therefore more accurate to assume a wide distribution of positions of certain width, not following a specific model, and simulate the spectrum and time trace $S(t) = \int dr\ K(r,t)P(r)$ back from them. To prevent over-modulation, the number of simulated distance positions is gradually reduced while the remaining lines in $P(r)$ are subsequently broadened to still fit the experiment. The Kernel function $K(r,t)$ is the analyti-

cal expression of $D(t)$ from equation 3.26

$$K(r,t) = \int_0^1 d\chi \; cos[(3\chi^2 - 1)\; \omega_{dd}(r)t] \tag{4.6}$$

with integral substitution $d\chi = d\theta \; sin\theta$ under the assumption of a constant excitation efficiency $\lambda(\theta) = const.$

Tikhonov Regularization is the method used for determining the optimal compromise between amount of simulated distances and broadening by minimizing

$$G(P;\alpha) = \|S(t) - D(t)\|^2 + \alpha \| \frac{d^2}{dr^2} P(r)\|^2 \tag{4.7}$$

where α, the *regularization parameter*, determines the ratio between fitting accuracy and broadening[II]. The usual method for appropriate choice of α is the *L-curve*, the plot of the χ^2-deviation (the first part of $G(P;\alpha)$) against the smoothness of $P(r)$ (the second part). ELDOR traces with a good S/N lead to an L-shaped diagram for a set of different α, with too sharp peaks not improving the mean deviation on the left side and too smooth $P(r)$ destroying the good fit at the bottom. If the S/N is still reasonable, the angle will become a curve that still can act as a guideline for an optimal α. With worse S/N an alpha that corresponds best to the expected width of the distance peaks was chosen.

If the sample contains monomeric as well as intra-multimeric interactions between spins, they can have different optimal regularization parameters for the different distance signals, as the expected orientation between two monomers can be much less restricted in its conformation than the stiff protein conformation of the monomer.

Another possibility for a biased interpretation is the effect of the pulse bandwidth on the experiment. Shorter pump pulses of hence higher bandwidth can flip fractions of the detection spin population[107,108]. In turn, λ becomes a Gaussian function of ω_{dd} and the effective excitation bandwidth $\delta\omega$.

$$(\delta\omega) = e^{-(\omega_{dd}/\delta\omega)^2} \;,\; K(r,t;\delta\omega) = K(r,t)\; \lambda(\delta\omega) \tag{4.8}$$

[II]To utilize a fast implementation of the Tikhonov Regularization, but still be able to impose $P(r) > 0$, DeerAnalysis uses an external implementation FTIKREG written by J. Weese from the Materials Research Center Freiburg.

In this work, an ELDOR pulse of 32 ns was used, the detection π pulse was 40 ns long. This corresponds to an effective $\delta\omega$ of about 10 to 12 MHz and the effects are visible only for distance contributions below 1.8 nm[109]. This Kernel correction was included where necessary.

EPR simulations

cw-EPR Simulations of the EPR spectra were carried out using the EasySpin package from Stefan Stoll[100]. For room temperature cw-EPR results, the *chili* routine for a slow tumbling motion was used. It solves the *Stochastic Liouville Equation* for the electron spin and one nucleus numerically to first order and generates the EPR spectrum from the computed energy levels:

$$\frac{\partial \varrho(\boldsymbol{r},t)}{\partial t} = -i[\mathcal{H}(\boldsymbol{r}), \varrho(\boldsymbol{r},t)] + \Gamma(\boldsymbol{r})\varrho(\boldsymbol{r},t). \tag{4.9}$$

Here, $\Gamma(\boldsymbol{r})$ is the rotational diffusion operator and the commutator as a whole ($\mathcal{L}(\boldsymbol{r},t) = [\mathcal{H}(\boldsymbol{r}), \varrho(\boldsymbol{r},t)]$) is called the Liouville superoperator. An extensive discussion is given in Schneider & Freed 1989[110].

The simulation can include anisotropic motion with inclusion of a fixed orienting potential, representing the stationary molecule in the external $\boldsymbol{B}_0$ coordinate frame. It was attempted to fit the X-band data accordingly, but the result was ambiguous, and therefore only isotropic motion was considered for the analysis.

MTSL EPR parameters The spin label parameters were determined by a W-band measurement of spin labelled DnaJ I50C/V90C in frozen solution at 60K to $g = (2.0086, 2.0064, 2.0023)$ and $A = (16, 18, 100)$ MHz. The simulation was performed with the EasySpin *pepper* routine.

Structural calculations

The calculations based on the available and new crystal structures are essential to this work, as they provide a comparison for the experimental data as well as a basis for interpretation.

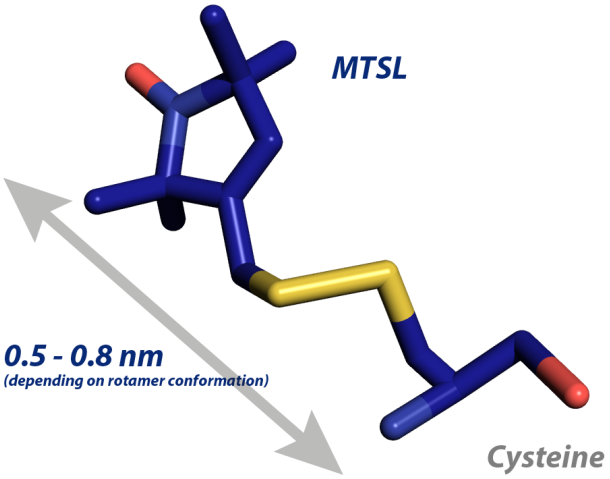

Figure 4.1: *One rotameric conformation of MTSL spin label bound to cysteine. The unpaired electron is located at the nitroxide group at the five ring.*

Rotamer library of spin labels The paramagnetic, stable spin label Methanethiosulfonate (MTSL) used in this work can change the dihedral angle between the nitroxide ring and the protein backbone around five different bond axes, which leads to a large set of rotameric conformations for an unconstrained label[III].

The MMM program includes an implementation of this set of rotamers into a rotamer library[101]. Spin labels can be attached to a molecular structure replacing a chosen residue. For each chosen residue position rotamer conformations that fit into the local surrounding are selected from the library. This provides an ensemble of multiple sterically allowed rotamers with corresponding population distribution. To take into account a low sample temperature (e.g. in frozen solution conditions), the rotamers with low conformation energy in the partition function are favored.

Based on these calculations, it is possible to choose any two (or more) labeled positions in order to calculate the distance distribution $P(r)$ with respect to the individual amplitudes, which then can be compared to the experimental distance data. The calculation does not, however, account for any conformational variation of the backbone – its sole basis is the rigid input crystal structure. In gen-

[III]MTSL can rotate around the C_α–C_β-axis, the C_β–S_1, the S_1–S_2, the S_2–$C_{1'}$ and the $C_{1'}$–C_2-axis connecting to the five-ring of the nitroxide.

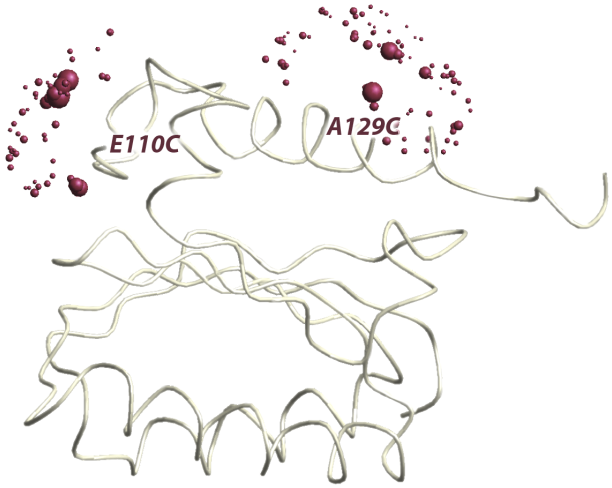

Figure 4.2: *Exemplary MTSL rotamer distribution of labeled E110C/A129C from the BlrB WT-structure (see section 4.3). The size of the spots signify the relative population. For both positions, two main orientations are visible which leads to a very narrow total distribution. Calculation done with MMM[101] for frozen solution conditions.*

eral, this leads to overly defined distributions as well as to different population proportions than observed in the experiment[97,101].

MTSSLWizard[111] is an alternative program designed as a PyMol[112] plug-in. It does not evaluate temperature, but always obtains a distribution by use of the whole rotamer library (leading to broader spread) and its output is limited. It was used as a check for consistency.

Structure modeling Within this work, several structure modifications have been calculated. To this end, a program was first developed by Thomas Barends from MPIMF Heidelberg to introduce mobile joints into the backbone of the DnaJ crystal structure, the dihedral angle of which could be rotated by means of Monte Carlo simulation. To guide the simulation, a pseudo energy was formulated as $E(\boldsymbol{r}) = -ln(P(\boldsymbol{r})) + W\, N_{clashes}$ derived from the ELDOR distance distribution with an additional weighted penalty to prevent clashes between C_α atoms. The objective was to learn with how few and which rotating bonds the experimental distance distribution could be explained. For this qualitative approach, tyrosines at the labeled positions modeled the MTSL molecules

– a discussion of the results will be given in the according chapter 5.

In this work, the simulation program was substantially expanded to find tangible model structures for BlrB. The most important modification was the addition of support for structures with attached rotamers at multiple positions to be able to compute the actual rotamer distances. The decision whether to accept a new random orientation was based on the comparison of the whole distance distribution of each pair with its respective experimental data. Because of calculation time considerations, this approach does not compute new rotamer distributions for the generated structure and is still an approximation. For most positions which are not directly situated at a moving joint, it was still a significant improvement. The clash penalty was extended onto C_z carbons, to account for large side chains of the residues arginine, tyrosine and phenylalanine. After computation, the new structure was stripped from all rotamers. To reconstruct the orientation of the original side chains from the crystal structure on the basis of the new backbone coordinates, the Kabsch/Procrustes algorithm[113] was implemented.

Additional structure modification has been done by hand in PyMOL[112] on the basis of the rotamer results of different autogenerated structures and the discussion given in chapter 5.

The newly proposed structures of BlrB could then be fitted to the SAXS traces by Anikó Udvarhelyi from the Heidelberg group and rated according to the fit quality in order to combine the experimental information. The result will be discussed in section 6.1.

Energy minimization The structure modifications on the proteins lead to non-ideal interactions with the proximal surrounding. To relax the modified residues into a local minimal energy while keeping the new overall conformation, the UCSF Chimera[114] molecular analysis program was used.

Chimera makes use of the force field routines from the Molecular Modeling ToolKit[115]. Hydrogens were added and charges assigned using the Amberff99SB parameter set for peptides and proteins[116].

The potential energy defined by the Amber functional takes into account distances, angles and dihedral angles to bonded neighbor atoms as well as van-der-Waals interaction and electrostatic interaction between all atoms in the molecule.

The geometry of the protein was kept fixed except for the moved joints. 500 Steps of steepest descent with 0.01 Å variation removed bad contacts with adverse potential energy. Then the local minimum was searched with 100 steps of conjugate gradient minimization with 0.02 Å variation.

Sequence alignments The alignment of multiple BLUF domain sequences in chapter 6 was performed using the ClustalX2[117] algorithm and JalView[118].

The proteins which contained additional effector domains were truncated to the BLUF domain part. The proteins used with their accession code in brackets: *Rhodobacter sphaeroides* BlrB [Q3IYE4], BlrA [Q3IV98], AppA [Q53119]; *Klebsiella pneumoniae* BlrP1 [A6T8V8]; *Synechocystis* Slr1694 [P74295]; *Escherichia coli* YcgF [P75990]; *Thermosynechococcus elongatus* Tll0078 [Q8DMN3].

4.3 Samples

Site directed spin labeling

This method is the prerequisite to the analysis of non-paramagnetic biomolecules with EPR and ELDOR.

By mutation of the protein sequence, artificial cysteine residues can be introduced at positions supposed to be affected by conformational changes or not well determined by a crystal structure. These cysteines can be labeled with MTSL nitroxide spin label which forms a disulfide bond that is reversible only under strong reducing conditions[119,120,121]. Other related spin labels like Maleimido-proxyl and -tempo can be used, which form an irreversible thioether-bond at their lower five-ring with the cysteine[IV] but are less stable under light. Out of this reason MTSL was chosen for spin labeling, but in the crosslinking experiments, this thioether-bond formation reaction was utilized. Multiple cysteine mutations could lead to formation of unwanted S–S-bonds or the replacement removed an otherwise important residue from the protein. A function assay is therefore important to verify the success of this procedure.

Both *T. thermophilus* DnaJ and *R. sphaeroides* BlrB contain no natural, accessible cysteines (see appendix for sequences, BlrB C60 is far inside the flavin

[IV] They can also interact with lysines at pH above 7.5.

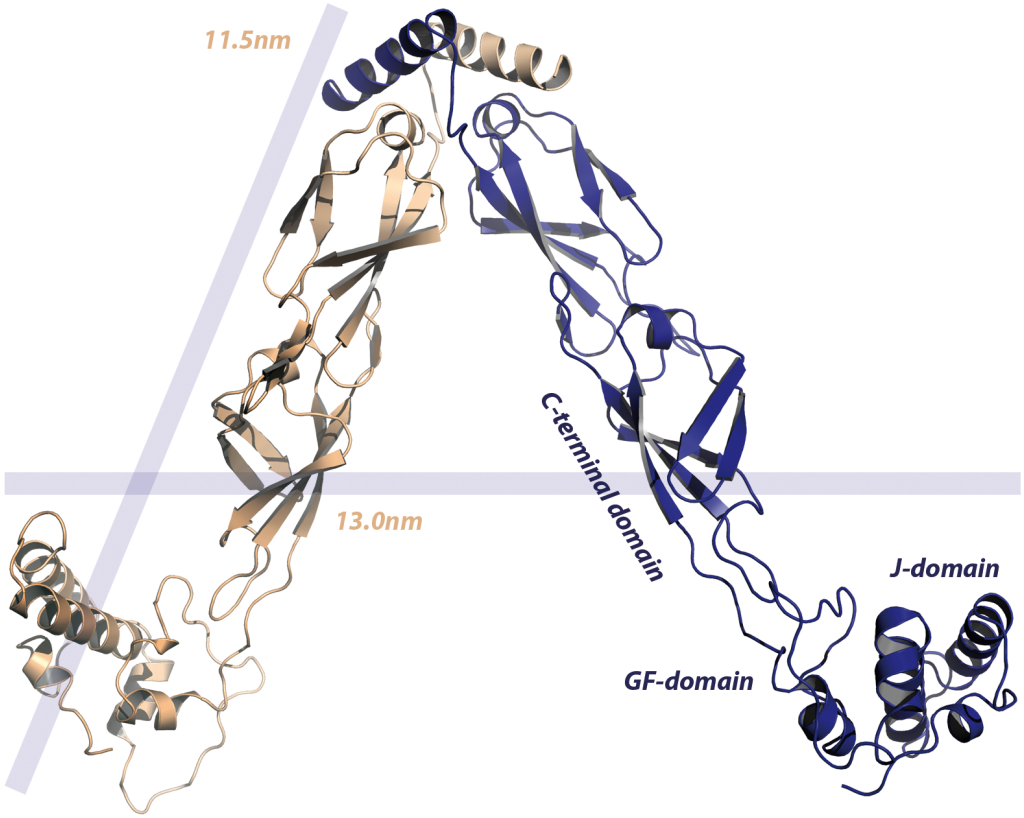

Figure 4.3: *Crystal structure of* T. thermophilus *DnaJ*$_{\Delta 108-114}$. *It consists of 280 amino acids per monomer (273 for the Delta-mutant) and has no cofactors. The molecular weight of one monomer is 31 kDa.*

binding pocket), so the well-proven method using cysteine mutations together with MTSL was used for the protein samples examined in this work. The functional assay for cysteine mutated DnaJ was the ATPase-activity, while for BlrB mutants the flavin cofactor red shift was the deciding factor. In both cases, all manufactured mutants were functional.

The DnaJ samples have been manufactured by Thomas Barends and Andrea Steinmetz, the BlrB mutants were created by Elisabeth Hartmann, all from the MPIMF Heidelberg.

DnaJ

The first crystal structure of *T. thermophilus* DnaJ (figure4.3) comprising the C-terminal domain as well as the J- and GF-domains has been solved by the Heidelberg group and is submitted together with data from this work. *T. thermophilus* DnaJ consists of three domains, the N-terminal J-domain surmised to interact with DnaK (residues 1-74), connected to the GF linker domain (residues 81-110) by a poly-Prolin helix and the C-terminus with its V-shaped dimer interface. One monomer of the full length protein has a molecular mass of 31kDa.

NMR spectroscopy has shown the GF-domain of DnaJ/Hsp40 to be unfolded and in disorder relative to the J-domain[27,28,29,32] and its influence on ATPase activation specificity was proven in *E. coli* DnaJ[38]. The crystallization of the *T. thermophilus* DnaJ protein was only possible by first constructing the crystal of the sole N-terminal J/GF part up to residue 114. No conclusive density could be found for the residues $108 - 114$, which would connect GF to the C-terminal domain. Subsequently, a full length deletion mutant ($\Delta_{108-114}$) was created and only then diffraction density could be obtained for all residues of GF. This *Delta* mutant was found functional in refolding assays.

Figure 4.4 shows the structure of the DnaJ GF/J-section. GF is situated on top of the J-domain like a wound spiral with a tight hydrophobic interaction of six of GF's seven phenylalanines[V] and a tyrosine are all directed towards the center of the J-domain like single teeth on a zipper or velcro tape. In the J-domain, this spiral motive continues, only here tyrosines are predominant. The strongly hydrophobic core suggests a very stable conformation in watery solution. In contact to a hydrophobic substrate, however, this coiled conformation could easily be unrolled.

To understand the effect of the GF domain conformation on the selectivity and activity of the DnaJ protein, it is necessary to examine the protein in watery solution. For this purpose, several cysteine mutants have been introduced into the J- and GF-domains of the full length protein.

[V] These seven phenylalanines are counted up to F101. One additional phenylalanine near F109 is cut away in the DnaJ$_{\Delta 108-114}$ construct.

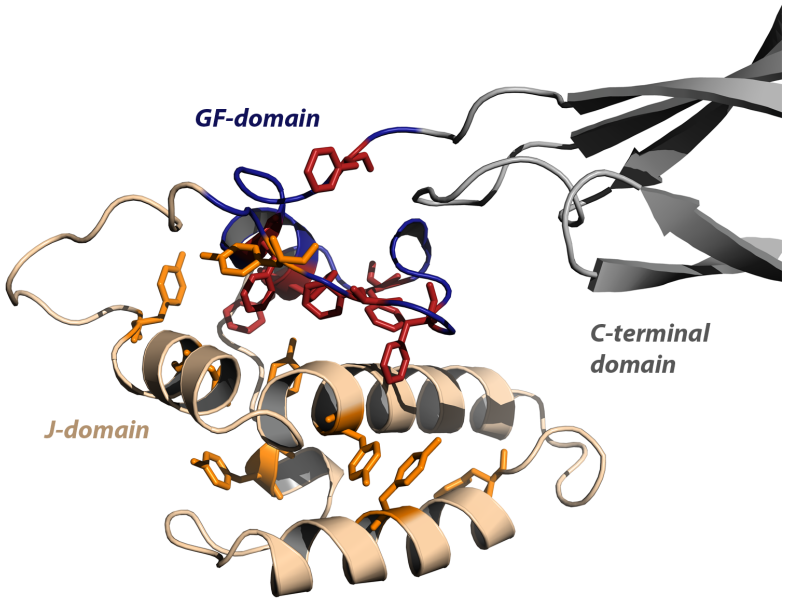

Figure 4.4: *Crystal structure detail of the N-terminus of DnaJ$_{\Delta 108-114}$. The GF-domain is colored blue. Shown in red are the Phenylalanines of the GF-domain, in orange the Tyrosines from J, constituting the hydrophobic center.*

Crosslinking These mutants have been examined in crosslinking experiments by Andrea Steinmetz from MPIMF Heidelberg. (1,4)Bismaleimide butane, a 1.2 nm short linker, binds selectively to the thiol group of cysteines with the same irreversible reaction as Maleimido-proxyl (s.a.). To prevent it from interacting with lysines at higher pH, the pH was kept at below 7.5. This crosslinker is added to the solution and given time to form bonds. Excess linker is then washed away. Now, with DnaJ and bound crosslinker, any interlinked tetra- and higher multimers are excluded via gel filtration and the dimeric protein is denatured, destroying the dimer interface at the C terminus. Subsequently, the sample is placed on a gel again to separate by molecular weight. The experiment resulted in large amounts of dimeric DnaJ, which has been captured by the crosslinker, even though the crystal structure would not have allowed it, indicating increased flexibility in solution (figure 4.5). The highest amount of crosslinking yield was attained with the S86C-mutation, suggesting its surrounding to be especially suited for the formation of the sulfur-carbon bond.

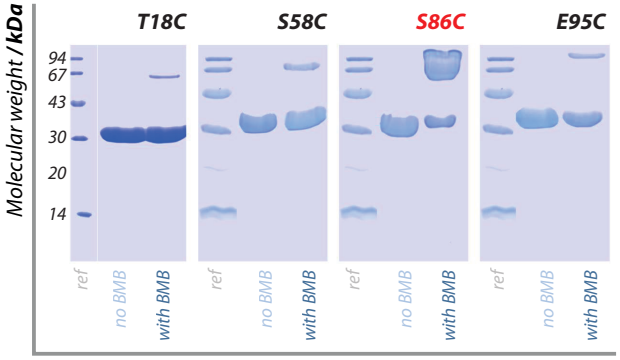

Figure 4.5: *Crosslinking experiments of several DnaJ$_{full\,length}$ single mutants, done by Andrea Steinmetz from MPIMF Heidelberg. For details, see text.*

Luciferase refolding assays In following assays of DnaJs stimulation of DnaK ATPase activity[21], the S86C mutant's result was slightly increased compared to the wild type yield. Several mutants with artificial cysteines in the GF- and J-domain modulated the effect of DnaJ concentration on the activity of DnaK, demonstrating the GF-domain's crucial impact for the interaction. The

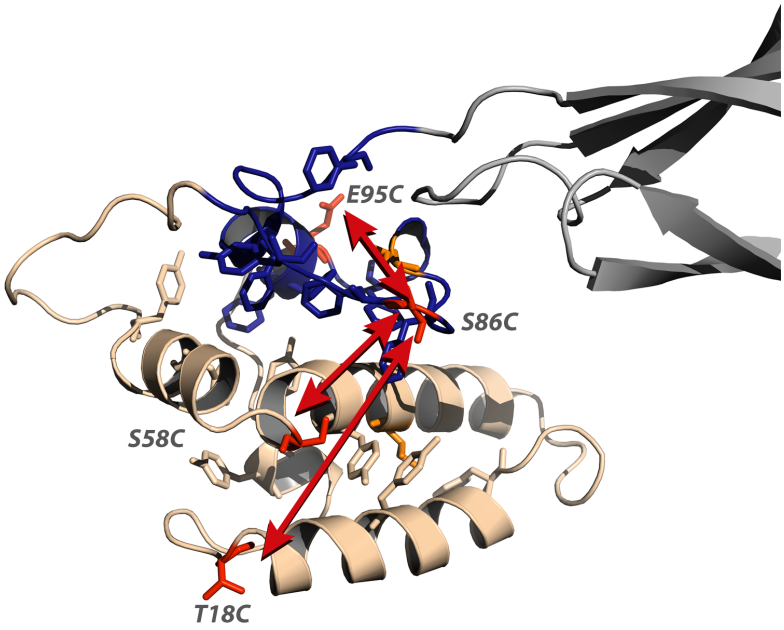

Figure 4.6: *Crystal structure detail of the N-terminus of DnaJ$_{\Delta 108-114}$. Highlighted in red are the three double mutant positions anchoring at S86C in the GF-domain.*

S86C/E95C double mutant with both cysteines within the GF-domain was responsible for the strongest change with a marked fourfold increase of ATPase activity at low 0.16µM DnaJ concentration and a more than threefold decrease at high concentrations of 3.2µM. Other mutants inverted this trend.

The aforementioned Delta mutants performed at about 80% the rate of their full length analogs.

ELDOR mutants To investigate whether an unfolded GF-domain produces the necessary additional flexibility or whether the J/GF-section is conserved in its crystal structure in frozen solution, several double-cysteine mutants were created to be examined with EPR spectroscopy.

S58C/S86C Serine is sterically very similar to cysteine, so the $S \rightarrow C$-mutation is comparatively unintrusive. S58 is situated inside the J-domain, while S86 is located in the center of the GF-domain. The crystal structure predictions for the distance distribution of this double mutant is below 2 nm. Since struc-

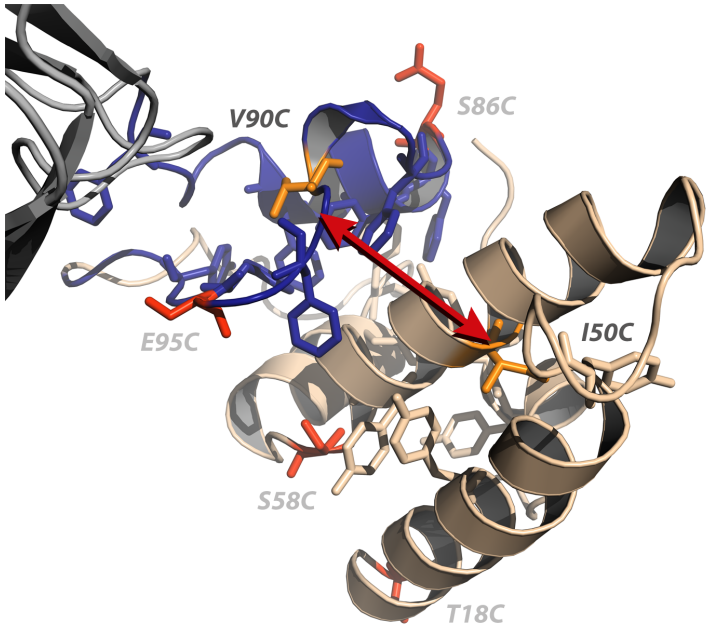

Figure 4.7: *Crystal structure detail of the N-terminus of DnaJ$_{\Delta 108-114}$. Highlighted in orange is the position of the label pair I50C/V90C.*

tural alterations of the GF-domain will only increase the interspin distance, this mutant is well suited to examine the conformation of the GF-domain to J-domain interface.

T18C/S86C The dual mutant T18C/S86C serves the same purpose as S58C/S86C with T18C located at the beginning of the first long alpha helix within J. It is better suited for detailed ELDOR analysis with its crystal structure distance within the optimal ELDOR range of 2-5 nm.

S86C/E95C To look at the internal GF-structure, this S86C/E95C double mutant was created. If the GF-domain unfolds between these two positions, a discrepancy to the crystal structure distance is expected. In addition, E95C is at the beginning of a two-turn helix up to P103. A change in tertiary structure would very probably affect the whole helix and thus E95C's rotamer distribution.

I50C/V90C After scanning the DnaJ crystal structure with MMM, a pair of amino acids was found with very few rotamers and inside the optimal ELDOR interspin distance interval. This pair was designed to permit study of the monomeric as well as inter-monomeric distances due to its defined rotamers. It also continues the principle to choose one label position in the J- and one in the GF-domain.

I50C/V90C in storage complex The DnaJ•DnaK•DafA stable complex mentioned in chapter 2 has been constituted with this I50C/V90C full length DnaJ. If DafA as an efficient pseudo-substrate would trigger the DnaJ GF-domain to unfold, the experiment would show a deviation from the signal of the above-mentioned sample alone in frozen solution.

As it exists solid evidence from gel filtration and analytic ultracentrifugation that DnaJ is a dimer in solution, this sample was assembled with the additional purpose of identifying the stoichiometry of the DnaJ•DnaK•DafA complex.

Single mutants Two single mutants have been labeled for EPR, S58C and S86C. Their main application will be the determination of the label mobility with RT cw-EPR. If the GF-domain is unfolded and disordered, S86C should have a significantly faster motion than S58C.[122,123]

Sample conditions The buffer used in all protonated samples was 25 mM HEPES and 25 mM KCl at pH=7.5. It contained 50% Glycerol. The concentration was between 180 mM and 280 mM for the DnaJ monomer. All samples were shock frozen and stored in liquid nitrogen.

The deuterated samples were buffer exchanged via centrifuging in a membrane concentrator. To obtain the correct pH in the deuterated buffer, protonated buffer of pH 7.5 without glycerol was dried by condensation, then refilled with D_2O, which ensured the according pD value. Deuterated Glycerol was added after the buffer exchange.

BlrB

The BLUF protein BlrB from *R. sphaeroides* consists of 140 residues, which form a compact protein centered around a five stranded beta sheet. Two parallel al-

Construct	Mutation	Domains
DnaJ$_{full\,length}$	S58C	J-domain
DnaJ$_{full\,length}$	S86C	GF-domain
DnaJ$_{full\,length}$	T18C/S86C	J/GF
DnaJ$_{full\,length}$	S58C/S86C	J/GF
DnaJ$_{full\,length}$	S86C/E95C	GF/GF
DnaJ$_{full\,length}$	I50C/V90C	J/GF
DnaJ$_{full\,length}$in complex	I50C/V90C	J/GF
DnaJ$_{\Delta 108-114}$	I50C/V90C	J/GF

Table 4.1: *List of all DnaJ mutants.*

pha helices α_1 and α_2 are attached to one side and constitute the flavin binding pocket together with the connecting loops. This is the *'body'* of the protein. A mostly helical C-terminal domain (the *'tail'*) is connected to β_5 and begins roughly at residue S98. The crystal structure[4] shows it to be attached to the beta sheet perpendicular to the strands, rendering the whole protein very compact, nearly spherical.

Small angle X-ray scattering (SAXS) measurements of BlrB were performed by Anikó Udvarhelyi (MPIMF Heidelberg) with highly concentrated sample solutions[VI]. The dark adapted sample features an effective radius of gyration R_g=1.76 nm[VII] which is considerably larger than R_g=1.50 nm calculated from the structure. After light activation a further increase was recorded together with incremental disorder. Indications of sample aggregation were concentration dependent, growing stronger with increasing concentration. However, the lowest

[VI] SAXS sample concentration ranged from c=250 µM to 10'000 µM.
[VII] Derived with the *Guinier approximation*[124]

concentration used in the SAXS experiments corresponds to a well but highly concentrated ELDOR sample; it should be negligible in the EPR experiments.

A second crystal structure has been solved by the Heidelberg group for BlrB W92N. It was created with the purpose of advancing the Tryptophan92 inwards/outwards-discussion quoted in chapter 2 and it showed a completely different conformation of the helical tail. Additionally, the helix α_{3B} is significantly longer than in the partly disordered tail of the WT-structure. Both crystal structures will be used to understand the ELDOR measurements.

The first batch of ELDOR samples were measured with a relatively low concentration of 75 µm as well as with a higher c of 250 µM (S58C/A129C, E110C/A129C and W92N-equivalents). After standard background correction, the distance distributions were equivalent, thus all other samples have been measured in the optimal ELDOR concentration range of 200–250 µM.

The buffer for all BlrB samples consisted of 25 mM Tris at pH 7.5 with 2 mM $MgCl_2$, 2 mM EDTA and 50 mM KCl. The solvent contained 28% Glycerol and 1 mg/ml Bovine Serum Albumin (BSA) to prevent aggregation after illumination.

The protein was illuminated at 4–8°C for 1.5–2 minutes with a strong *Luxeon DS46* 3 W blue LED, its radiation centered around 455 nm with a spectral half width of 20 nm. Then, the sample was shock frozen in liquid nitrogen (LN_2) under light. For the dark adaption, the samples were kept at 4°C in complete darkness for 6–16 hours and then also frozen in LN_2, still in the dark.

S58C/A129C In the crystal structure, the distance from $S58C$ to $A129C$ spans across the whole body and tail of the protein. It is therefore a direct monitor of any reorientation or extension of the tail helices.

S58C/R95C The pair $S58C/R95C$ measures the dimension of the body as it reaches from the beginning of helix $alpha_2$ to the last, fifth beta strand. This probe is especially important for the further examination of the surmised $W92$-reorientation into or out of the flavin binding pocket in the vicinity of R95.

E110C/A129C The tail of BlrB has a different orientation in the WT crystal structure than in the $W92N$-mutant structure. As this part of the protein

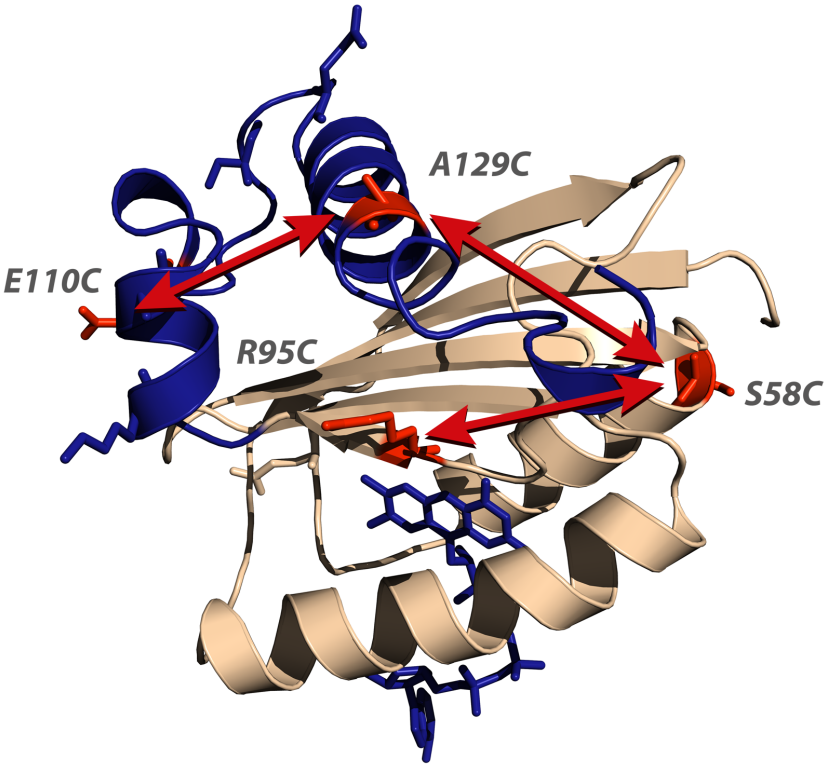

Figure 4.8: *Crystal structure of BlrB WT with indication of the label positions S58C, R95C, E110C and A129C in red. The BlrB core is colored in wheat, the C-terminal region in blue.*

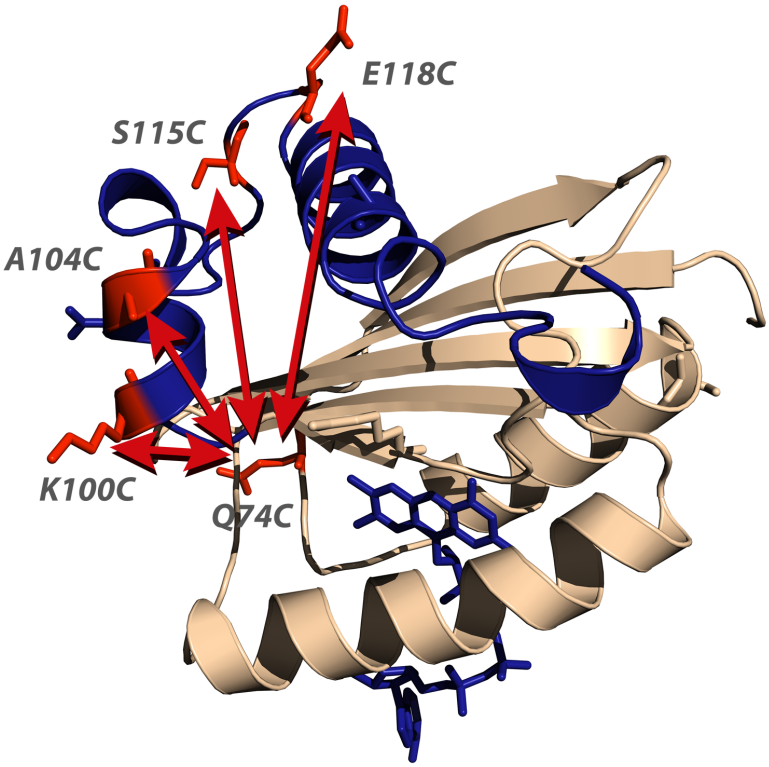

Figure 4.9: *Crystal structure of BlrB WT with a red color indication of the label positions Q74C in the body (wheat) and K100C, A104C, S115C and E118C in the tail (blue).*

seems to be the most dynamic, it is expedient to measure the dimension of the wedge-shaped α_{3B} to α_4–conformation.

Q74C To isolate the actual positioning of the tail conformation, several labels were placed along the C-terminal part paired with the common anchor $Q74C$. $Q74C/S115C$ and $Q74C/E118C$ report the distance from the end of α_{3B} and the beginning of α_4 to Q74C. $Q74C/K100C$ and $Q74C/A104C$ should provide information about the orientation of α_{3A}.

V31C/S98C The different bending of $S98$ in the wild type structure and that of the $W92N$-mutant motivate the creation of this control sample, which is a probe for the β_5– conformation from a different angle than $S58C/R95C$.

Construct	Mutation	Positions
wildtype	Q74C	α_2
wildtype	S98C	β_5
wildtype	V31C/S98C	$\alpha_1 \leftrightarrow \beta_5$
wildtype	S58C/R95C	$\alpha_2 \leftrightarrow \beta_5$
wildtype	S58C/A129C	$\alpha_2 \leftrightarrow \alpha_4$
W92N	S58C/A129C	$\alpha_2 \leftrightarrow \alpha_4$
wildtype	E110C/A129C	$\alpha_{3B} \leftrightarrow \alpha_4$
W92N	E110C/A129C	$\alpha_{3B} \leftrightarrow \alpha_4$
wildtype	Q74C/K100C	$\alpha_2 \leftrightarrow \alpha_{3A}$
wildtype	Q74C/A104C	$\alpha_2 \leftrightarrow \alpha_{3A}$
wildtype	Q74C/S115C	$\alpha_2 \leftrightarrow \alpha_{3B}$
wildtype	Q74C/E118C	$\alpha_2 \leftrightarrow \alpha_4$

Table 4.2: *List of all BlrB mutants.*

Single mutants Two single mutant samples have been measured, $S98C$ and $Q74C$, both in dark adapted and illuminated state in order to find hints on possible dimerization or multimerization.

4.4 ELDOR distance distributions

This section provides a qualitative explanation for the distance distributions which occur from different geometries of label pairs. The examples discussed here will be relevant for the construction of the BlrB model structure (chapter 6).

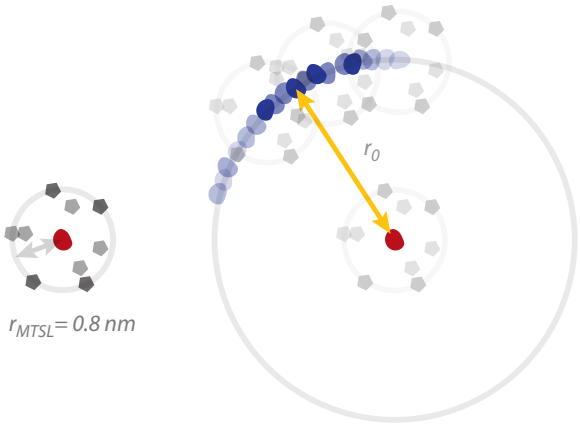

Figure 4.10: *The most general situation for spin label geometry is a sphere. The possible spin positions are denoted as red and blue clouds, the corresponding backbone C_α backbone positions with grey pentagons.*

With two labels that are restrained to a single rotamer and thus possess only one spin position each (which will just be called 'rotamer' for simplicity), the general case without any information is illustrated in figure 4.10. The single rotamer position in space (depicted as a cloud) can originate from a variety of different rotameric conformations for the spin label, generating a filled sphere of possible C_α-positions (indicated by pentagons) limited by the maximum stretch of the label.

With a measured narrow interspin distance r_0, the second rotamer can be on the surface of a hollow sphere with its thickness determined by the width of the

r_0-signal. The C_α–C_α orientation is very undefined without further information.

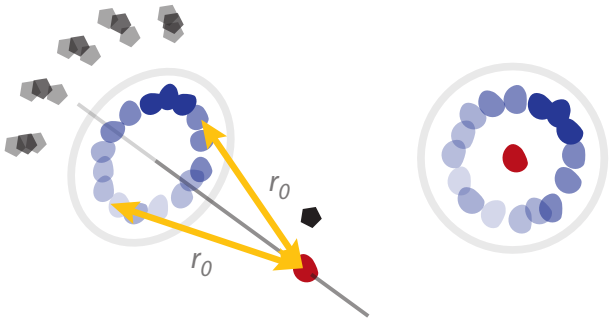

Figure 4.11: *With information about the protein size and the backbone rigidity at both labeled C_α positions, the possible C_α–C_α conformation can be narrowed down considerably (indicated with black pentagons).*

A crystal structure provides this information even to the extent of allowing generation of explicit rotamer configurations. ELDOR can then be employed to interpret the differences observed in solution with respect to the rigid structure, which can indicate functional relevance of certain protein domains. It can further detect conformational changes before and after a triggered reaction.

Figure 4.11 depicts a known configuration of the red label. The rotamer arrangement for the blue label was estimated from the crystal standard and due to steric constraints, only a subset of all possible orientations is applicable. This is a substantial improvement and can be correlated to further measurements on other label pairs. The paragon of such analysis is the publication by Altenbach, Hubbell et al. from 2008[125] on Rhodopsin. The distance distributions of the label pairs were very narrow, so the dark state rotamers were used for the activated state conformation search.

Broad distributions

The analysis of BlrB, however, demands the understanding of broad distance distributions and whether they can be appropriated to a fixed conformation or whether disordered conformations have to be assumed in solution. In the following examples, the rotamer distribution of BlrB Q74C will be used as point

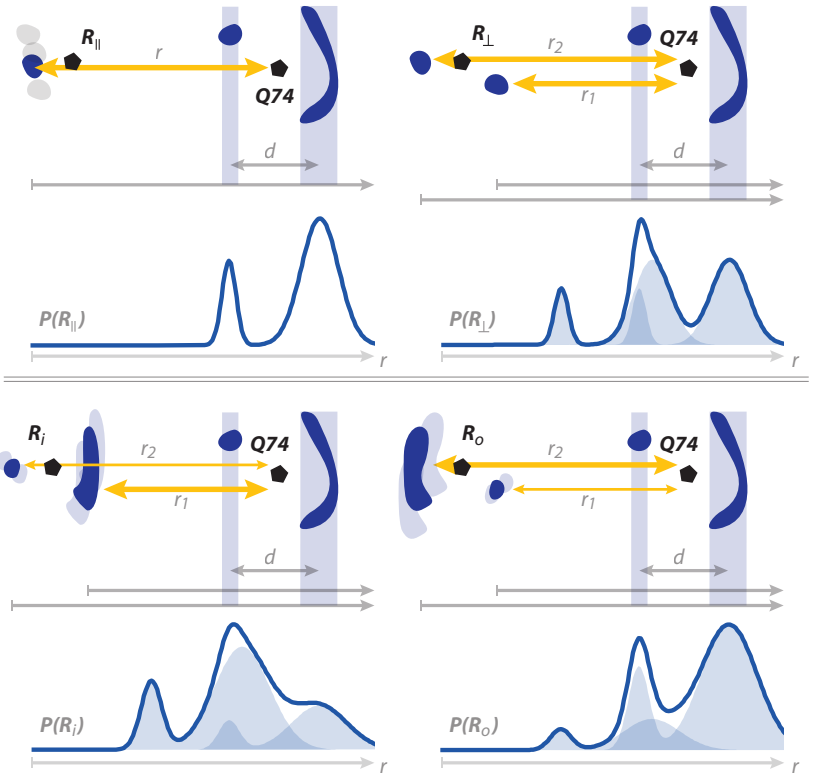

Figure 4.12: *Different examples of a label pair geometry and their according distance distributions below. The backbone positions are indicated with pentagons, the spin positions from the different rotamers are blue clouds. The observed distance distributions are depicted as solid lines below with its constituents in shaded blue.*

of reference, because the samples containing this mutation are pivotal for the ELDOR analysis. It is determined from the wildtype crystal structure of the consistent BLUF core. Each label pair geometry is depicted along the mean interspin vector.

We take the reasonable assumption of exciting all rotamers of both label positions. Then the observed distance distribution is a convolution of both spin conformations (each rotamer in Q74C interacts with each rotamer in R according to the population density).

Different R, same constituent spectrum In the case of one defined rotamer for R, as shown in the upper left of figure 4.12, the observed distance

distribution shows the projection of the rotamer distribution of Q74C onto the interpin vector. Its rotamers are located mainly in one plane with its main populations along one edge and in one other corner of a square with Q74C C_α at its center (indicated as a pentagon). Without loss of generality, the angle of the figure plane has been chosen accordingly.

Taking the mean of the first and last position observed yields an estimate for the backbone distance that is shifted by the displacement between R and its rotamer. In this orientation, a variation of the R rotamer perpendicular to the interspin vector would result in a similar spectrum.

The upper right example shows two R rotamers of equal population. Both project the Q74C rotamers onto their interspin vector. As the interspin vector r_1 is much shorter than r_2, its origin is shifted and we observe three peaks (both single projections are indicated in shaded blue). If no artifacts occur, taking the mean of the first and last observed rotamer results in a very good estimate for the C_α–C_α distance, because in both positions the rotamers are spread equally to both sides along the mean interspin axis.

Focusing on Q74C alone, the distance within its rotamer arrangement from top left to bottom right is 1.5 nm, which is about the maximum variation one can encounter at a single label site labeled with MTSL. This leads to three consequences:

a) In principle, broad conformations of up to 3 nm in width (which is huge by ELDOR standards) can have one rigid orientation for both C_α's. It is very likely for such broad conformations that contain several distinct peaks.

b) An estimation of the C_α–C_α connection length just from the observed distances is only feasible for a very broad image of at least 2.5 nm in width. Below, an asymmetric displacement is possible and additional information necessary.

c) If two peaks are more than 1.5 nm apart with nothing in between, they belong to different label pairs (or different conformations of the same).

The bottom examples from the same figure 4.12 vary the proportion of both rotameric fractions and use broadened constituents for the distance distribution to simulate stronger variation of the R rotamers. It produces substantially different spectra from very similar situations. For the interpretation, always the whole constituent spectra have to be considered.

The bottom right distance distribution is very similar to several actually ob-

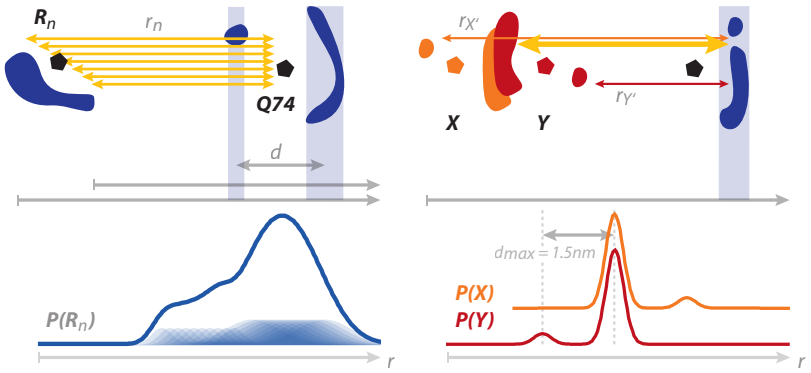

Figure 4.13: *(left) Continual distribution of rotamers for R. (right) Narrow conformations have high variance for the C_α positions without further information.*

served BlrB Q74C/R spectra (Q74C/K100C and Q74C/E118C).

Special cases Figure 4.13 shows two special cases. To the left, a continuous rotamer distribution along the mean interspin vector for R is shown. This can be described as many small constituent spectra stepped by small increment and added to form a smooth distance distribution (or one could switch the vantage point, but which is not useful in the BlrB case for known Q74C geometry but unknown for R). Even though this spectrum is very smooth, it is caused by just one backbone orientation. This example distribution is similar to the observed Q74C/A104C spectrum.

The right example in figure 4.13 does not contain Q74C, but a generic sharp conformation of rotamers along the mean interspin vector. Here two different cases for the other label pair have been sketched with one dominant and narrow rotamer population. The result in both cases is largely the same spectrum, even though the position of X and Y can differ by up to 1.5 nm. Small additional contributions can carry valuable information, but have to be distinguished from fitting artifacts due to insufficient S/N. In any case, additional information is mandatory to interpret such a conformation.

Information valuable for such cases includes a) Knowledge about the position of neighboring residues, which are connected by a known element of conserved secondary structure. If two residues are on the same side of a helix, the

interpretation is different from if they occupy opposing sides. b) Possible interfacing regions. If case X would imply a helix or loop hovering in a rather large distance above a beta sheet, but case Y would fit it onto the surface, case Y is the more probable. Of course, cross-referencing is mandatory here.

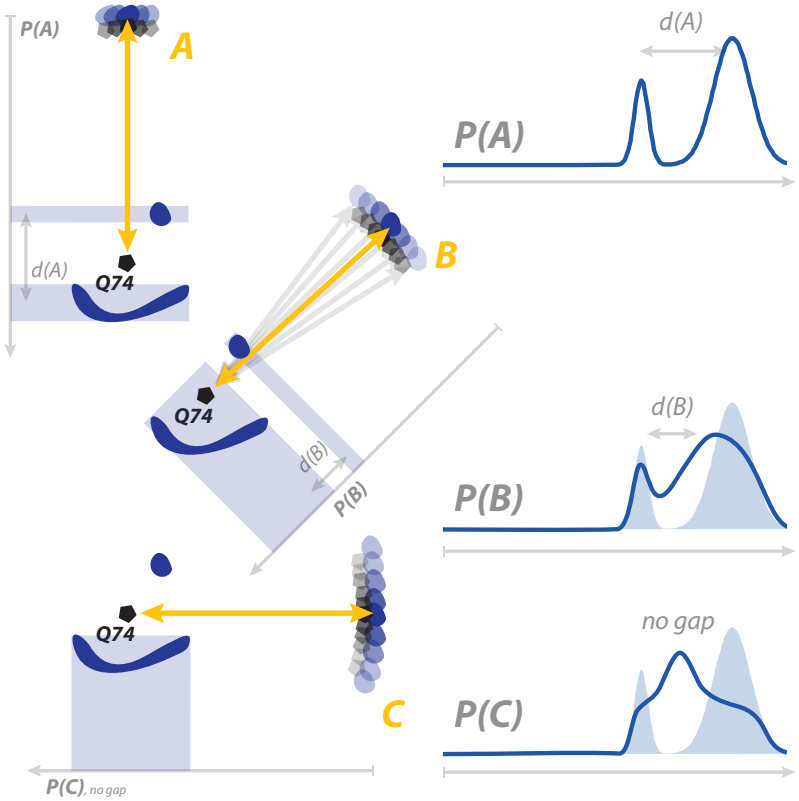

Figure 4.14: *Rotation of R in the Q74C rotamer plane. (left) Orientation. (right) Distance distributions (solid lines). For comparison, $P(A)$ is plotted in shaded blue in cases B and C.*

Same R rotamer, different constituent spectra In the following examples, R is restricted to one rotamer, thus showing the constituent spectrum with which more complicated R rotamer configurations are convoluted.

Figure 4.14 shows three exemplary conformations of Q74C/R with the same mean distance, but at different angles inside the rotamer plane. Due to the special rotamer configuration of Q74C, an interspin vector tilted out of the rotamer plane (see next paragraph) will cause a reduction of the width of the constituent

spectrum, but the same arguments regarding its shape apply.

Case A is already discussed in the very first example. In case B, R has been rotated by 45°and in C by 90°, while Q74C stays fixed. Qualitative distance distributions are depicted on the right, showing a decrease of the gap between both Q74C populations in the constituent spectrum. From B to C, the gap is completely gone (whether the peak for the corner-population is visible now strongly depends on the population along the edge of the Q74C rotamer square).

While a conformation like C is difficult to evaluate and has high insecurity in the lateral orientation, the gap in the observed distance distribution for a conformation R in the vicinity of A can be analyzed. Here, the size of the gap is strongly dependent on the rotation angle. Thus, if the constituent spectrum can be identified and the gap measured, an estimate for the orientation angle for R can be found.

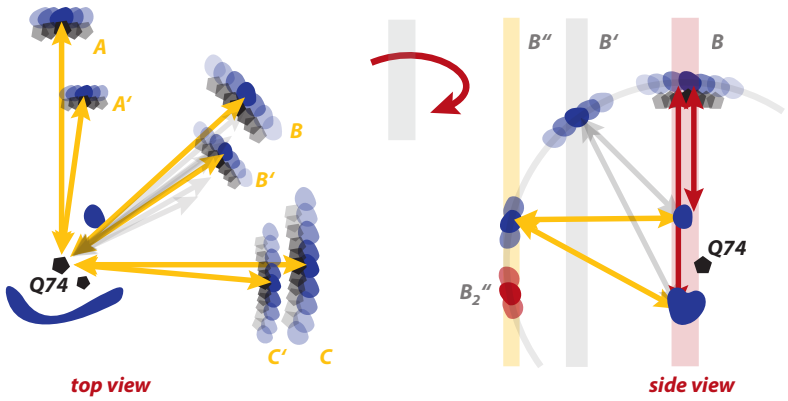

Figure 4.15: *Orientations A', B' and C' (left, shaded gray in right picture) emerging out of the Q74C rotamer plane (shaded red, right). For details, see text.*

Third dimension, narrow constituent spectrum As we have seen in the first example (figure 4.11), the observed narrow distance distribution r_0 of two isotropic rotamer configurations cannot define its relative orientation. This is very different for such highly anisotropic rotamer configurations as from Q74C.

In all given examples, a small section of the initial globe leaning out of the rotamer plane remains as error margin (figure 4.15, side view). With a larger

tilting angle, the overall width of the constituent spectrum decreases, scaling the effects already discussed. The spectra for A' to C' will differ in the same way from each other as the spectra A to C.

With a further significant increase of the tilting angle, the distance difference between both Q74C rotamer populations becomes very small and its internal structure will be less defined. This is outweighed by the fact that such a B" orientation already is very well defined, because only a small solid angle with possible positions for B" remains as shown in figure 4.15 on the right. Here the spectra are very narrow and the internal structure is reduced to pyramidal vs. sawtooth shape. B" would have a sawtooth distribution peaking at higher distances, while $B"_2$ (red) would have a sawtooth peaking at its lower distances.

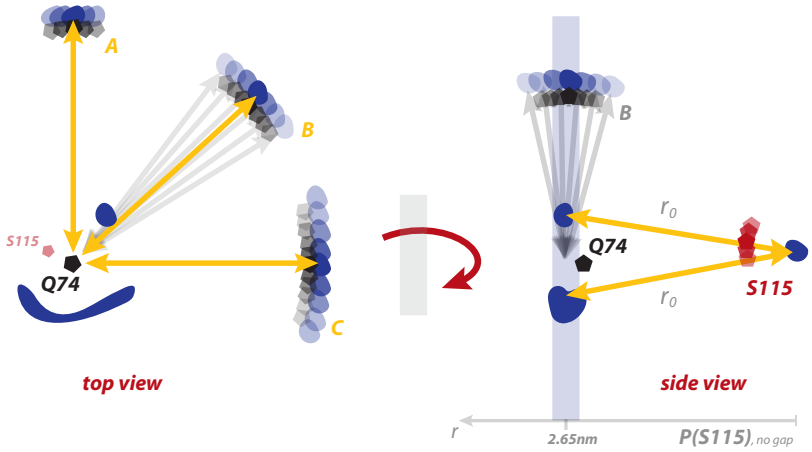

Figure 4.16: *Exemplary interspin configuration leading to a narrow observed distance distribution (indicated in side view picture, right), even though Q74C possesses a broad variety of spin label rotamers. For details, see text.*

In final consequence, this leads to the situation shown in figure 4.16. The rotamer configuration of Q74C is flat and the constituent spectrum of Q74C becomes extremely narrow although it has large rotamer variation in other directions.

With a complete, actually observed distance distribution still as narrow, only few R rotamers can be present. These have to be in parallel to the Q74C plane and be in a very defined location to prevent trapezoidal interaction geometry as

in A' to C'. Therefore in this special case, the position of such a second label is determined in all three dimensions relative to Q74C by this one double mutant with given geometric considerations and its observed distance r_0. This is the case for Q74C/S115C and is discussed in chapter 6.

Chapter 5

DnaJ

The work on *T. thermophilus* DnaJ presented in this chapter serves the purpose of proving in how far the recently obtained crystal structure for $DnaJ_{\Delta 108-114}$[I] is meaningful in frozen solution or whether the GF-domain is disordered as in *E. coli* DnaJ. As quoted in chapter 2, the GF-domain has been found crucial for DnaJ's substrate binding specificity. To further investigate the high affinity of *T. thermophilus* DnaJ to DafA, a labeled DnaJ•DnaK•DafA complex has been examined.

5.1 Full length DnaJ

Double mutants Figures 5.1 to 5.4 show the ELDOR measurements of all four investigated $DnaJ_{full\,length}$ double mutants (T18C/S86C, S86C/E95C, S58C/S86C and I50C/V90C) in frozen solution at 80 K. The time traces have been background corrected, and the resulting dipolar evolution functions depicted have been simulated using Tikhonov regularization with a broadening parameter $\alpha = 10$ (as described in the methods chapter 4). The acquired distance distributions are compared to the rotamer predictions from the crystal structure.

The ELDOR trace from figure 5.1 features a sharp intensity drop after only 0.05–0.1 µs. The corresponding distance region of this main contribution lies below 2 nm, which is already below the optimal ELDOR range and required the short distance Kernel correction 4.8 for its evaluation. Still, a quantitative de-

[I] Solved by Thomas Barends from MPIMF Heidelberg

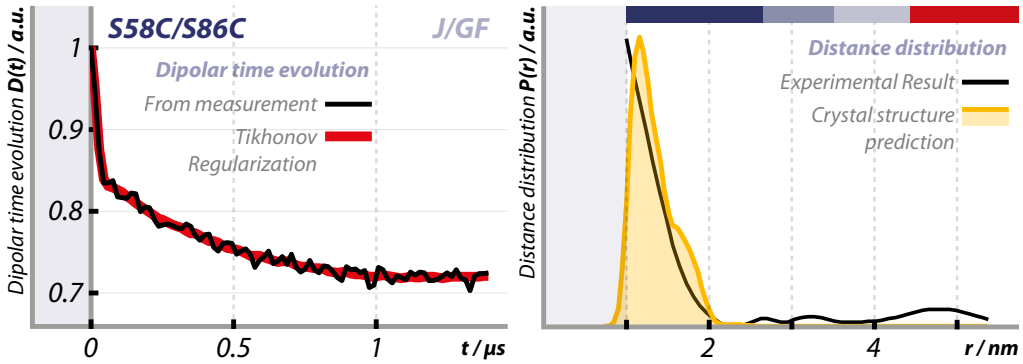

Figure 5.1: *S58C/S86C ELDOR measurement. The background corrected time trace (left, black) with its Tikhonov fit (red, $\alpha = 10$) shows a first echo intensity drop at below 0.1 µs. Thus, the resulting interspin distance distribution (right, black) has its major intensity below 2 nm. This matches the prediction from the crystal structure (shaded yellow).*

termination of the dipolar interaction is not possible in this case. The distance between S58C in the J-domain and S86C in the GF-domain is so close, that due to strong dipolar coupling and exchange broadening (see chapter 3) the EPR spectrum of this sample exhibits a dipolar/exchange broadening of more than a factor of two compared to a singly labeled sample or one of the other double mutants (see later figure 5.15).

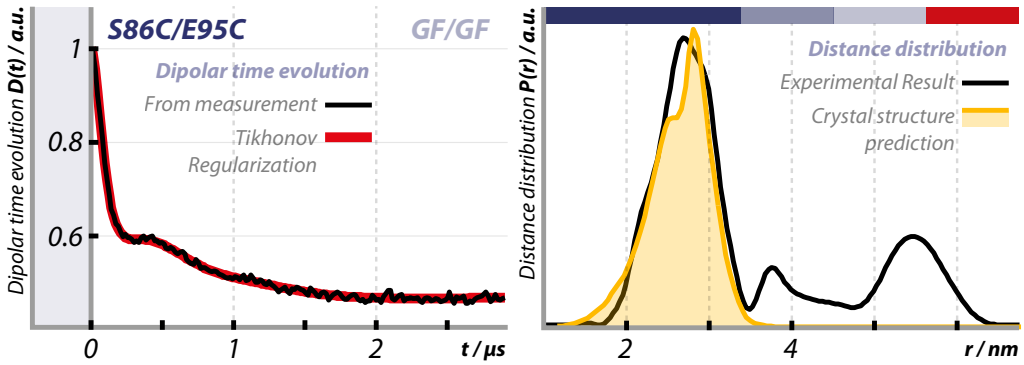

Figure 5.2: *S86C/E95C ELDOR measurement. The dipolar evolution function (left, black with red fit, $\alpha = 10$) has a major oscillation period $T \approx 0.5$ µs, which corresponds to the large peak around 2.8 nm also seen in the crystal structure (right).*

In spite of the limitations of ELDOR in this case, the rotamer prediction is well reproduced by the measurement and confirms a tight interaction between the J/GF domains in this region.

The ELDOR trace of S86C/E95C with both labels within the GF-domain possesses one very defined modulation as its dominant feature (figure 5.2). In the distance distribution it emerges as a narrow peak centered at 2.7 nm. This main peak confirms the X-ray structure in the region between S86C and E95C, as its narrow shape from 2 to 3.3 nm matches the rotamer prediction exactly. Additional modulation intensity generates stray contributions between 3.8 and 5 nm as well as another prominent peak at 5.5 nm that will be interpreted later.

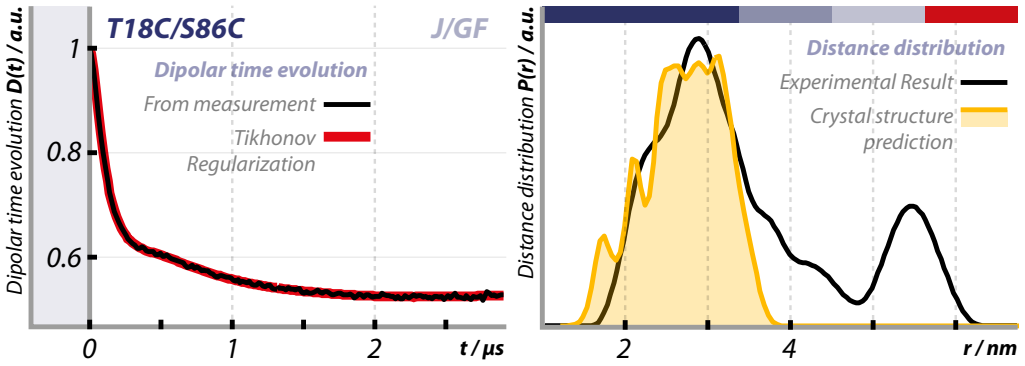

Figure 5.3: *T18C/S86C ELDOR measurement. Its dipolar evolution function (left, black with red fit, $\alpha = 10$) has less pronounced features than that of S86C/E95C, leading to a much broader distance distribution (right, black), which is in accordance with the crystal structure prediction (shaded yellow).*

In comparison to S86C/E95C, T18C/S86C with one label in the J-domain and one in the GF-domain produces a more dampened modulation in its time trace (figure 5.3), resulting in a broader distance distribution with suggested bimodal shape. The additional contributions are the same in this experiment as in that for S86C/E95C. The broader main peak observed in the experiment is reproduced by the rotamer calculation.

All three of these samples contain the S86C mutation. As mentioned in chapter 4, the according DnaJ single mutant exhibits a major increase in crosslinking

yield of at least 50% of the whole educt compared to 8-10% for the T18C, S58C and E95C single mutants at most (quoted in methods chapter, figure 4.5).

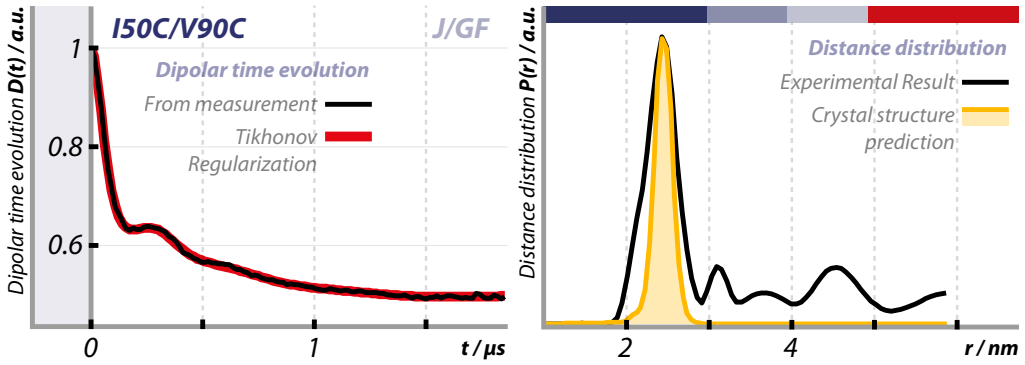

Figure 5.4: *I50C/V90C ELDOR measurement. This trace possesses a very defined structure (left, black with red fit, $\alpha = 10$) with three, nearly four completely visible oscillations. The resulting distance distribution (right, black) matches the rotamer calculation from the crystal structure (shaded yellow).*

To assure not to misinterpret effects of the serine86 to cysteine mutation present in all three specimens, I50C/V90C as a fourth sample has been investigated (figure 5.4). Its modulation is the most pronounced of all samples examined and produces a narrow, cone shaped main contribution at 2.3 nm with a slight shoulder to lower distances. It matches the correspondent rotamer calculation from the crystal structure with identical peak position, the distribution is only marginally broader. The additional occurring rotamer positions in the measurement imply slight backbone flexibility while the overall structure is highly conserved.

In addition, the modulation depth for the short main contribution corresponding to the crystal structure of nearly 0.4 is roughly the same for I50C/V90C as for T18C/S86C and S86C/E95C, where r is within optimal ELDOR-range. A modulation depth of 0.4 is already near to the theoretical maximum of 0.5 for a perfectly labeled double mutant under perfect experimental conditions[95], as discussed in chapter 4. Therefore the vast majority of the J/GF-sections in solution adopt the J/GF conformation seen in the crystal structure. No major conformational change or unfolding of the GF-domain below E95 can be related to the S86C-mutation in particular.

In S58C/S86C the labeling efficiency seems to be reduced, probably due to singly labeled double mutants hindering the attachment of a second label at so close a position during the labeling procedure.

Regarding the S86C/E95C sample, a conservation up to even higher residue numbers can be reasoned, as E95C's rotamers would be substantially affected not only by changes at lower residue numbers, but also at higher numbers. The region above E95 comprises three phenylalanines and a leucine that have strong van-der-Waals interactions with the other central hydrophobic residues of GF. In watery solvent, decomposition of this apolar center is unlikely, but a dislocation might occur. Such a dislocation would displace or at least redistribute E95C's rotamers and thus the observed distance distribution. However, the distribution is an *exact* fit to the rotamer calculations, rendering major occurrences of such structural changes unlikely.

So far, the perfect agreement of the short distance contributions from the measurements and the corresponding rotamer calculations for all four investigated samples implies a high degree of structural rigidity and conservation.

The origin of the small fractions at intermediate distances as well as the prominent peak at $r \approx 5.5\,\mathrm{nm}$ in the result for T18C/S86C and S86C/E95C, and at $r \approx 4.7\,\mathrm{nm}$ in the distance distributions of I50C/V90C and to a lesser degree in S58C/S86C cannot be assigned yet. With T as length of the corresponding timetraces, the ELDOR distance relation[II] reproduces the r-values of these distance peaks. As we have mentioned in chapter 4, such artifacts are caused by longer distances in the sample which are not resolved. They probably are caused by interactions between two DnaJ monomers.

There is solid evidence for *T. thermophilus* DnaJ forming a dimer in solution from analytic ultracentrifugation and gel filtration[III] and it is seen in this state in the crystal structure. However, with such a large distance between both J/GF-regions (shown in figure 5.5), short time traces like those shown in this section (2 – 3 µs) cannot resolve these intra-dimeric distances, which would cause an oscillation with $T \approx 8\,\mu\mathrm{s}$ or more.

[II] $r \approx \sqrt[3]{52 * T/\mu\mathrm{s}}\,\mathrm{nm}$

[III] Private communication by Jochen Reinstein and Thomas Barends from MPIMF, Heidelberg

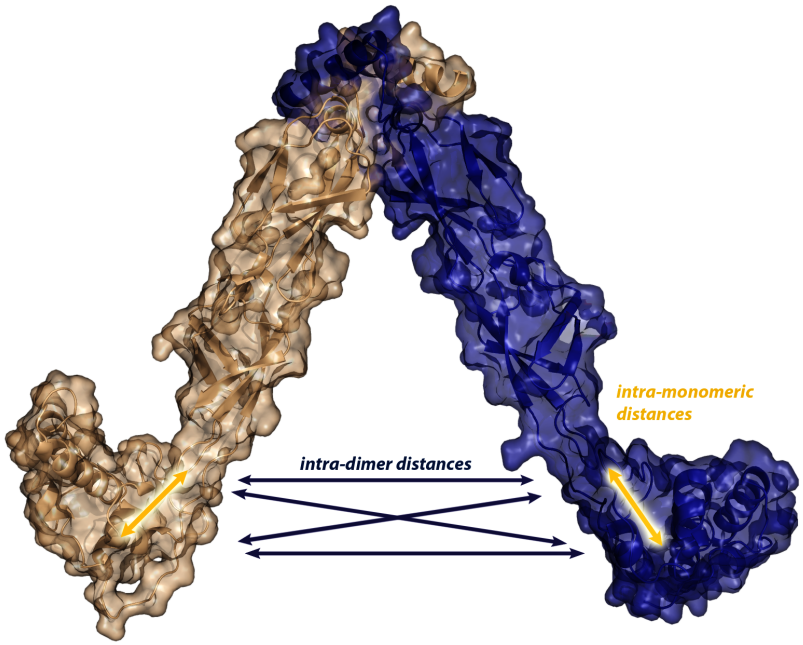

Figure 5.5: *DnaJ$_{\Delta 108-114}$ crystal structure. The dipolar interaction geometry for an exemplary double mutant is marked.*

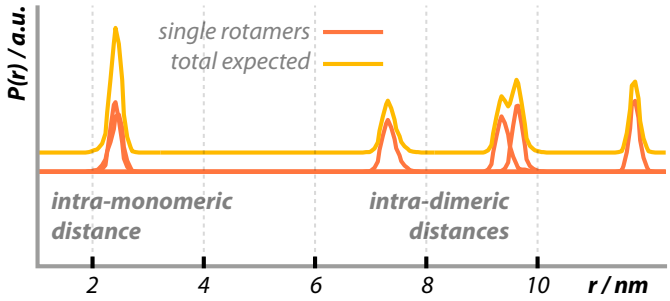

Figure 5.6: *Distribution prediction based on the whole DnaJ dimer structure for I50C/V90C. In the crystal structure, the area between 3 and 7 nm interspin distance is void, in contradiction to the experiments.*

Single mutants To clarify the issue, an ELDOR experiment on the labeled single mutants S58C and S86C in deuterated solvent has been performed (see figure 5.7), because these mutants can categorically only exhibit intra-dimeric interactions. They produce very smooth time traces of equal modulation depth (which is another indication of no possible explanation for the increased S86C-yield within the means of EPR), and therefore cast broad distance curves. It

demonstrates a substantial variation of the intra-dimeric distances even down to the intermediate distance ranges between 3 and 5 nm, so all observed intensity besides the intra-monomeric crystal orientation in the double mutants can be explained by intra-dimeric interaction.

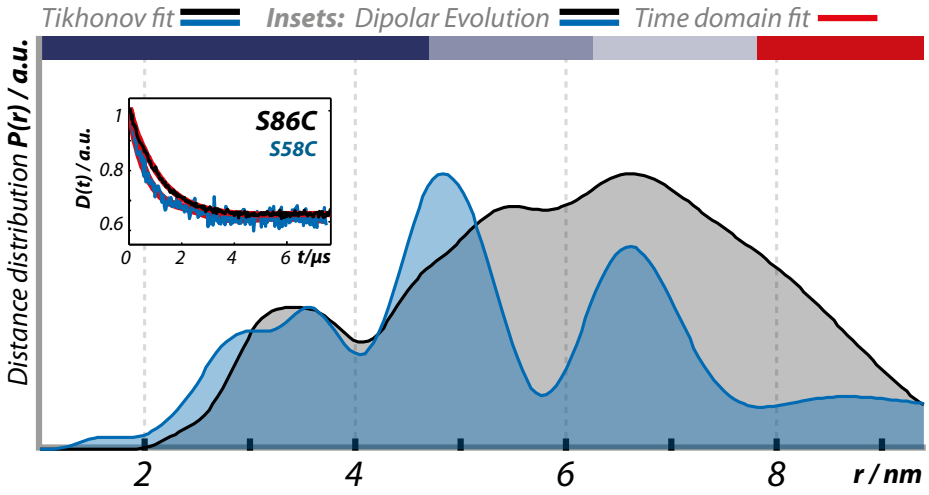

Figure 5.7: *Distance distributions of two DnaJ$_{full\,length}$ S58C (blue) and S86C (black) single mutants, $\alpha = 100$. Inset are the dipolar evolution functions, both samples have nearly the same modulation depth. $\Delta_{S86C} \approx 0.34$, $\Delta_{S58C} \approx 0.36$.*

5.2 DnaJ storage complex

Besides the issue of conservation/non-conservation of the crystal structure in solution, the question about DafA affecting the conformation of DnaJ in the process of the DnaJ•DnaK•DafA complex formation is addressed in this work. Samples of the complex have been assembled with labeled DnaJ$_{full\,length}$ I50C/V90C and investigated. In addition, the same mutation has been introduced into the DnaJ$_{\Delta 108-114}$ construct to compare the intra-dimeric interaction. The three different specimen will be abbreviated *'FL'* for DnaJ$_{full\,length}$, *'Complex'* for the DnaJ•DnaK•DafA-complex and *'Delta'* for the DnaJ$_{\Delta 108-114}$ deletion construct used for the X-ray crystal structure analysis.

Intra-monomeric distance As was found by reconstitution experiments, the complex can be reassembled with only J/GF-sections as DnaJ contribution, but not with only the C-terminal domain[IV], however it was not possible to determine the stoichiometry of this J/GF-part within the complex. With ELDOR, it can be examined in how far this interface modifies the internal J/GF-structure. I50C/V90C has been chosen to monitor the GF-domain in particular. Figure 5.8 shows the measurements of both Complex and additionally Delta for detection of the short intra-J/GF distance.

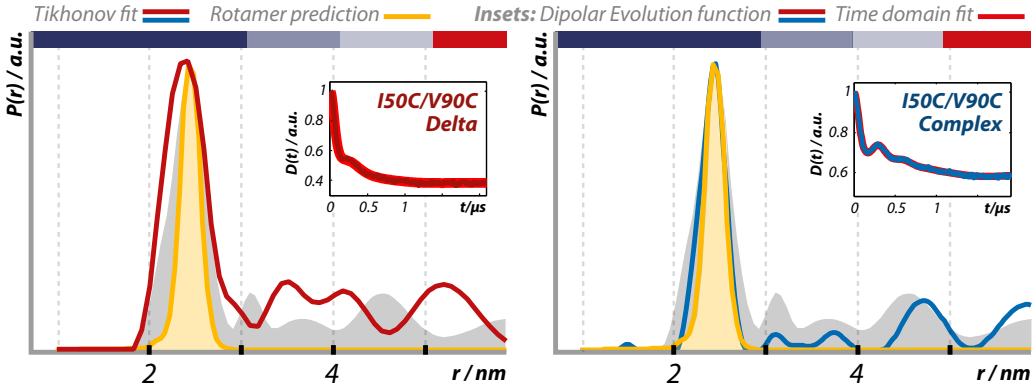

Figure 5.8: *Distance distributions for the Delta and Complex samples, $\alpha = 10$. In orange, the I50C/V90C rotamer prediction from the crystal structure and in gray the comparison to FL.*

While the expected peak is found in both samples, there are clear differences. The Complex shows a very long-lasting one-component modulation in its time trace, which results in an extremely narrow distance peak that perfectly matches the prediction from the rigid crystal structure. This implies the relevance of the J/GF-domain crystal conformation for the binding of *both* DnaJ monomers to the DafA substrate and DnaK. Otherwise, a two-component peak would be observed with half its constituents being in the wider rotamer configuration of FL. In the wider distance ranges, the time traces of both FL and Complex are similar. This will be discussed below on the basis of longer time traces.

Conversely, the intra-monomeric peak in Delta is marginally wider than in FL. The Delta construct exhibits a larger modulation depth already for the

[IV]Private communication by Andrea Steinmetz from MPIMF, Heidelberg

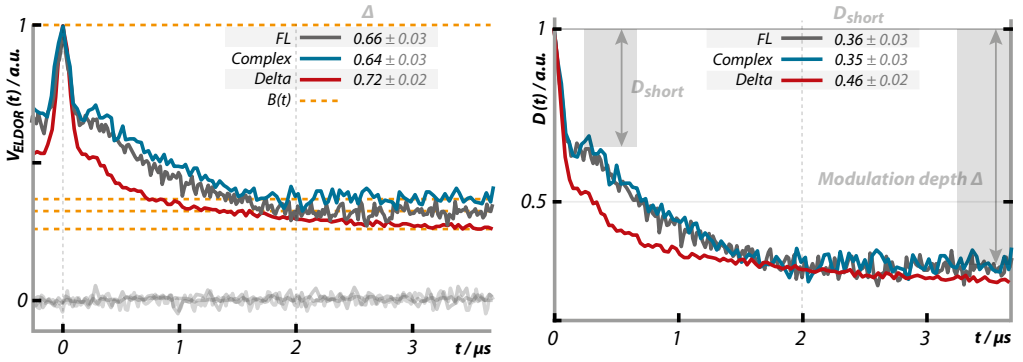

Figure 5.9: *(left) Raw ELDOR time traces of the three deuterated I50C/V90C-samples with $\tau_2 = 3.8\,\mu s$. The values for the overall modulation depth Δ are noted. (right) Time traces after noise correction. The values for the modulation at short times t are listed.*

short intra-monomeric interaction, but it continues for intermediate oscillation periods and will be discussed below. The changed modulation pattern produces more contributions between 3 and 4.5 nm, which must be caused by intra-dimeric interaction.

Intra-dimeric interaction The discussion of the DnaJ intra-dimer distances relies on the deuterated samples of FL, Complex and Delta[V]. With deuteration of the solvent, the limiting relaxation time T_m was prolonged by a factor of 1.4 in Complex and 1.8 in FL. The Delta sample was directly solvated in deuterated buffer after assembly and also had a higher concentration.

The observed differences in the time traces between Delta and Complex/FL are apparent on a longer timescale from figure 5.9. When comparing the ELDOR traces[VI] with a zero background correction (as we have to expect large distances that are not resolved, we can only correct the maximum position for noise by fitting), the modulation depth after one oscillation of the monomeric distance differs significantly between $D_{short} \approx 0.36$ for both FL and Complex and $D_{short} \approx 0.46$ for Delta. For long times $t \approx \tau_2$, the modulation depth for Delta is again larger than for the other two, while at 2 µs, the traces all overlap.

[V] See section 4.3 for the buffer exchange procedure.

[VI] The experimental parameters are consistent for all three traces as the EPR spectra coincide and the pulse powers, bandwidths, and positions were kept constant.

FL and Complex have nearly horizontal traces above 2 µs.

Before quantifying the difference in modulation depth D_{short} with equation 4.5, several factors have to be considered. Delta possesses a significantly increased amount of intensity directly adjacent to the intra-monomeric peak, which in turn contributes to its D_{short} much stronger than slower oscillating FL and Complex traces, when neglecting their intra-monomeric frequency. Additionally, there could be a small fraction of denatured protein or a different labeling efficiency, but it would be a coincidence that both FL and Complex feature the exact same amount of defects. A third possibility could be the Delta construct exerting additional constraints on the structure and a certain small, but equal amount of protein from all DnaJ$_{full\,length}$ samples including FL and Complex are in an unfolded GF state as presumed from before this study.

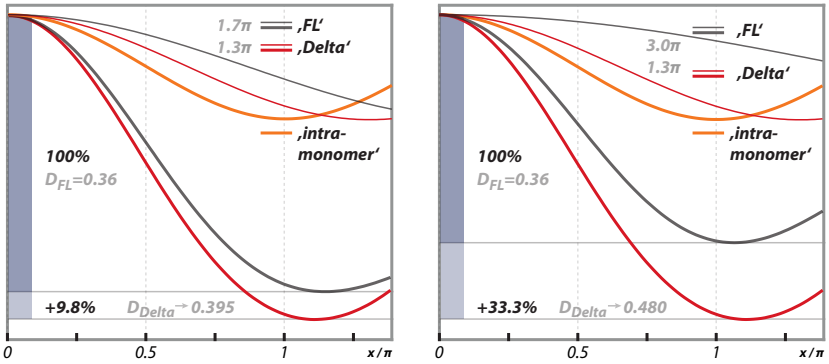

Figure 5.10: *Shown is the influence of additional neighboring cosine modulation according to equation 4.2 on the observed modulation. Constituent modulations scaled for clarity. (left)* $T_{Delta} = 1.3\pi$, $T_{FL} = 1.7\pi$. *The result is a 9.8% deeper observed modulation. (right)* $T_{Delta} = 1.3\pi$, $T_{FL} = 3.0\pi$. *This calculation can already explain the observed difference in modulation with just one neighboring spin interaction.*

With the raw numbers from figure 5.9, equation 4.5 produces a population difference of the monomeric crystal orientation of 13%. The (important!) fact of neighboring oscillation however, as illustrated in figure 5.10 for a conservative and a realistic example of still nearby oscillation, can already account for the difference on its own. Thus, the effect is not due to population differences, but to strongly reduced intra-dimeric spin-spin distance, misguiding the eye by mathematics.

This denotes an equivalent rigidity of the GF/J-monomers for Delta as for FL and Complex. In consequence of these arguments, there must be an equal amount of intra-dimeric interaction (the same amount of spins per monomer implies the same for the dimer) and the slope of the signal trace can safely be attributed to interaction with third molecules due to higher sample concentration (see chapter 4 on ELDOR background).

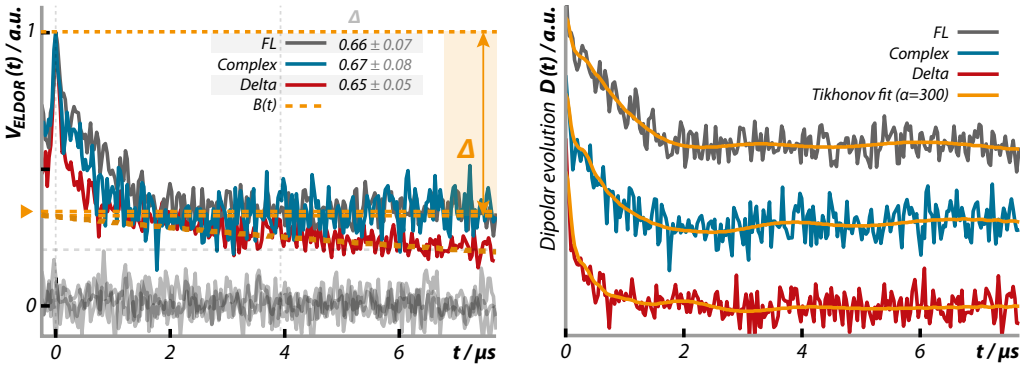

Figure 5.11: *(left) Raw ELDOR time traces of FL, Complex and Delta with $\tau_2 = 7.8\,\mu s$. The values for the overall modulation depth Δ noted from these traces after background correction are identical. (right) Tikhonov regularization fits with $\alpha = 300$ for the time traces. The corresponding distance distributions $P(r)$ are shown in figure 5.12.*

The long time traces depicted in figure 5.11 show worse signal to noise, but in combination with the knowledge from above about the intra-monomeric distance, meaningful distance distributions could be extracted (figure 5.12). The Delta trace has been background corrected, and in agreement with above considerations all three modulation depths Δ comprising intra-monomer and intra-dimer interactions are identical.

A final question remains about which fraction of the intra-dimeric interaction is actually resolved and how much intensity with longer modulation period could we expect in theory. Bode et al.[95] have shown that highly diluted, perfectly labeled spin pairs have a modulation depth of 0.5, spin triplets of 0.7 and spin quartets of 0.8. So our maximum modulation depth for monomer/dimer modulation depths is 0.8 against an observed 0.66. However, our intra-monomeric and single mutant intra-dimeric modulation has never exceeded 0.4. If this tendency is extrapolated, the observed maximum modulation depth $\Delta \approx 0.66$ fits

well to a spin quartet with reduced excitation efficiency. This implies that the majority of intra-dimeric interaction is resolved within the time traces acquired. It also suggests the S58C and S86C single label ELDOR distance distributions to contain nearly the whole variety of intra-dimeric interactions.

Figure 5.12 depicts the distance distributions acquired from Tikhonov regularization fitting of the 7.8 µs time traces of the three constructs. The L-curve criterion was less definite, therefore several regularization parameters have been plotted to show the tendency of the fit. In all three cases there may be additional, but smaller contributions at clearly separated higher distances, indicated in the figure. But as we have reasoned, the main proportion of intra-dimeric interaction is observed in the depicted frame.

Besides the known peak at 2.3 nm, clearly resolved in the short time traces of all three samples and already discussed above (superimposed), a dominant bimodal contribution from 5 to 7 nm is visible in FL (marked by the rounded line). It is confined on either side by clear voids (asterisks), and there only exists a small, additional contribution between 3 and 4.2 nm.

In complex, the small contribution below 3.5 nm mostly vanishes, which is already seen in the short time trace. Instead, a broad range of distances emerges between 3.8 and 7 nm with significantly more intensity in the intermediate distance regions as in FL.

The Delta distribution possesses a broader range of distance contributions with lesser contributions at large r (labeled by a dotted line) with no clear void within the confidence region. Here the main intensity is found in a continual range from the intra-monomeric peak up to 5 nm. By virtue of the modulation depth, this intensity still has to originate from intra-dimeric interactions.

Notably, both FL and Complex have no significant intensity between 7 and 8 nm, where artifacts from wrongly assigned background would be expected (as in the short time traces). The intra-dimer distances are thus concentrated in significantly smaller distance regions than seen in the crystal structure in all three samples with the extreme case of Delta having intra-dimeric interaction as close as the intra-J/GF distance. Still, the contributions in FL and to a lesser degree in Complex are constrained to smaller ranges than one would expect from isotropically oriented J/GF-sections connected to a rigid V-shaped C-terminal dimer interface.

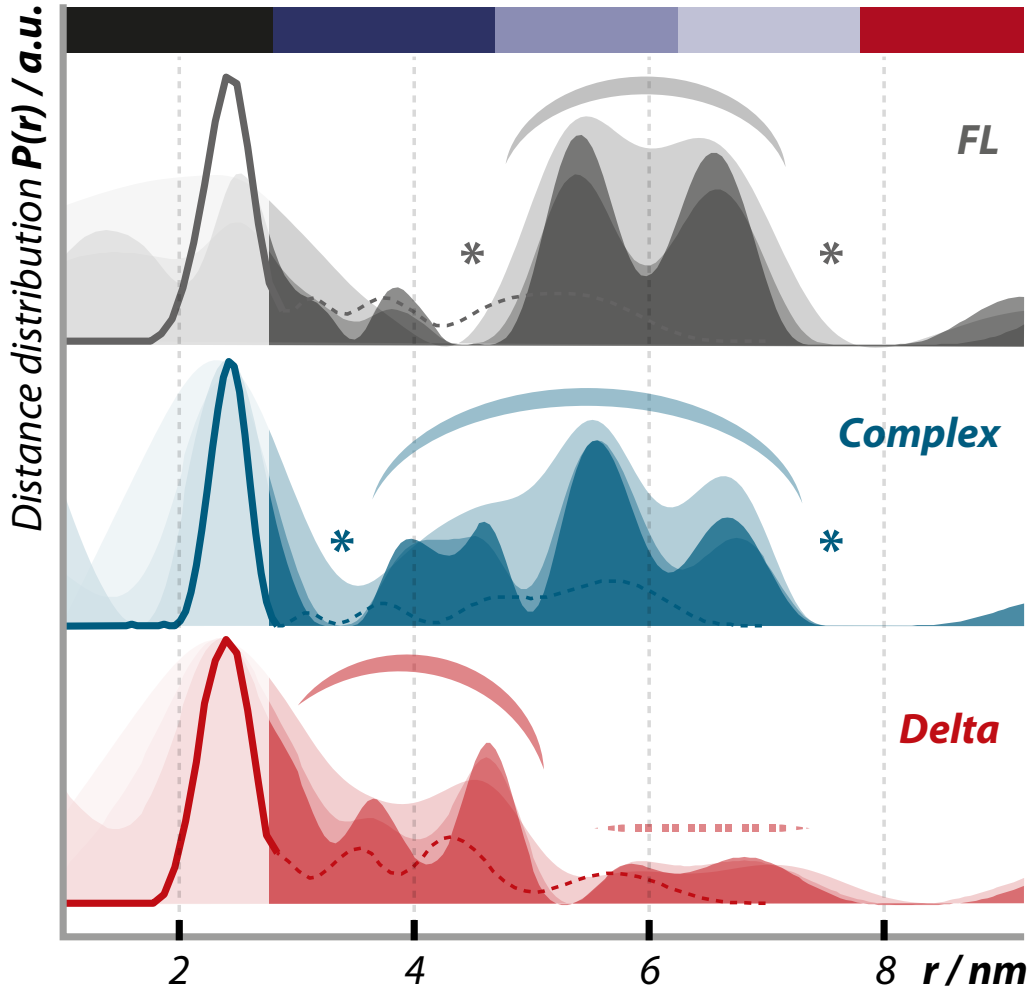

Figure 5.12: *Distance distributions from the 7.8 µs time traces shown in figure 5.9 with* $\alpha = 300$ *and the broader* $\alpha = 1000, 10000$ *are shown solid (The L-curve criterion for these time traces is not as strong, but the different distributions are consistent). Superimposed are the distance distributions from 5.8 & 5.4 with* $\alpha = 10$ *for the short distances. These are shown as dotted line above 2.7 nm. Predominant intensity is marked with a rounded line and asterisks mark voids in the distance distribution.*

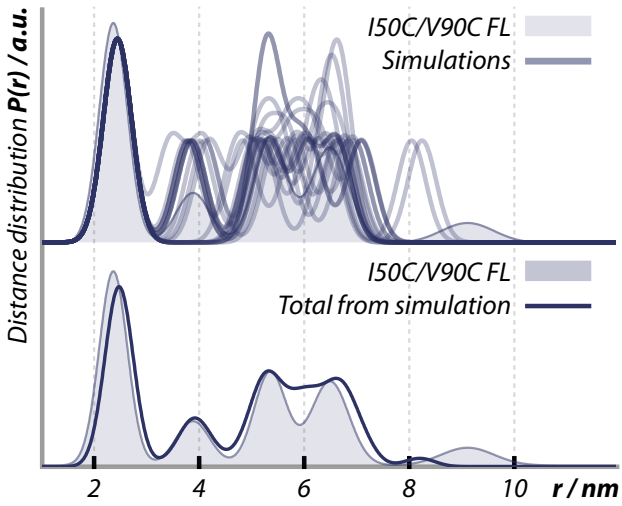

Figure 5.13: *Histogram of the calculated distances – best 20 out of 800. Variation was possible around the $N - C_\alpha$-axis of positions 108-114 from the structure (which would sterically translate to 115-121 in FL).*

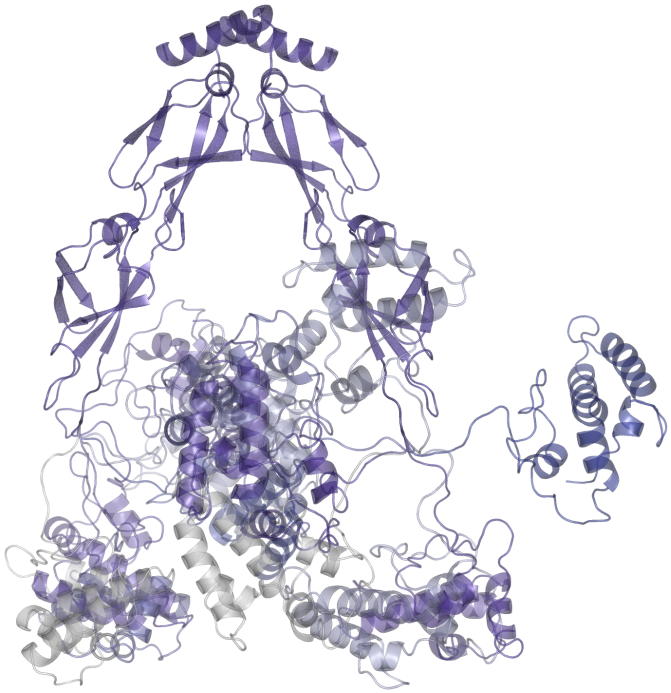

Figure 5.14: *DnaJ$_{\Delta 108-114}$ exemplary ensemble of calculated orientations. The J/GF-domains are nearly always closer to each other as in the crystal structure.*

Monte Carlo simulations To test, in how far and with how few modifications the observed intra-dimer distances could also be modeled by changing the quaternary structure of the crystal structure when rotatable N-C_α bonds above the GF-domain are introduced, a Monte-Carlo simulation was programmed by Thomas Barends from MPIMF Heidelberg. The structure was varied with a steric model generating pseudo energies as explained in chapter 4. A typical result is shown in figure 5.13 for variation of the initial C-terminal region from 115-121 (as a substitute for the deleted residues 108-114), and it can perfectly account for the observed distribution even down to 3 nm. Figure 5.14 shows an exemplary ensemble from the same simulation. The ELDOR constraint keeps both J/GF-sections mainly in the center between the two C-terminal domains or directly below in close distance to each other. A more condensed, but also variable quaternary conformation ensemble in solution in contrast to the pronounced V-shape in the crystal structure is therefore suggested by the measurements.

Room temperature cw-EPR To be able to observe the mobility of the spin labels in the examined mutants and thus to attain information about the rotamer configurations in consequence of the immediate surrounding of the spin labels, ambient temperature cw-EPR was performed.

The acquired spectra of all available DnaJ$_{full\,length}$ samples have been approximated with isotropic motion spectra using EasySpin[100] as discussed in section 3.6. The **g**- and **A**-coupling matrices were determined from a frozen solution W-band measurement of I50C/V90C to $\mathbf{g} = (2.0086, 2.0064, 2.0023)$ and $\mathbf{A} = (17, 18, 104)\,MHz$, common values for bound nitroxide[97] (see figure 5.15). From the spectra of T18C/S86C and S86C/E95C, 50% amplitude of S86C single was subtracted to provide estimates for the T18C and E95C single spectra, called 'T18C' and 'E95C'.

The MTSL at S86C has the highest mobility and shows least anisotropy, but its $\tau_c \approx 2.2$ ns is of the same magnitude as that of most other samples. 'T18C' and S58C are nearly as fast, 'E95C' is about 2 ns and I50C/V90C is considerably slower. The small anisotropy in S86C is also found in 'T18C', while S58C and 'E95C' produce distinct anisotropic shoulders. I50C/V90C has two label sites, and the best fit for two components ($\tau_{c1} = 15.8$ ns, $\tau_{c2} = 5.0$ ns) is depicted, which still requires strong anisotropy.

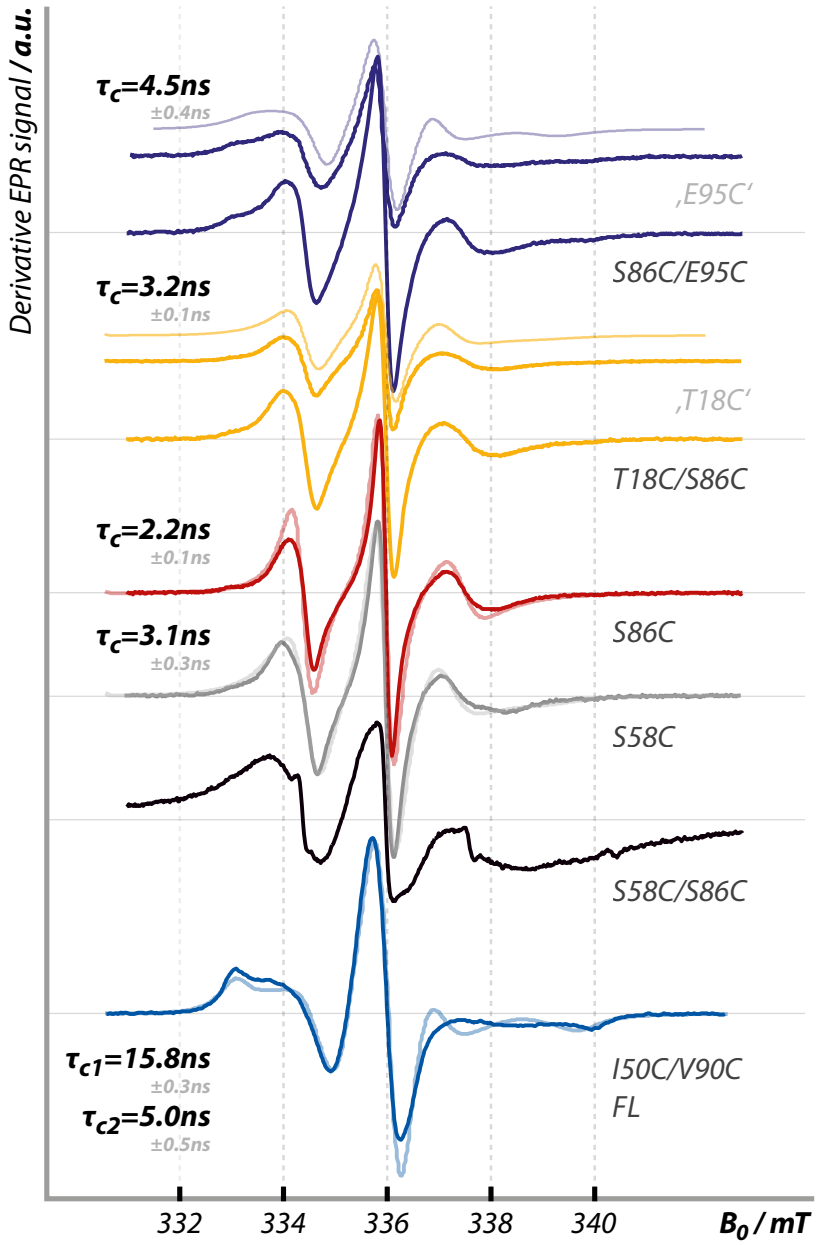

Figure 5.15: *Comparison of RT cwEPR spectra of all labeled DnaJ$_{full\,length}$ mutations. From the double mutants T18C/S86C and S86C/E95C, 50% of the S86C-spectrum has been subtracted before simulation (marked with 'T18C' and 'E95C'). $\mathbf{g} = (2.0086, 2.0064, 2.0023)$ and $\mathbf{A} = (17, 18, 104)\,MHz$, determined from a field-calibrated 80K W-Band measurement of I50C/V90C in protonated buffer.*

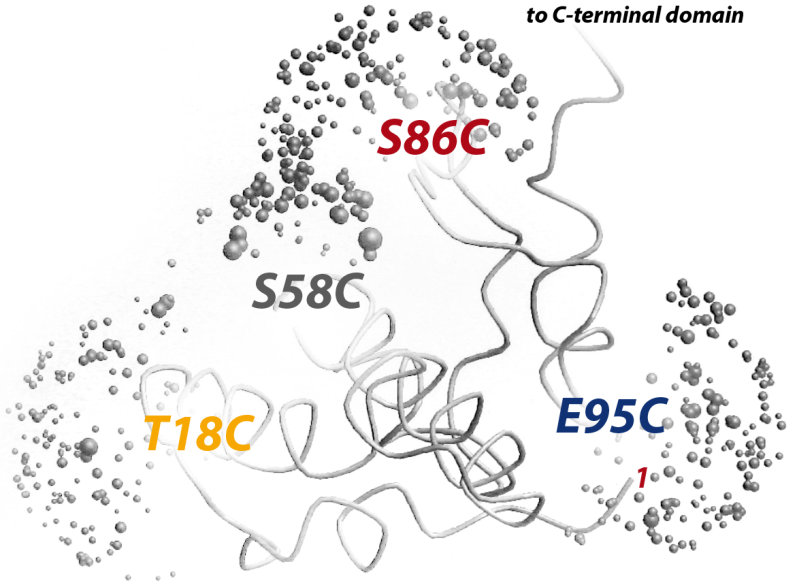

Figure 5.16: *Illustration of the DnaJ J/GF-region with gray spheres indicating rotamers of T18C, S58C, S86C and E95C, calculated for ambient temperature in MMM[101] - the bigger the spheres, the higher the proportional population. The N-terminus is marked with a red '1'.*

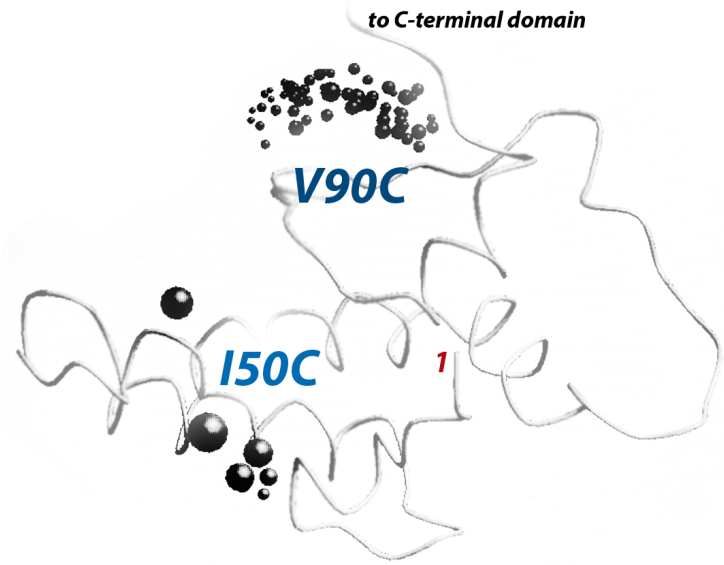

Figure 5.17: *The calculated ambient temperature rotamer distributions of V90C and I50C are very narrow and defined. Especially I50C has only few positions between which the spin label can move.*

The Figure 5.16 depicts the rotamer distributions of all labeled residue positions calculated for ambient temperature kT. Regarding the anisotropy of S58C and 'E95C', the it shows particularly constrained rotamers for S58C. The anisotropy in 'E95C' is likely caused by the N-terminus extending right into the cloud of rotamers. The small variation in the S58C rotamer configuration in comparison to S86C can also explain the different width of the observed distance distributions in the single mutants (see above, figure 5.7).

Figure 5.17 is from a different viewing angle and shows the rotamer predictions for I50C and V90C, making the identification of the slower component $\tau_{c1} = \tau_{I50C}$ possible, but also suggesting it having strong site exchange.

The S58C/S86C double mutant is a special case where extreme dipolar and exchange broadening in combination with high anisotropy occurs. Its spectrum also shows remaining free spin label as three small, sharp lines, which is an indication of unstable double labeling and could cause its reduced intra-monomeric ELDOR modulation amplitude.

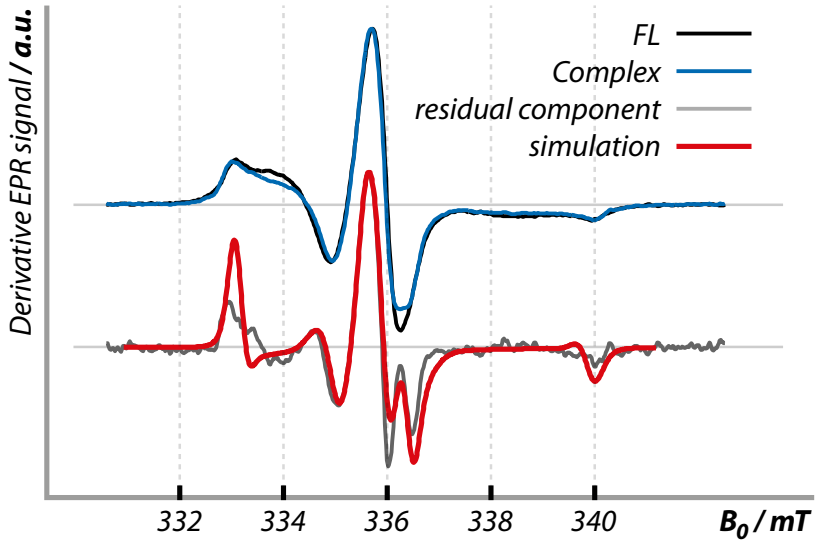

Figure 5.18: *Ambient temperature cwEPR of DnaJ$_{full\,length}$ I50C/V90C alone and in complex. Both samples show strong anisotropic and slow tumbling, even more so in the complex spectrum. With singular value decomposition, it was possible to extract and simulate the difference near the rigid limit with $\tau_c \approx 100\,ns$.*

The Complex sample also has been measured at room temperature and generally agrees to the spectrum of DnaJ$_{full\,length}$ I50C/V90C. A detailed comparison via singular value decomposition, however, yields an additional component in the rigid limit of about 25% (figure 5.18). This is an indication of one or both residue positions to have rotamer exchange between a rigid conformation and their remaining orientations, requiring the complex interface region being located in the J/GF-region. It is also in agreement with the one-component peak result from the short ELDOR traces to have both J/GF-regions interfaced.

5.3 Synopsis

In this chapter we have presented the experiments on spin labeled *T. thermophilus* DnaJ, which in conclusion support the crystal structure for the J- and GF-domains being relevant in solution. No indications have been found for major unfolding of the GF-domain as it is reported from other organisms like *E. coli*. The experiments document a much closer intra-dimeric distance between the majority of both J/GF-sections, suggesting a more consolidated quaternary conformation in solution instead of the V-shape seen in the crystal structure.

The DnaJ•DnaK•DafA storage complex completely conserves the monomeric J/GF conformation of the crystal structure and DnaJ$_{full\,length}$ in solution. The addition of DafA and DnaK inhibits the motion of the attached spin labels, which implicates the J/GF-region in the substrate binding.

The complex sample furthermore retains the overall modulation depth as well as the proportion of its intra-monomeric contribution, being solely of intra-dimeric origin in DnaJ$_{full\,length}$. This in turn is solid proof against a *trimeric* storage complex stoichiometry, as found in the literature [5], but suggests an even ratio DnaJ$_{2n}$•DnaK$_{2n}$•DafA$_{2n}$.

Regarding the quaternary structure of DnaJ$_{full\,length}$ in complex, it is similar to that observed in DnaJ$_{full\,length}$, although with more contributions at smaller distances resulting in a slightly broader distribution. This is a strong indication of the DnaJ–DafA interaction not to be based on rigid polar bonds, but on amorphous hydrophobic interaction. Still, it is not connected to any unfolding of the J/GF-section between I50 and V90 as formerly presumed, but has to originate from positions further upwards in direction of the C-terminus.

The DnaJ$_{\Delta 108-114}$ construct, used for crystallization, showed a quaternary structure in solution most deviant from its own structural conformation. Presumably, the crystallization selected the V-shape conformation due to optimized packing, while in bulk solution the deletion of the linker molecules could have allowed for an optimized J/GF–J/GF orientation with tight hydrophobic interaction.

Finally, the possibility of crosslinking is evident from the ELDOR distance distributions and the model simulations (with intra-dimeric distances reaching into the area of possible linking). However, no particular contortion or disproportionate exposition of the structure surrounding S86C could be observed, as presumed by the increased yield from S86C-crosslinking. Exaggeration by shifts in equilibrium between the conformations is possible and would be in line with the results presented here.

Chapter 6

BlrB

The research on *R. sphaeroides* BlrB as an isolated BLUF protein presented in this chapter is aimed at the identification of a valid solution structure for its C-terminal tail region in the dark state ($BlrB_{dark}$). This goal is strongly motivated by a second crystal structure for the W92N-mutant of the protein in dark state[I] showing a fundamentally different conformation of this region as in the available wildtype (WT) structure 2BYC[4] (displayed below in figure 6.1).

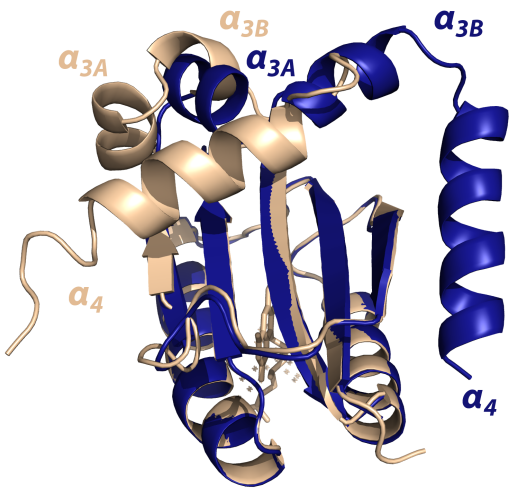

Figure 6.1: *Crystal structures of* R. sphaeroides *BlrB WT (*2BYC*, wheat) and W92N (blue).*

[I]Private communication by Thomas Barends, Ilme Schlichting and Elisabeth Hartmann, MPIMF Heidelberg

Furthermore, it has the purpose of detecting conformational changes of this region upon blue–light illumination (creating BlrB$_{light}$). The experimental observations are related to available literature data for possible mechanisms of signal transduction at the end of the chapter.

6.1 BlrB dark state

ELDOR on BlrB$_{dark}$

The C-terminal tail region is divided into three helical regions α_{3A}, α_{3B} and α_4. To accumulate enough information on the solution conformation of the C-terminal tail, eight different pairs as well as two single mutants have been constructed. Two double mutants with a label in α_4 have additionally been examined in BlrB W92N to shed light on the W92 in–out issue.

As described in the methods chapter in section 4.3, two labels have been placed within α_{3A} in conjunction with the body region anchor Q74C, Q74C/-K100C and Q74C/A104C. Another two samples, Q74C/S115C and Q74C/E118C, have labels at the end of α_{3B} and the beginning of α_4, respectively. S58 is situated in the first turn of α_2, pointing away from the beta sheet and acts as a second anchor in the protein body. It was combined with R95C at the end of β_5 as well as with A129C at the tip of helix α_4. The latter position is monitored from another angle by the E110C/A129C mutant. Both A129C double mutants are additionally examined in conjunction with the W92N tryptophan replacement. Finally, the V31C/S98C double mutant is created to observe the transition region from β_5 to α_{3A} from another direction.

Figures 6.2 and 6.3 show the results of frozen solution ELDOR measurements on the BlrB$_{dark}$ double mutants in comparison to rotamer predictions from both crystal structures. The ELDOR traces have been background corrected, and the resulting dipolar evolution functions $D(t)$ were simulated using Tikhonov regularization with a broadening parameter of $\alpha = 10$ (see chapter 4 for a detailed description).

The different crystal conformations of the C-terminal tail region is reflected in their divergent rotamer calculations. Neither structure is suitable to explain

all measurements, but nonetheless both contain useful information.

For the first label pair Q74C/K100C between body (Q74C) and helical tail (K100C in α_{3A}), the experimental trace shown inset in figure 6.2 features a defined oscillation over two fully visible periods. Still, several frequencies are present as the modulation strongly deviates from a harmonic shape. The simulated distance distribution with its mean at 2.85 nm (width 2.1 nm) features a bimodal peak of major intensity with a sharp cutoff to larger r and a smaller, broad peak. The width is 2.2 nm at the bottom. As K100 is located at the beginning of α_{3A}, where both structures still roughly resemble each other, it is not surprising that both crystal structures result in similar distance distributions. They are in good agreement with this distance measurement regarding both width of the distribution and absolute distance, the W92N-structure fits slightly better.

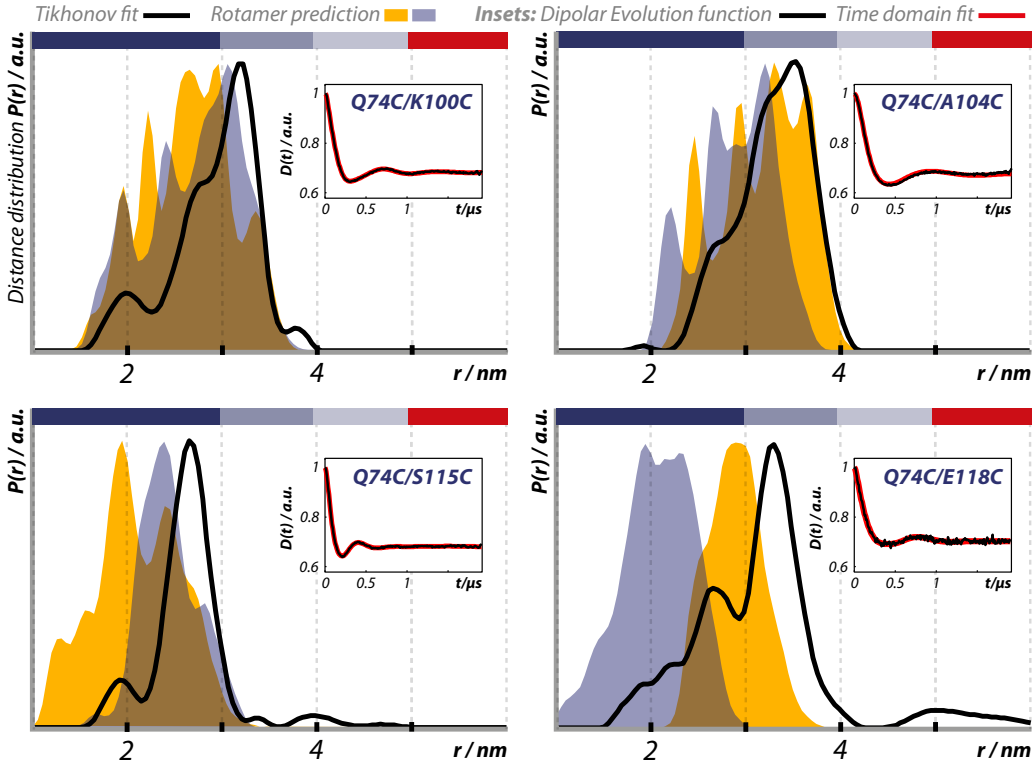

Figure 6.2: *Distance distributions from ELDOR measurements for BlrB$_{dark}$. Inset the dipolar evolution function with its Tikhonov fit. In yellow, the rotamer calculations for the WT structure and in blue for W92N.*

The modulation of the Q74C/A104C time trace is also well pronounced but with a slower, more harmonic oscillation. The corresponding distance distribution thus has its mean at 3.2 nm (width 1.6 nm) and is well matched by the WT rotamer prediction, while the W92N structure produces distances which are too small, even if the shape is in agreement. A104 is at the end of helix α_{3A}, three residues before the enforced break by P107. In the W92N structure, α_{3A} lies slanted above β_2, while it is perpendicular to the beta sheet in the wildtype crystal conformation.

Q74C/S115C is a special case, which we already discussed in a qualitative manner in section 4.4. Its time trace has a clear, short oscillation which translates into a sharp peak at 2.7 nm with a width of about 0.8 nm. A stray small contribution is visible at 2.0 nm. The constituent spectrum of Q74C has to be very narrow in the direction of S115C, even though its rotamers are spread. Both crystal structures do not describe this observation. The region between P107 and S115 forms a two–turn helix α_{3B} in the W92N structure, while it is partly distorted in the wildtype by tension from polar interaction (It will still be called α_{3B} for simplicity).

P117 marks the beginning of the last C-terminal helix α_4 with four turns. Q74C/E118C, even if it is near to S115, shows the most broad $P(r)$ distribution of all measurements. It is centered around 2.8 nm (width 2.4 nm) and similar in overall shape to Q74C/K100C with its major intensity at large distances, although its high distance–flank is not as sharp and the two main distance contributions are separated.

All four Q74C mutants from figure 6.2 possess the same modulation depth: Hence, their labeling efficiency is equal and S115C must be similarly accessible as the other three tail positions.

In figure 6.3, the measurements for the six remaining samples with four different label pairs are depicted. The two samples containing the W92N replacement are offset for clarity (Depicted in blue. For comparison, the WT-based distribution is repeated in gray). The modulation depth of the wildtype based mutants is indicated.

The mutants S58C/A129C and S58C/A129C/W92N possess a main contribution at equal position (3.7 nm) and width (1.4 nm), although the rotameric dis-

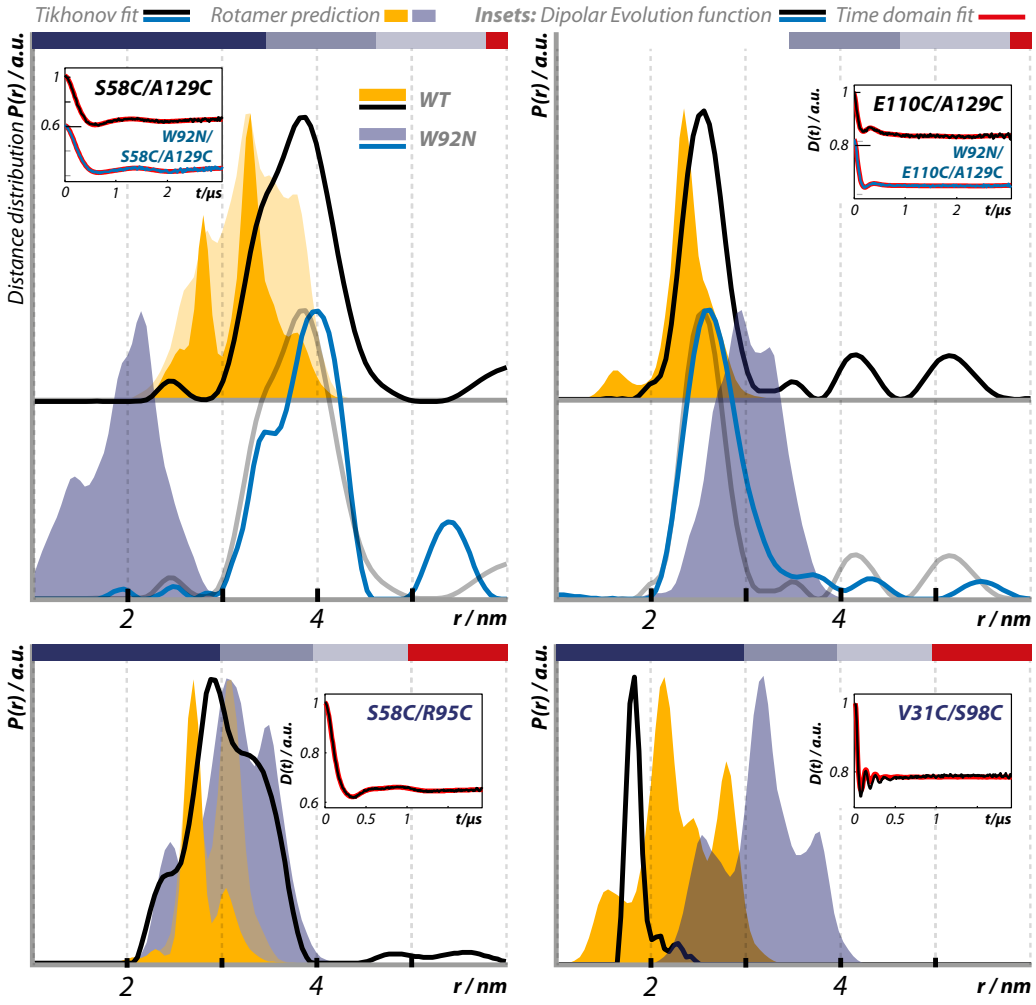

Figure 6.3: *Distance distributions from ELDOR measurements for BlrB$_{dark}$. Inset the dipolar evolution function with its Tikhonov fit. In yellow, the rotamer calculations for the WT structure (with truncated N-terminus in shaded yellow, see section 6.1) and in blue for W92N. The W92N label pairs are displayed in cyan with a comparison to WT from above in gray.*

tribution is slightly shifted to larger interspin distances r in W92N. No fundamental conformational difference between both proteins could be detected. The BlrB$_{dark}$ solution measurement clearly favors the orientation of α_4 seen in the wildtype structure over the W92N crystal structure conformation, although the spins are even further apart in the experiment.

The E110C/A129C double mutant possesses a narrow distribution at 2.6 nm of similar width as Q74C/S115C. However, it has a significantly reduced modulation depth Δ, indicating reduced labeling efficiency and thus reduced accessibility of E110C within helix α_{3B} (S58C/A129C had no unusual Δ).

In E110C/A129C/W92N the overall distance distributions is identical. The modulation depth is higher (which will be discussed later in combination with the BlrB$_{light}$ results) and the right flank of the distance peak is marginally spread out by 0.2 nm. As this label pair monitors the C-terminal conformation from within and is independent from the relative position of the protein body, both structures can produce similar rotamer predictions. The relative orientation between E110C in α_{3B} and A129C in α_4 in solution probably conserves the wedge shape seen in the crystal structures with a wider angle as in the WT and a smaller as in the W92N structure.

The distance distribution of S58C/R95C forms a bell shaped curve similar to that of S58C/A129C, but centered at 3.0 nm (width 1.8 nm). It will be discussed in the following section in detail.

The last sample, V31C/S98C, exhibits an oscillation of short time period which is extremely defined. This is completely atypical for a soluble protein with attached spin labels. Its needle–like distance requires *both* MTSL labels to be immobilized. The lower modulation depth is an additional indication of reduced accessibility (seen only here and in E110C/A129C). The label at S98C probably is stuck to a hydrophobic region in the vicinity (there are plenty of apolar residues above and below the beta sheet at this position) and is constrained in its motion in this manner. In the neighborhood of V31, however, there are mainly arginines and other polar residues. The only nearby apolar residue L34 cannot explain the constriction of the rotamer configuration at V31C necessary for the appearance of one single interspin distance. The two mutations V31C and S98C do not contort the backbone structure at the cofactor (which would be an alternative explanation), as it is still capable to undergo the same reversible

light activation reaction as the other samples[II]. Given the strong interference of unassigned residues from the surrounding, anyhow no reliable information about the backbone conformation can be gained from this double mutant.

Both the WT and W92N based double mutants show virtually identical distance distributions in frozen solution. Therefore, both X-ray crystal structures originate from the same solution conformation of $BlrB_{dark}$. The measurements in general document a difference between this solution conformation and both crystal structures, but the reason for the different orientations of the C-terminal tail in the crystals is not yet found.

Position of the β_5-strand

The measured S58C/R95C distance distribution is nearly identical to the prediction from the W92N structure, while the WT-structure distances are both too small and too narrow. Taking a look at the surrounding of R95 in both structures (see figure 6.5), we realize that the β_5 strand in the W92N sample has moved by two amino acid positions in relation to the wildtype as the *asparagine*92 has moved into the binding pocket (in the literature designated as the 'Trp–in' position). In addition, α_4 is not situated above R95 in the W92N structure, but on the other side of the protein along α_2. The surrounding of the anchor S58 itself might be influenced by the fixed position of the N-terminal amino acids M1 and D2 in its vicinity in the WT structure, which have no localized density in the W92N structure.

To separate these effects, it is most feasible first to check the influence of the WT tail position on the variety of rotamers by artificially cutting away helix α_4 (*'no Tail'*). As it can be seen in figure 6.4, the change in rotamer configuration is negligible. The simulated label at S58C, on the other hand, was indeed limited to a subset on conformations. Larger contributions emerge at above 3 nm upon truncation of the N-terminus by two residues (*'no Nterm, no Tail'*). Hence, figure 6.3 was appended with the modified rotamer calculations for S58C/A129C, too. Regarding the width of the calculations with and without truncated N-terminus in figure 6.3, a lack of conformational stability of M1 and D2 (therefore not

[II]Private communication of UV/vis data by Anikó Udvarhelyi, MPIMF Heidelberg

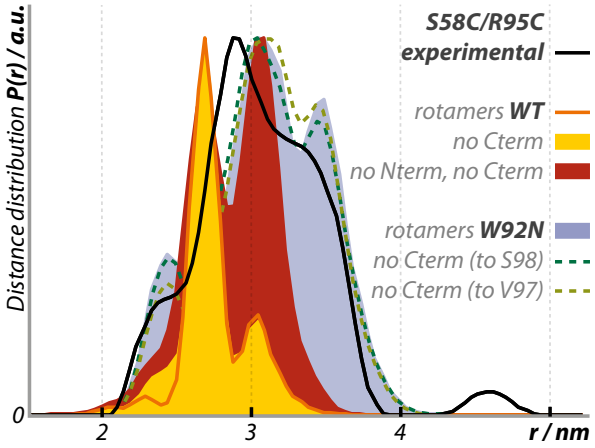

Figure 6.4: *Distribution function of* S58C/R95C *in comparison with rotamer simulations of different structural environments at position* R95.

limiting the rotameric configuration of S58C) in frozen solution is probable. Still, the distribution calculated from the twice modified WT structure (filled red) has its peaks where the measurement exhibits relative minima, thus is not a good model for the β_5 solution conformation of BlrB_{dark}.

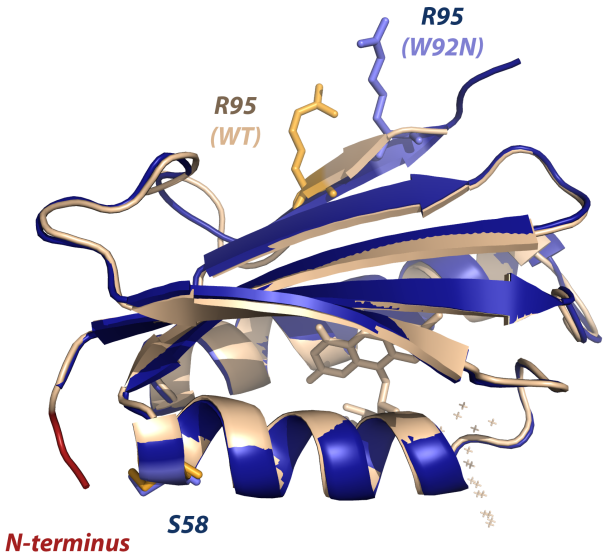

Figure 6.5: *Position of* R95 *from both the WT and W92N structures.*

Removing the C-terminus from the W92N mutant structure even down to

the R95 neighborhood has no fundamental effect on the calculated rotamer distribution of S58C/R95C (*'to S98'* and *'to V97'* in figure 6.4). This indicates the S58C/R95C-measurement carrying no strong information about the orientation of either helix α_{3A} or α_4, but clearly evidences the β_5 position of the W92N structure as its conformation in BlrB_{dark}[III]. This poses the question about the location of *tryptophan*92 and also whether it is flipped into the flavin cavity or situated outside. We will return to said question in a later section.

Position of S115 in BlrB_{dark}

One extremely important clue is the ELDOR result of Q74C/S115C. Even though the rotamers of Q74C are very widespread, S115C is located in a position, where a) it has few rotamers and b) these are perpendicular to the plane of largest density of all Q74C-rotamers. For the given distance of 2.7 nm and these geometric arguments, only a small range of locations for the center of the S115C-rotamers is possible, as discussed in depth in section 4.4.

To find this area, a Monte Carlo search[IV] for putative alternative orientations of helices α_{3A}, α_{3B} and α_4 was performed as described in section 4.2. Their initial geometry was taken from the W92N structure, as it provides an entirely helical α_{3B} that can serve as a first model for the steric limits of the S115C position and the α_4 orientation. Furthermore, the rotamers calculated from the W92N structure (which were fixed for the Monte Carlo search) better match the *shape* of the observed distance distributions than those from the WT structure. In each step, two randomly determined $N - C_\alpha$ bonds of S98 and R99 between α_{3A} and β_5, L105 and A106 between α_{3A} and α_{3B}, and L114, G116 between α_{3B} and α_4 were rotated. Afterwards the resulting distance distributions were compared with the measurements with a strong weight on the Q74C/S115C and

[III] This perfect match of the distance distribution could otherwise mathematically only be achieved on the surface section of a sphere centered around S58 with near identical rotameric arrangement relative to this residue, but given the interaction with the beta sheet – imposing a preferred direction and integer positioning – and the actual observation of this conformation in the W92N X-ray structure, an alternative is highly unlikely.

[IV] The program originally developed by Thomas Barends for the qualitative DnaJ conformation search was substantially modified in this work to support multiple weighed distributions of the actual MTSL side chain as a more realistic model with improved precision.

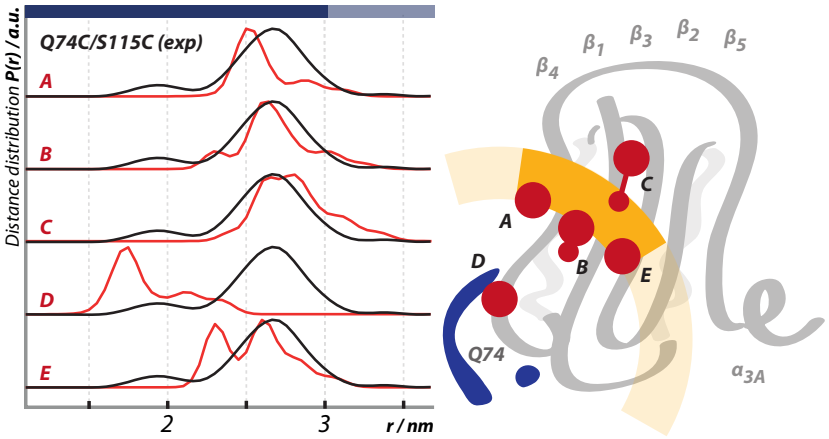

Figure 6.6: *(left) Exemplary rotamer distributions of artificially created S115C positions. (right) Location sketch of the beta sheet (gray), viewed from the C-terminal side without α_{3B} and α_4. The rotamer positions of the left simulations are indicated in red. In each case, the amino acid 115 was located 0.6 to 0.75 nm above the beta sheet ($C_\alpha - C_\alpha$–distance). The S115C rotamers from the measured sample must be located within the yellow area.*

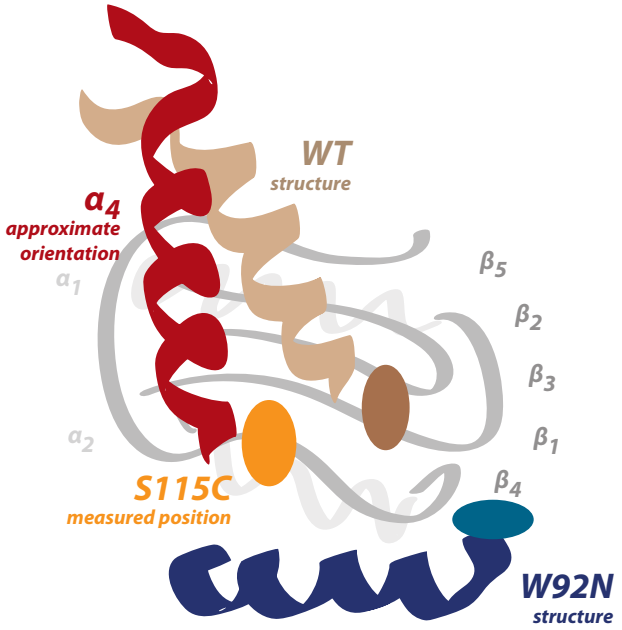

Figure 6.7: *Sketch of the protein, again viewed from the C-terminal side with the beta sheet and α_1, α_2 below in gray. The round areas mark the position of S115 as seen in both crystal structures and in the measurement. Combined with an estimate for the E110C/A129C criterion, the orientation of α_4 has to be more perpendicular to the beta strands than seen in the WT. α_{3A} and α_{3B} are omitted.*

E110C/A129C constraints. Overall improved structures were saved and could later be selected from a graph documenting the each ELDOR distance criterion. For promising conformations, the joints have then been minimized using the Amber forcefield (method described in section 4.2) and the rotamers have been newly calculated. Figure 6.6 displays several optimal results for S115 in close proximity to the beta sheet (0.6 to 0.75 nm $C_\alpha - C_\alpha$–distance) as well as an exemplary outlier in the vicinity of the S115 position seen in the WT crystal structure.

In comparison to both crystal structures, S115 is situated more centrally above β_1 or β_4. This has steric consequences for α_4 (in combination with the E110C/A129C constraint), pushing it further back (see qualitative sketch in figure 6.7). This protrusion of α_4 may prevent tightest packing for crystallization in the solution conformation and cause the discrepancy in its orientation as well as the decomposition of α_{3B}.

Model structures from the BlrB$_{dark}$ ELDOR data

The broad distributions of Q74C/K100C and Q74C/A104C makes automated unambiguous fitting nearby impossible, as simple statistical values like χ^2 or correlation between test conformation and measurement can be equally achieved by very different orientations[V]. Figure 6.8 shows three optimized results from different Monte Carlo search runs (in parts with more flexibility) with near identical S115 position. They all fulfill the ELDOR constraints much better than both crystal structures, but still the orientation of helix α_4 exhibits a wide variety for this specific S115 position (if located on the diagram 6.6, it would be in the center between B, C and E). The comparison to SAXS measurements[VI], as explained in section 4.2, indicated that more information is necessary to better fix the separate structural elements. An optimal overlap could not be found by the automated search (The parameter space is still too large).

An extreme example, borderline compatible with the ELDOR constraints, is displayed in figure 6.9. Helix α_{3B} has been attached to the beta sheet and α_4

[V] An instructive example of the ease of misguiding graph fitting is provided by Anscombe's quartet [126].

[VI] Private communication by Anikó Udvarhelyi, MPIMF Heidelberg

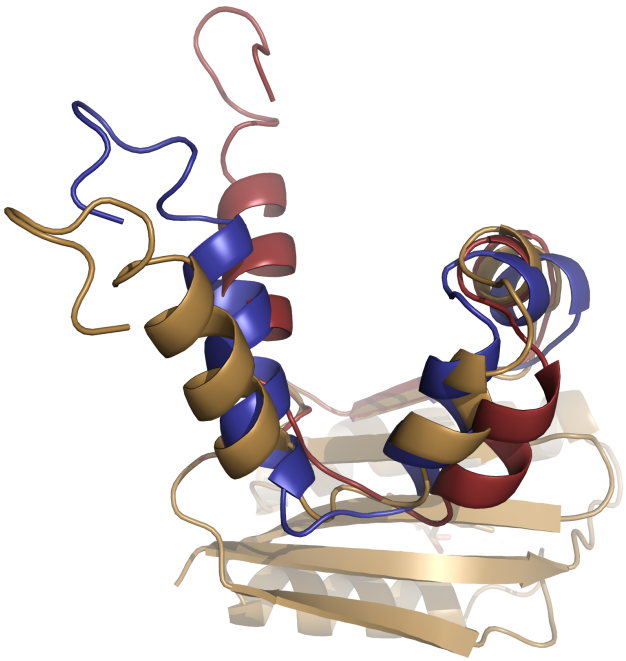

Figure 6.8: *Three different model structures acquired by hand-adjusting optimal fits from different Monte Carlo search runs with near identical S115 position, minimized with Amber.*

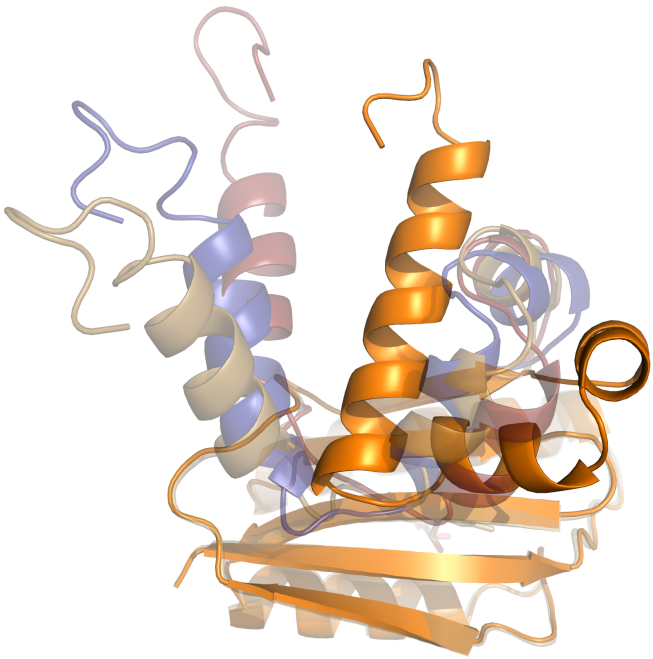

Figure 6.9: *Another model structure still borderline compatible with the ELDOR measurements. It has a substantially different α_{3A} and α_{3B} conformation. Helix α_4 follows accordingly to fulfill the E110C/A129C and S58C/A129C constraints.*

follows, but even in this example, there is no knowledge about the lengthwise rotation of α_{3B}, which affects the E110C/A129C distance distribution greatly. In conclusion, the BlrB$_{dark}$ spectra form an elastic network of constraints that is still lacking substantial evidence of how it could be placed inside the protein framework. A reliable reconstruction of the relative orientations must rely on additional information like ELDOR on illuminated BlrB$_{light}$.

6.2 BlrB light state

ELDOR on BlrB$_{light}$

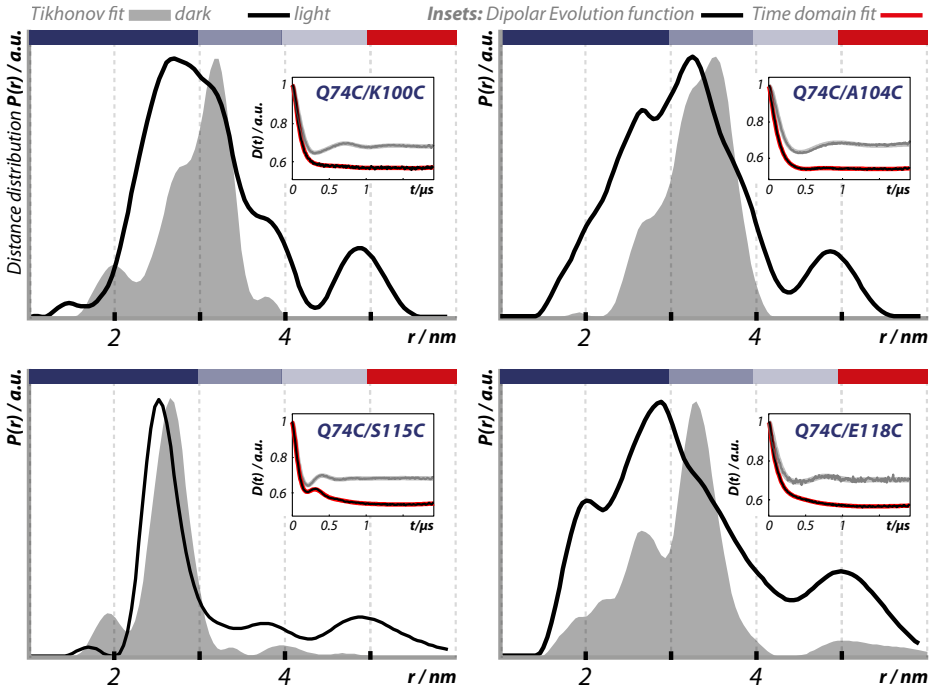

Figure 6.10: *Distance distributions from pulsed ELDOR for BlrB$_{light}$ as black lines, BlrB$_{dark}$ for comparison in shaded gray. Inset the dipolar evolution functions with corresponding Tikhonov fit.*

Figure 6.10 depicts the ELDOR measurements of all four Q74C/X double mutants of BlrB$_{light}$, normalized by their maximum peak intensity[VII]. They all ex-

[VII]For the Q74C/X samples, this normalization is an opportune depiction. See later in this

hibit the same significant increase in modulation depth (Table 1 in the supplement lists numerical values) which can only be explained by inter-monomeric interactions, thus formation of a dimer or multimer upon light activation.

Furthermore, in all cases except Q74C/S115C, the distinct modulation is lost to a broad, nearly uniform time trace decay. In Q74C/S115C, however, the additional signal is limited to larger r, while the monomeric peak is nearly not affected. A slight shift to smaller distances can be observed, but its width and shape stays the same. In combination with the indication of reduced accessibility of E110 in α_{3B} from the measurement of E110C/A129C, which possesses significantly reduced modulation depth in BlrB$_{dark}$, it is plausible to attribute this stability of the S115C position to a strong interaction between helix α_{3B} and the beta sheet.

For the three broad distributions of Q74C/K100C, Q74C/A104C and Q74C/E118C, following properties can be recognized: a) The substantial amount of distance contributions at larger r in BlrB$_{dark}$ (the sawtooth shape) changes into a bell shaped distribution plus contributions at higher distances. b) For Q74C/K100C, the defined substructure is completely lost and the integral center of the first large contribution is significantly shifted to lower r, but remains within its original bounds. c) In Q74C/A104C, the shift of the center is accompanied by an extension down to the boundaries of reliable distance determination by ELDOR at 1.5 nm. d) In Q74C/A104C as well as in Q74C/E118C, there is substructure preserved. e) Q74C/E118C shows the most drastic difference between its very pronounced peak in its dark state at 3.2 nm and the absolute maximum of the massive light state distribution at 2.9 nm.

The obvious multi component–nature of these three Q74C/X BlrB$_{light}$ distance distributions makes it necessary to identify the proportions of the constituents. In the case of a dimer (which is observed, see below Q74C single mutant in BlrB$_{light}$), the mean increase of the modulation depth Δ from $\Delta_{dark} = 0.32$ to $\Delta_{light} = 0.45$ can be understood in relation to optimized experimental values[VIII] for spin pairs ($\Delta = 0.5$, 0% dimer), triples ($\Delta = 0.7$, 50% dimer is

section for a detailed discussion about normalization.

[VIII] Bode et al. have found these values in 2007 [95] for highly diluted, pure n–spin organic molecules with an optimized excitation efficiency λ and have used a theoretical model on the basis of Milov et al. [88,94,104] and the background interaction from Mims 1972 [102].

formed and resolved, this leads to one additional interacting spin on average), and quartets ($\Delta = 0.8$, 100% dimer is formed and resolved)[95]. By projection onto this scale, $\Delta_{light} \rightarrow 0.7$, which implies a dimerization rate of about 50% for fully visible dimerization effects in the time trace and otherwise an even higher percentage. Extrapolating the dimensions of the dimer from the size of one BlrB monomer, most interactions will be within resolution or at least will affect the modulation depth of the time trace at its end ($t = \tau_2$).

Dimerization of a labeled double mutant causes three distinct additional distance contributions from intra-dimeric interaction. For a proportion of 50% observed dimer interaction in the time trace, they amount to a total intensity of 1/6 for the cross distance and 1/12 each from the mutual intra-dimeric interactions. To complicate matters, BlrB has one of the fastest back reaction time constants of all BLUF domains of only several seconds. Even with shockfreezing under light, the equilibrium will be in between the dark and light states, hence further small contributions from remaining BlrB_{dark} will be found in the spectra.

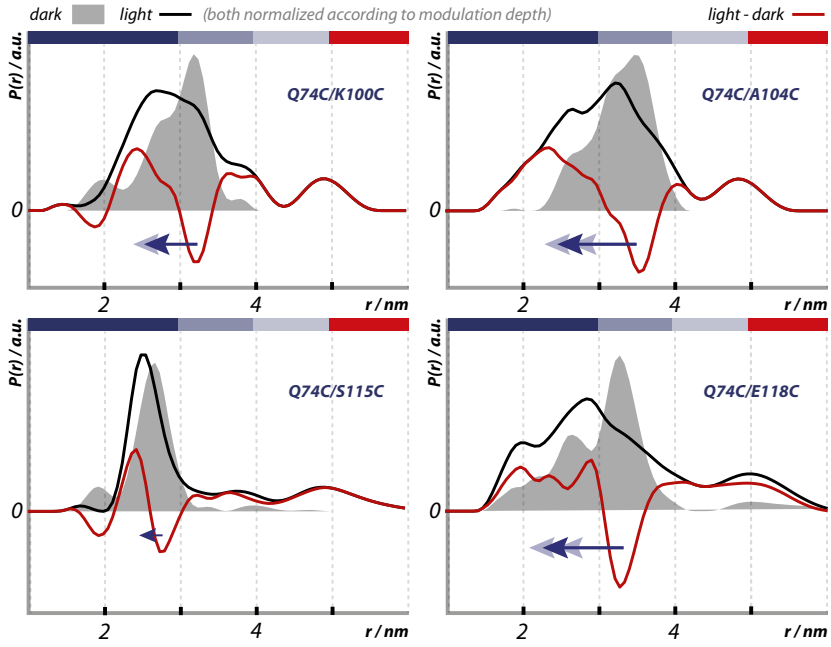

Figure 6.11: *Difference (red) between light and dark spectra. Integrals normalized to 1 for light and 0.67 for dark (with approximately 50% dimer, see text). The blue arrows indicate the change of maximum intensity, thus is an estimate for the conformational change.*

While for Q74C/S115C, the slight shift to lower distances is evident, the extent of any possible conformational shift at the three positions K100C, A104C and E118C remains unclear. With a hypothesis of no conformational change and the intra-dimeric interactions solely causing the additional broadening as well as the shift of the mean to significantly lower distances, the light and dark distributions were compared after integral normalization to their appropriate intensities most consistent with the observed modulation depths changes (50% increase in $\Delta \Rightarrow$ normalization to 1 for BlrB_{light} and 0.67 for BlrB_{dark}). The result in figure 6.11 clearly shows the nontruth of the constant conformation–assumption, as negative distance contributions are physically impossible. This result is also not dependent on the chosen basis for normalization, because even with normalization on the basis of a doubled modulation depth (which corresponds to 100% dimerization, 100% labeling efficiency and no remains of BlrB_{dark}) a negative intensity of 1/4 the peak positive would occur in Q74C/K100C, which shows the smallest shift. Therefore, substantial conformational changes take place at all three positions, which push significant parts of the intra-monomeric interaction into lower distance regions.

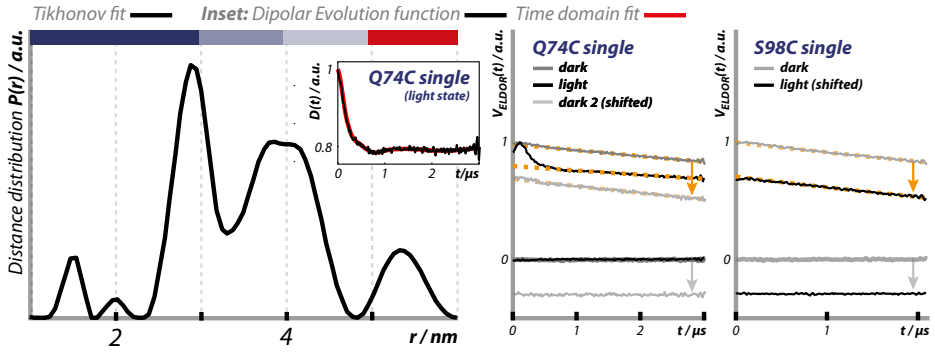

Figure 6.12: *The Q74C single mutant forms a defined dimer upon light activation (distance distribution to the left), which is reversible (center), while the S98C single mutation shows no conformational change. Also note the shift in the background slope of Q74C, as the effective concentration of spin particles is reduced.*

To have an estimate for the inter-monomeric contributions, the Q74C single mutant has been measured in the dark and illuminated state (figure 6.12). As expected, Q74C shows no modulation in the dark, but a defined ELDOR modu-

lation manifests upon light activation which can only originate from a specific, well defined dimer conformation and not a multimer. It provides us with one determined constituent for the light spectra, which mainly contributes to the higher distance flanks (and also would further amplify the negative values from figure 6.11). One can argue, that probably the intra-dimeric Q74C/X cross distances won't be smaller than the monomeric Q74C/X contributions, leaving only the X–X mutual interaction in the lowest distance region with an small intensity of about 8%. This allows the interpretation of the observed changes in the distributions on the lower flanks to mainly be attributed to the intra-monomeric interactions even on a semi-quantitative level.

Again regarding figure 6.11, the strongest change in its distribution shape is observed in Q74C/E118C . Together with the nearly conserved position of S115C, this implies a turn or a lengthwise rotation of helix α_4, but no large translation of the residues at its base[IX]. For Q74C/K100C, a similar tendency can be found. However, the rotamers of A104C on the same helix significantly reduce their minimal distance to Q74C by nearly 1 nm. This is a major reorientation, given the propagation of one helix turn is only 0.54 nm. As the overall distance between Q74C and K100C remains the same and the position of S115C is also fixed (an with it at least parts of α_{3B}), A104C from α_{3A} can only slide down to the front edge of the beta sheet. This would involve a longitudinal rotation of α_{3A} which also reorients the rotamers of K100C with respect to Q74C. This change also is in line with the increase in R_g observed upon illumination in the SAXS experiments – the protein changes from a globular to a more flat conformation.

To find clues about the mechanism causing this conformational change, which cannot be initialized by the relatively fixed α_{3B}, we have to discuss the light state ELDOR measurements of the remaining mutants (figure 6.13).

Orientation of α_4 and β_5 in BlrB$_{light}$

The light state of all WT based double mutants in figure 6.13 (again normalized to maximal peak intensity) show a similar increase of their modulation depth as those with the Q74C anchor. The S58C/A129C time trace of the illuminated

[IX]Helix α_4 starts at P117 with a flexible G116 connection to S115 and the rather fixed region of α_{3B}.

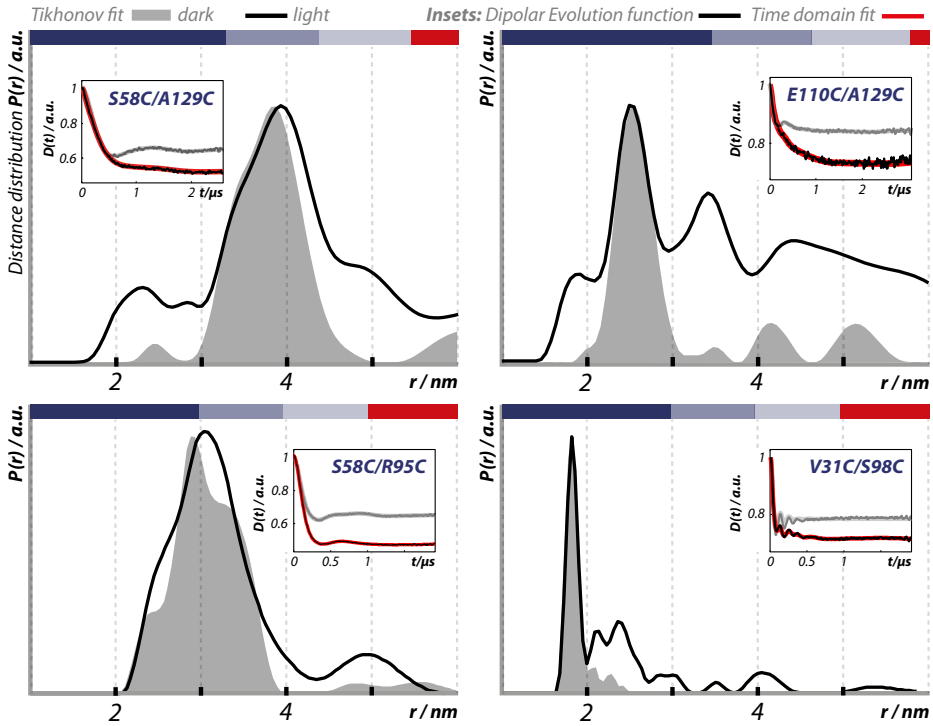

Figure 6.13: *Distance distributions from pulsed ELDOR for $BlrB_{light}$ as black lines, $BlrB_{dark}$ for comparison in shaded gray. Inset the dipolar evolution functions with corresponding Tikhonov fit.*

state still retains the characteristics of its main bend, the distance distribution therefore shows the same predominant contribution as in $BlrB_{dark}$. In addition, a contribution between 2 and 3 nm emerges as well as a broad shoulder above 4.5 nm, tailing out beyond the resolution of the time trace.

As the shape of the S58C/A129C$_{dark}$ distribution is nearly bell shaped, one can attempt an estimation of the other interspin interactions by similar curves (figure 6.14). The observed light spectrum possesses three additional regions, which can be approximated by integral normalized Gaussian functions. The central new peak is larger by a factor of two, and thus potentially marks the cross interaction between S58C and A129C from different monomers. Subtracting these Gaussians from the observed light peak returns the shape of the dark spectrum as the remaining intra-monomeric distance between S58C and A129C in the light state, which documents the consistency of this model. It restricts

the possible movement of A129 to a sector on a spherical surface around S58C (see section 4.4). Consequently, one of the two single intensity peaks is caused by the mutual A129C interaction, the other by S58C. We now can look at both S58C/R95C$_{light}$ and E110C/A129C$_{light}$ to find a similar shoulder down to below 2 nm only in E110C/A129C$_{light}$, determining the lowest emerging peak as the A129C–A129C distance. It places both S58C rotamer configurations further than 5 nm apart from each other. Together with the distance between both Q74C positions in BlrB$_{light}$, this implies the C-terminal side of the β sheet as interface region for the light induced dimer.

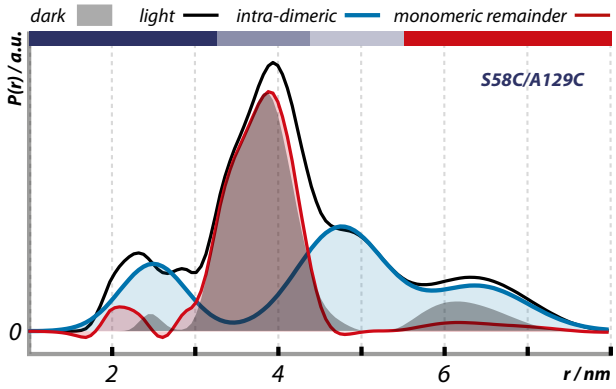

Figure 6.14: *Approximate fitting of the three different intra-dimeric interactions of S58C/A129C$_{light}$ with normalized gaussian functions of appropriate width. They are centered at 2.5 and 6.4 nm for the A–A and B–B interactions and at 4.75 nm for the cross distance of double intensity. The remainder (red, shaded) reproduces the monomeric dark spectrum (gray, shaded).*

For the analysis of E110C/A129C, the otherwise opportune normalization to maximum peak intensity is misleading in this case, because in BlrB$_{light}$ contributions over the whole observed distance range emerge. The BlrB$_{dark}$ distribution, however, consists of one single, narrow peak. The integral normalization in figure 6.15 provides a more accurate proportion. From this figure it is clear that the peak intensity of the BlrB$_{dark}$ peak at 2.6 nm decreases substantially. This is a direct consequence of the observed (and limited) increase in modulation depth and is independent from a specific model of excitation and dimerization efficiency. It is, however possible to acquire estimates for these parameters by comparison

to S58C/A129C. Superimposing the found A129–A129 interaction as a Gaussian centered at 2.5 nm, the remaining intensity at this distance is a mere leftover of its former amplitude. The aforementioned circumstance of persistent fractions of non-excited BlrB$_{dark}$ in the illuminated sample explains this remainder, which amounts to a semiquantitative maximum estimate of 15% BlrB$_{dark}$ (as shown in said figure 6.15).

For S58C/A129C, the observation of a constant intra-monomeric distance between S58C and A129C is not influenced by this equilibrium in the illuminated sample, as the dark spectrum has been reproduced by the analysis (It would only increase the relative dimerization rate of the BlrB$_{light}$ fraction). For the Q74C/X samples, any remainder of BlrB$_{dark}$ would even increase the negative intensity encountered in figure 6.11, and thus increase the extent of their observed conformational shifts.

Returning to the broad distance distribution of E110C/A129C$_{light}$ after having determined the origin of the contributions below 3 nm, it is clear that a conformational shift takes place. For a self consistent interpretation of the results, given the conservation of the rotamer configuration of dark adapted S58C/A129C in its light state, the narrow intra-monomeric distance peak of E110C/A129C$_{dark}$ retains its shape in BlrB$_{light}$ as well. The interaction above 4 nm in E110C/A129C$_{light}$ is broad an not strongly defined, therefore only the newly formed peak at 3.4 nm can be assigned to the intra-monomeric in the illuminated protein, which corresponds to a (directly observed) translation of A129C in the C-terminal part of helix α_4 by 0.9 nm. Due to the conservation of the rotamer orientations of A129C, no lengthwise rotation occurs alongside the relocation of α_4 which is stronger at its C-terminal end than at its N-terminal beginning (see Q74C/E118C and Q74C/S115C). The observation of this major rearrangement is a pivotal result of this work.

The distance distributions of S58C/R95C for BlrB$_{light}$ and BlrB$_{dark}$ have the same width and position of its main contribution. However, their well resolved internal structure is fundamentally different. The main peak has three components in the dark state, but a bimodal shape in the illuminated state with its relative maxima at the position of the local minima in S58C/R95C$_{dark}$. This complete inversion of the substructure takes place without changing the lower boundary

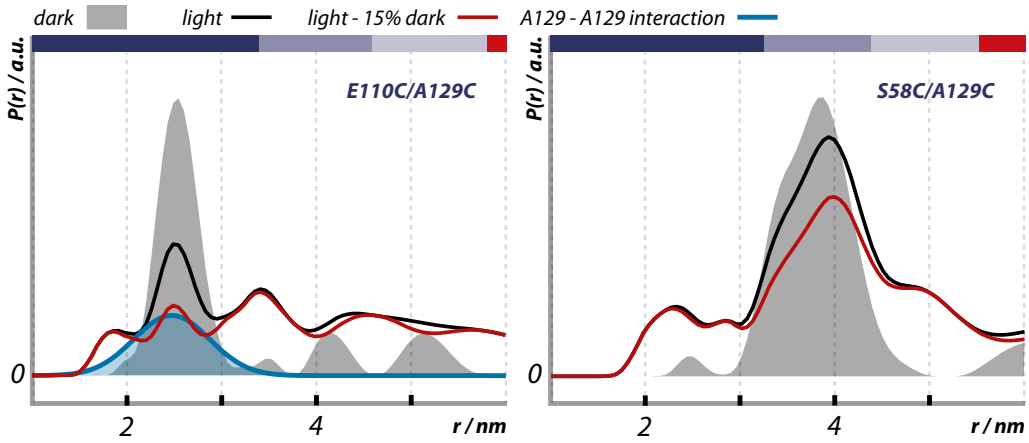

Figure 6.15: *Comparison light vs. dark of E110C/A129C (left) and S58C/A129C (right) with the integrals normalized to 1 (light) and 2/3 (dark) respectively, as estimated from the modulation depths. In red, light minus 15% dark as an approximation of the actual light state spectrum (accounting for a remainder of dark state BlrB).*

of the rotamer distribution . To conserve the dark spectrum as intra-monomeric contribution of the light spectrum, the intra-dimer interactions would have to fill the gaps. This is illustrated in figure 6.16 with a generous assumption of 2/3 dimerization instead of 50% and no upfront correction of the light spectrum for any remains of BlrB_{dark}. The expected amplitude of the dark spectrum is subtracted.

Of the three intra-dimeric interactions, only R95C–R95C and the cross distance can be located below 5 nm (S58C–S58C was already assigned to higher distances and is not fully resolved by the comparatively short time trace of S58C/R95C). The constituent spectra of these two interactions between broad rotamer distributions of S58C and R95C would have to cause three distinct, narrow peaks within 2 to 4 nm, which they can't[X]. Instead, we have to assume broader, bell-shaped intra-dimeric interactions in this region and above, which would make it necessary for the intra-monomeric interaction to shift from a triplet to a bimodal shape and mainly define the observed internal structure of the light spectrum.

[X] Again, any remains of BlrB_{dark} in the light state would increase this trend, pushing the local minima into negative regions.

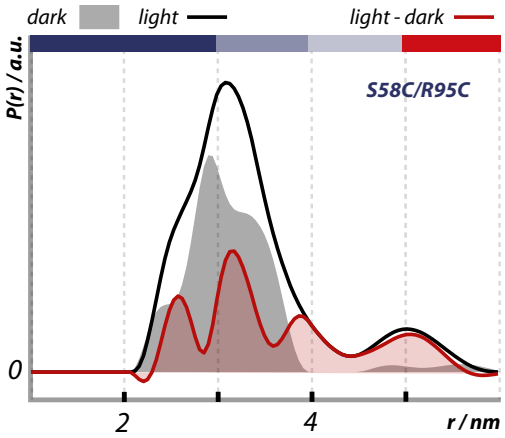

Figure 6.16: *Hypothesis of no conformational change for R95C. Generous estimation of 67% additional intra-dimer signals instead of 50% and no upfront reduction of the light spectrum of any remains of $BlrB_{dark}$. The distance is shown in red and should be constituted only by intra-dimeric interactions.*

Such a bimodal shape at exactly this position we have already found in the 2BYC wildtype crystal structure (after truncation of the N-terminus). Figure 6.17 shows the rotamer simulation for the WT crystal conformation of S58C/R95C

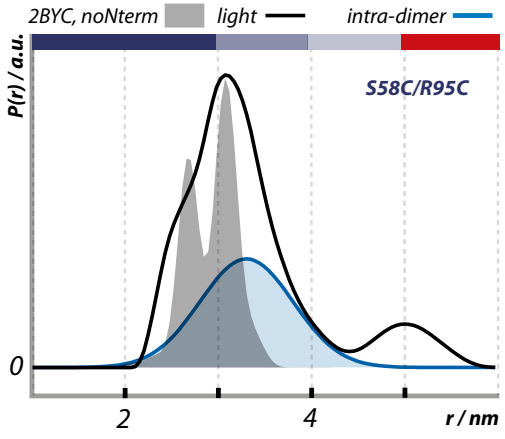

Figure 6.17: *Second hypothesis of conformational change for R95C to the 2BYC crystal conformation. One exemplary intra-dimeric gaussian distribution accounts for the slope on the right edge of the main peak (cyan).*

with truncated N-terminus. The maxima are at the same positions as in the ELDOR data, even if the broadening is substantially different (Proportions of remaining $BlrB_{dark}$ will improve the fit as in the case of E110C/A129C). This represents a conformation distribution centered around the WT crystal position for R95 in $BlrB_{light}$ in contrast to the position from the W92N structure for R95 in $BlrB_{dark}$, and with it for the whole β_5 strand. This change of conformation is again about 1 nm, as directly observed for the tip of α_4 and estimated for α_{3A}.

In other BLUF domains, the presence of *both* conformations of β_5 has been recorded as well[50,55]. In these publications, it was always accompanied by a switch in orientation of tryptophan92, which is not necessarily the case here (see discussion below).

The second monitor for the β_5 conformation, V31C/S98C, does not show any change of its needle-shaped interspin distance. As we have stated above, the labels cling to hydrophobic regions, their $P(r)$ is thus as poorly indicative of the backbone movement as it is of the general backbone structure. However, an increase of modulation depth is recorded, and therefore significant dimer formation. This implies that both labels keep their constrictive environment also after the conformational change.

As a brief summary, the WT based double mutants have shown a directly observable light induced conformational change in α_4 and in β_5 of equal magnitude (1 nm), with α_{3A} similarly influenced. The region of α_{3B}, which has been found in tight interaction with the beta sheet already in $BlrB_{dark}$, remains nearly unaffected. For the orientation of β_5, where the W92N structure had been found to show its dark state conformation, the WT structure 2BYC actually displays a good model for the light state solution conformation of β_5.

The role of Tryptophan92

Tryptophan92 is directly affected by the position of the β_5 strand. The different structure of the W92N mutant posed the question of its effect on the signal transduction mechanism and motivated the creation of appropriate cysteine double mutants which have been examined with ELDOR not only in the dark state (see above, figure 6.3), but also in the light as shown here in figure 6.18.

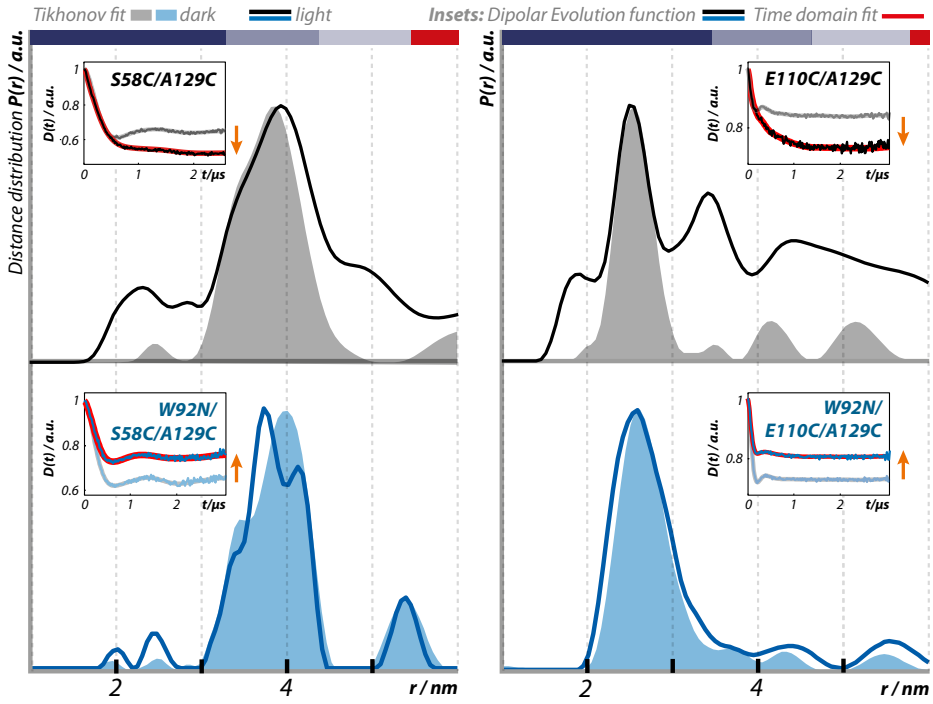

Figure 6.18: *Distance distributions from pulsed ELDOR for $BlrB_{light}$ as black (WT) and blue (W92N) lines, $BlrB_{dark}$ for comparison in shaded gray (WT) and blue (W92N). Inset the dipolar evolution functions with corresponding Tikhonov fit. Note the contrary evolution of the modulation depth Δ (orange arrows).*

In the dark state, S58C/A129C/W92N shows a reproducible, slightly different internal structure of the main peak as the WT based double mutant, and E110C/A129C/W92N a slightly broader interaction, both of which can be explained by a minor change in the rotation angle of α_4. This can be caused by the missing interaction from W92 if this residue would be in outward orientation in $BlrB_{dark}$. However except for this detail, the conservation of the overall distribution also documents W92 and W92N not to have a very strong influence on α_4 directly.

Upon illumination, neither S58C/A129C/W92N nor E110C/A129C/W92N show any signs of conformational shift. In contrast to the WT based double mutants, the positions of the main distance lines stay the same. For E110C/A129C/W92N the peak width is marginally increased and for S58C/A129C/W92N the internal

structure of the main peak changes, but not its width. Furthermore, virtually no dimerization is observed. SAXS measurements on the W92N mutant support this lack of coalescence, the observed radius of gyration R_g is not increased but stays about constant[XI].

Yet in the ELDOR time traces, a drastic change occurs in the modulation depth Δ, which does not increase or remains the same (as no dimer signals emerge, one would expect $\Delta = constant$), but it *decreases* instead. This characteristic can be explained by illumination causing fractions of the sample to lose its structural integrity. In this state, the monomeric interspin interaction of this fraction would be spread statistically over a large distance range. Hence, such a state of reduced cohesion would only affect the background signal in these 3 µs time traces (compared to the long 7.8 µs traces of deuterated DnaJ from the previous chapter, where very loose, longer range interactions could be isolated). This would reduce the observed intensity of defined modulation.

Two BlrB mutants of the W92 residue have been constructed and tested by coworkers on their capability for photoactivation (W92T and W92N). The absorption shift occurred in all UV/vis experiments (measured at 4°C) and the light reaction was reversible, but the red-shifts were 1 to 1.5 nm smaller and the mutant's back reaction speeds were reduced about tenfold[XII].

In comparison to the SAXS results, the extent of the statistical unfolding or random dislocation must be limited, as otherwise an increase in R_g would have been recorded. Because of the capability of the mutants to reversibly undergo photo activation, we can infer the dislocation to be localized in the C-terminal tail region, as it does not affect the UV/vis signals from the binding pocket in a major fashion. In the W92N crystal structure, the seemingly arbitrary new orientation for the tail region could be rendered possible by just the same disconnection thereof.

In summary, the presented W92N experiments prove the *asparagine*92 to destroy the capability of BlrB to undergo light induced conformational change and to slightly change the properties of the binding pocket. Because of the significant and reproducible observed reduction in modulation depth, still a light induced effect is present which must be propagated via a different pathway than

[XI]Private communication by Anikó Udvarhelyi, MPIMF Heidelberg
[XII]Private communication by Anikó Udvarhelyi, MPIMF Heidelberg

by *tryptophan*92. In addition, the BlrB$_{dark}$ spectra of WT and W92N hint at tryptophan92 to be in outward orientation and have weak interaction with α_4 or the C-terminus.

Correlation to literature data

We now have analyzed the experimental information which was acquired within this work. In short, we have found direct evidence for a substantial conformational change of α_4, β_5 and α_{3A} with α_4 and α_{3A} turning away from another in opposite directions (increase in E110C/A129C distance, but decrease in Q74C/A104C), while α_{3B} stays fixed (Q74C/S115C, reduced accessibility of E110). The W92N replacement prevents this conformational change and the subsequent dimer formation, but it has no part in the propagation of the light induced change of the binding pocket (reduction in modulation depth means disconnection of proportions of the C-terminus).

To figure out clues about the actual mechanism of signal transduction, it is mandatory to correlate the experimental results to the information available from the literature.

Wu & Gardner found in 2008 [54] the C-terminus of α_4 crucial for the structural integrity of the binding pocket of BlrB. A truncation from 140 residues down to 135 provided the same UV/vis absorption, but already only 130 amino acids reduced the capability for flavin binding substantially. Truncation to 120 residues (near complete removal of α_4) totally wrecked the integrity of the protein binding pocket, no flavin was bound. In their NMR studies, a reduction to only 135 residues already reduced relative peak intensities signifying decreased conformational stability.

They also published the result from a NOESY NMR experiment[XIII] on tryptophan92, which they found to be water exposed in BlrB$_{dark}$. This indeed fortifies the interpretation of the small effect on the α_4 rotation angle between the

[XIII] NOESY stands for Nuclear Overhauser Effect SpectroscopY. It is another name for relaxation via dipolar interaction between two nuclear spins, similar to ELDOR between two electron spins. It can be used to determine solvent accessibility of amino acids and structural properties of proteins.

$BlrB_{dark}$ ELDOR measurements of WT and W92N based double mutants to signify a weak interaction of W92 with the C-terminus above or at the end of α_4.

Their truncation study showed a graded loss in structural integrity, indicating other amino acids from the C-terminus directly connecting to the main frame of the binding pocket. The extraordinary confinement of the label at V31C could have its origin in the last few residues of the C-terminus (136–140) being attached to a surrounding arginine. Still, further evidence is necessary for this hypothesis.

In order to generally support the discussion about the tail region and to identify, which parts of a BLUF domain are conserved on the side of the beta sheet facing the C-terminus (and averting the cofactor), an alignment of several BLUF domain sequences was performed (figure 6.19). The interpretation founds on the general assumption that conserved residues within cognates will be most important for the protein's functions.

As a general trend for the beta sheet, only polar residues facing the C-terminal side at the beginning and end of a strand are conserved, while apolar conserved chains are found in their center. For simplicity, the highly conserved loop regions between α_2 and β_4, and between β_4 and β_5 are called ζ_1 and ζ_2, respectively.

The first strand β_1, embedded within the beta sheet at second position, possesses a strictly conserved apolar leucine at position 4 below ζ_2 and a long and polar arginine side chain at position 10 in the neighborhood of helix α_{3B}. β_2 and β_3 as the other central beta strands exhibit an even higher level of conservation. Here, two strictly conserved polar residues connect to ζ_2. They are both right next to a flexible glycine[XIV] on one side and an apolar side chain reaching down into the binding pocket on the other side. In the case of T39 in β_2, a second glycine follows (except for AppA and YcgF, which also possess slower back reaction rates than BlrB in UV/vis), creating a flexible hinge similar to a mechanical suspension. The second connector to ζ_2, E54, only possesses this flexibility on the outer side, while it is rigidly tied to glutamine Q51. Q51 is the main actor in the reorganization process of the hydrogen bond–network within the binding pocket after photoactivated proton coupled electron transfer[62]. Via E54, any

[XIV] Glycine is the smallest and thus most flexible amino acid with only a hydrogen atom at C_α.

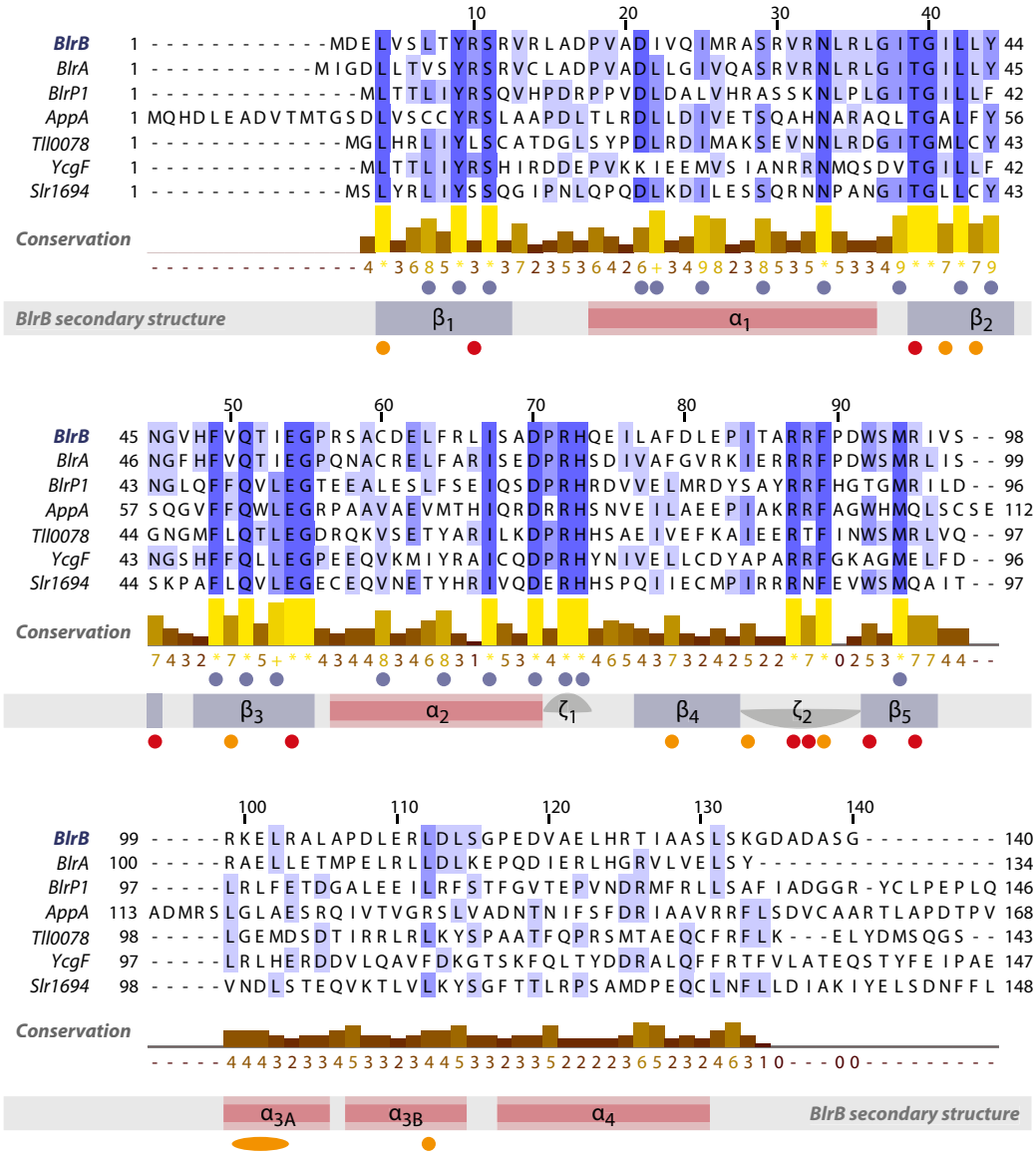

Figure 6.19: *Alignment of several BLUF domain sequences (the longer sequences have been truncated). The proteins with their accession code:* Rhodobacter sphaeroides *BlrB [Q3IYE4], BlrA [Q3IV98], AppA [Q53119];* Klebsiella pneumoniae *BlrP1 [A6T8V8];* Synechocystis *Slr1694 [P74295];* Escherichia coli *YcgF [P75990];* Thermosynechococcus elongatus *Tll0078 [Q8DMN3]. The highly conserved residues are marked with dots (blue for binding pocket/below the beta sheet; red for polar and orange for apolar above the beta sheet). The conserved loops have been called ζ_1 and ζ_2 for simplicity.*

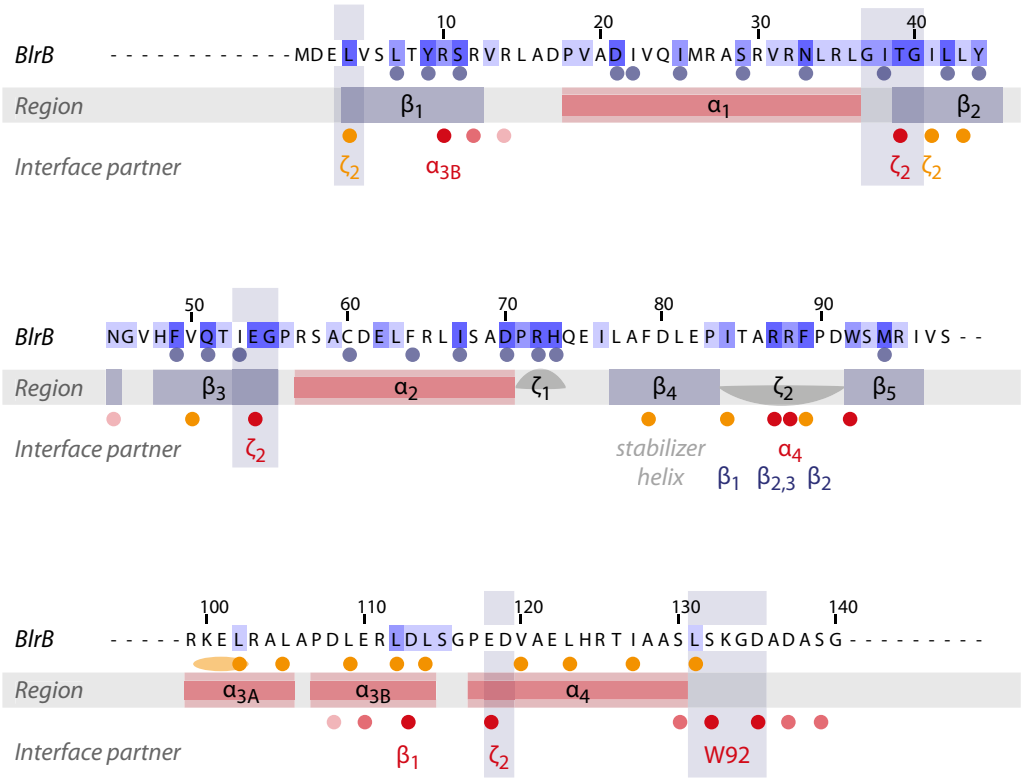

Figure 6.20: *Sequence for* R. sphaeroides *BlrB [Q3IYE4]. The polar conserved residues above the beta sheet nearly all interact with ζ_2. This loop is bound to β_2 by a GITG motive and to β_3 by an I/LEG motive. Possible interaction partners for W92 are highlighted at the end of α_4. All longer apolar residues in the C-terminal part have been marked orange. Polar residues of note are red.*

change in Q51's conformation can be transfered to the ζ_2 loop. In the center of the beta sheet, I41, L43 and V50 are conserved as apolar residues.

In the sequence further above follows helix α_2 (containing S58), which is connected to β_4 by the highly conserved, rigid turn ζ_1 (with the second main anchor Q74 at its end). Its rigid mounting together with the low conservation within this outer β_4 strand indicates its function to be a static, steric stabilizer for the protein and to pose as fulcrum for the leverage of its moving parts, especially for the following ζ_2 loop.

From the alignment perspective, ζ_2 is standing out because a) it is of high

conservation by itself, and b) because its conserved redidues all connect to other conserved residues we already mentioned: To L4 and I41 via van-der-Waals interactions (which allows sliding motion) and to the movable residues T39 and E54 by strong hydrogen bonds (salt bridges between their oxygens and the nitrogens of R87). In addition, it is linked to D119 or E118 by another salt bridge from R88, therefore mounting the beginning of α_4 onto this flexible suspension and directly linking it to small conformational changes of Q51 by its rigid link to E54.

This flexible mounting can also support movement of β_5, which is directly adjacent. The transition region is rather rigid in BlrB, but more flexible in AppA with an incorporated glycine, and completely mobile in BlrP1 and YcgF with another G**G motive also replacing the otherwise conserved tryptophan92.

The last strictly conserved residue in the sequence alignment is methionine94, one of the two most important residues for the protein's light reaction. It was identified together with its neighbor Q51 and the electron donor Y9 in the binding pocket as the three residues from the beta sheet that do not tolerate any mutational change without loss of function[47,55,127].

The question about the interplay between M94 and Q51 in the binding pocket is subject of intense research. Our measurements have shown that β_5 is in forward position in the dark state and in backward position in BlrB$_{light}$, defining the longitudinal position of M94 in both states for BlrB.

The measurements have also shown that these two actors are not only connected inside the binding pocket, but also by a strictly conserved system of leverage built into the protein backbone. From a mechanistic viewpoint, the following progression after light activation is most likely: a) The illumination causes the proton coupled electron transfer and a rearrangement of the hydrogen bonds follows, as discussed elsewhere. b) By this rearrangement, a tension is exerted from Q51 onto E54, but it is still locked by the rigid connection to β_5. c) The same rearrangement also causes M94 to snap back two integer positions in the beta sheet. The moving $beta_5$ strand allows ζ_2 and the attached α_4 to flap back with it, causing the observed distance shift in E110C/A129C, but not in S58C/A129C, because of the movement direction. d) This backward movement of β_5 also pulls down α_{3A}, while α_{3B} stays more or less fixed due to salt bridges

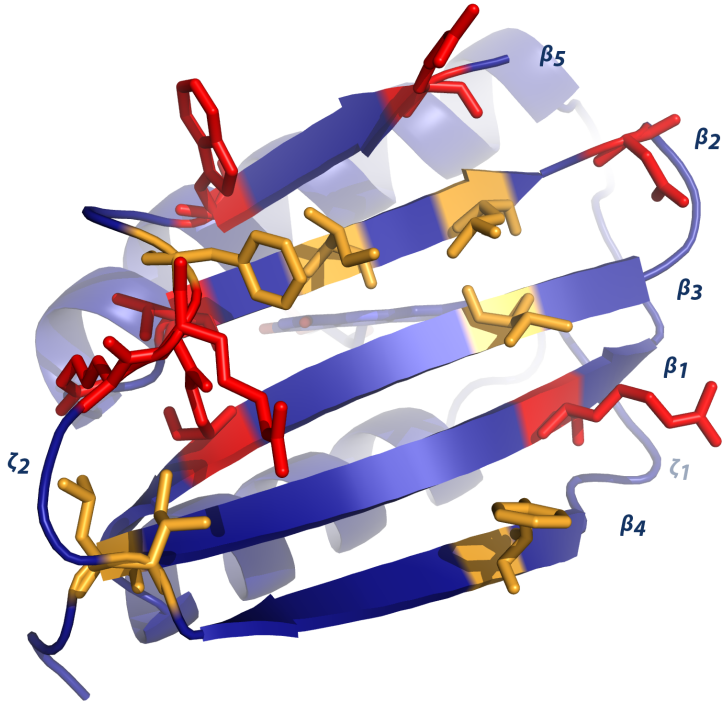

Figure 6.21: *BlrB – conserved residues above the beta sheet. Polar (red), apolar (orange).*

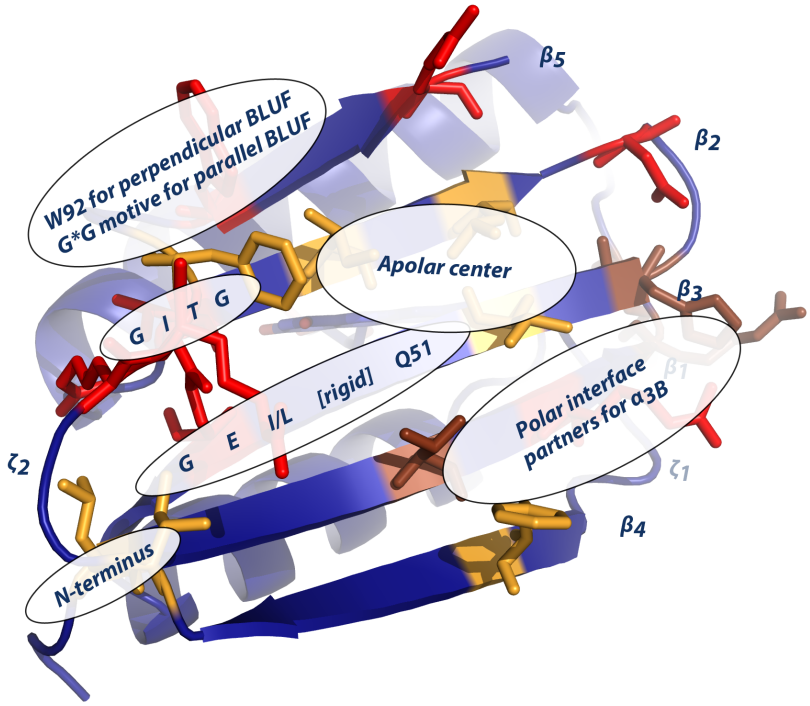

Figure 6.22: *The same as above, with added comments and polar, non-conserved residues in the vicinity of α_{3B} (redbrown).*

between its carboxylates D108, E110, and D113 and the arginine and histidine residues from β_1 and β_3. This causes the strong shifts observed in Q74C/K100C and especially in Q74C/A104C. e) In conclusion, the relatively closed surface from the dark state has completely exposed the central apolar amino acids as well as the apolar residues from α_{3A} and α_4. Now, the protein only has to diffuse to a suitable partner for further signal transduction. In the absence of such, it forms the observed homodimer.

Note, that this conformational change can take place without major bond breaking, even α_4 stays attached to ζ_2 and probably to W92. Accordingly, the NMR experiments from the abovementioned publication by Wu & Gardner[54] detect only few light dependent chemical shift changes. In figure 6.23 their results are mapped onto a sketch of the beta sheet, viewed from the C-terminal side. Residues not assigned even for BlrB$_{dark}$ are colored red (signifying proportionally strong chemical exchange under their measurement conditions) and with assigned, strong change in chemical shift colored purple except for M94, which is emphasized in orange. M94 exhibits the most substantial chemical shift of all assigned residues, which indeed can be correlated to its light induced translation along the beta sheet direction observed in this work.

The red, unassigned residues mainly correspond to regions involved in the change of conformation upon illumination. The beginning of ζ_2 where a separation from α_4 can occur, the hydrophobic core which is exposed, together with the lever mechanism at Q51 and the helix α_{3A} that is pulled down by the motion of M94 are the main regions with strong chemical exchange even in the dark, indicating a strong readiness for the light-induced shift in BlrB.

In addition, they also found strong variability in the chemical shifts in the vicinity of V31, namely they could not assign M26 and R27. Especially R27, which is pointing outward into the solvent, has no partner to interact with. This could back the explanation for the rotamer impediment of V31C to be caused by nearby interaction with the C-terminus (containing two carboxylates and several ionizable serines as ideal targets for salt bridges to arginine). A truncation by only 5 residues would render this additional bond sterically impossible. In their NMR experiments, a reduced stability was observed as consequence, W92, R88 and F89 would be the only residues still capable of holding α_4 in position.

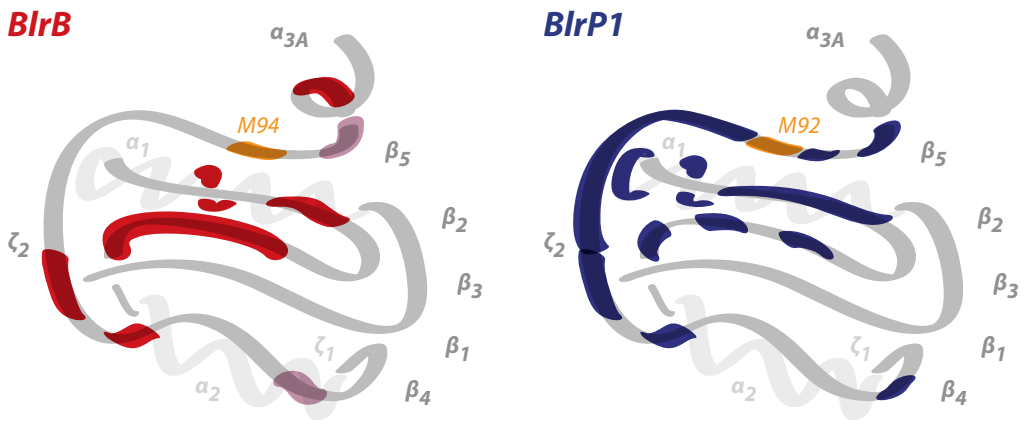

Figure 6.23: *From Wu & Gardner 2008[54] (left) and 2009[47] (right). For details, see text.*

The further reduction below 130 residues abolished flavin binding capability. Here, two effects have to be considered. This truncation removes the interface to W92, but it also removes parts of the α_4 helix which are hydrophobic itself and counterbalance α_{3A} not to flip inside onto the beta sheet in BlrB$_{dark}$. Thus, α_4 acts as a balancing lintel[XV] in the dark state, arching over one half of the hydrophobic core (while in the light state due to the translation of β_5, there is no risk of α_{3A} backflip).

Comparison to BlrP1

For *parallel* BLUF domains like BlrP1 from *Klebsiella pneumoniae*, the arrangement of the C-terminal tail is fundamentally different, while the structure of the body is conserved (see figure 6.24). α_{3A} is reduced to one turn and not named in the literature. α_{3B} becomes $\alpha_{3,BlrP1}$ and is located directly above and parallel to $\beta_{5,BlrP1}$. The following loop above $\zeta_{2,BlrP1}$ links to the $\alpha_{4,BlrP1}$ helix, which again runs parallel to the beta sheet directly above the hydrophobic center, and ends into a linker to the adjacent EAL domain. This linker is very rigidly bound at multiple sites in the same region as α_{3B} from BlrB, which remains in position upon illumination as found in this work, and additionally downwards to $\zeta_{1,BlrP1}$.

[XV] In architecture, a lintel is a structural element within the wall above a window opening, by which the static load is distributed to both sides.

The EAL domain of a second monomer is in vicinity to the C-terminal side of the first BlrP1 (shown in yellow in figure 6.24) and Barends et al. have suggested mutual interaction[3].

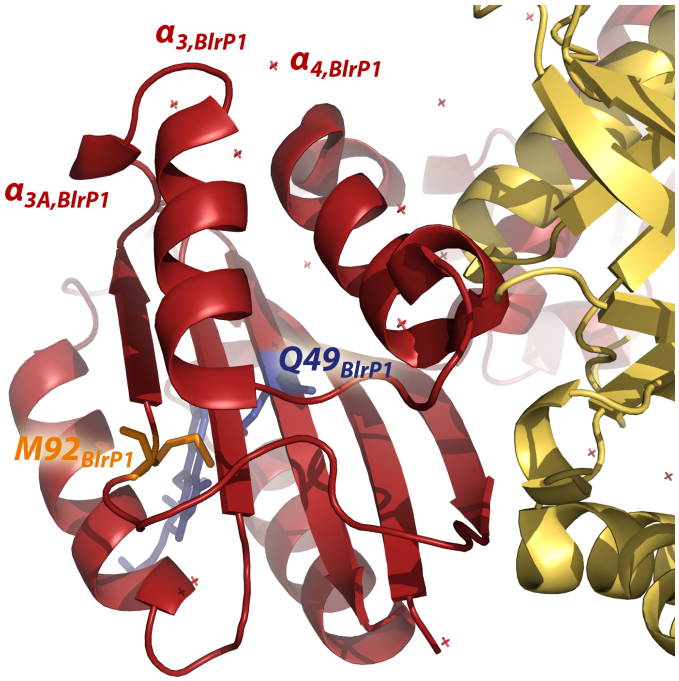

Figure 6.24: *Crystal structure of the* Klebsiella pneumoniae *BlrP1 dimer by Barends et al. 2009[3]. The second monomer is shown in yellow.*

As the body is conserved, the mechanism of signal propagation from the binding pocket must work in a similar fashion, but with differences in its effect on the tail. In 2009, Wu & Gardner have examined this protein with a similar set of NMR experiments as for BlrB, this time able to identify the majority of residues. The residues with significant chemical shift changes are shown in blue in figure 6.23, again $M92_{BlrP1}$ exhibits the strongest change (orange). This implies the same movement as found for BlrB. In addition, huge portions of the $\zeta_{2,BlrP1}$ loop, the $\beta_{5,BlrP1}$ strand and the hydrophobic center of the beta sheet experience strong changes in their surrounding. For instance, much stronger chemical shifts are observed for $T90_{BlrP1}$ than for its equivalent W92 from BlrB. BlrP1 (and YcgF) do not feature W92 (at equivalent number), but instead a very

flexible G**G motive (see sequence alignment in figure 6.19).

From our mechanistic viewpoint, this is easily explained because the movement of M92$_{BlrP1}$ will have a similar impact on $\alpha_{3A,BlrP1}$. However, the following C-terminal helices are ordered parallel to the beta strands, so a reorientation of the short $\alpha_{3A,BlrP1}$ in addition to the fixed fulcrum at the linker to the EAL domain will push them up, away from the beta sheet. This mechanism destroys the bond to $\zeta_{2,BlrP1}$, which causes strong changes in this region in the NMR signals.

In order to be able to still flap away $\zeta_{2,BlrP1}$ while breaking the bridges from R86$_{BlrP1}$ and H88$_{BlrP1}$ to the C-terminus with a nearly identical connection to Q49$_{BlrP1}$, the mounting at $\beta_{5,BlrP1}$ needs to be more flexible, hence the G**G motive. As a consequence from stronger reorientation in this region, also the corresponding region of α_1 below is affected by chemical shift changes. The two sequences in question (BlrP1 and YcgF) also have the shortest possible N-terminus, further assuring maximum flexibility of ζ_2 (while AppA with its very slow reversion time constant has the longest N-terminus, which might restrain the back reaction in this specimen by keeping ζ_2 in opened position).

In the end, the same exposure of the central hydrophobic residues ensues as in BlrB, but the increased expenditure to achieve the described, larger conformational change suggests the actual effect on EAL being caused by the steric rearrangement and the hydrophobic interaction providing a means to reliably switch back from the active form and reinstate the bond to $\zeta_{2,BlrP1}$.

Comparison to LOV domains

When looking for analogies in other blue–light sensing flavoproteins, the LOV domains are very similar equivalents. They occur predominantly in phototropins as N-terminal domain with a Ser/Thr kinase as effector domain linked at the C-terminus[128]. These domains possess a similar five-stranded beta sheet in same orientation to the flavin cofactor as BLUF domains and also additional helical regions on its backside. However unlike BLUF, upon illumination a covalent bond between the flavin and a nearby cysteine is formed[129]. This is a potent interaction, and it has strong repercussions on the network geometry of the binding pocket. Already small changes in the cavity region most distant from the reac-

tive cysteine and the polar pyrimidone ring of the flavin isoalloxazine moiety can substantially affect the stability of this bond[71]. The bottom line then is very comparable to the effects of the hydrogen bond switch reaction in BLUF domains in that somehow the small change in the binding pocket is relayed to an outside surface effect[130].

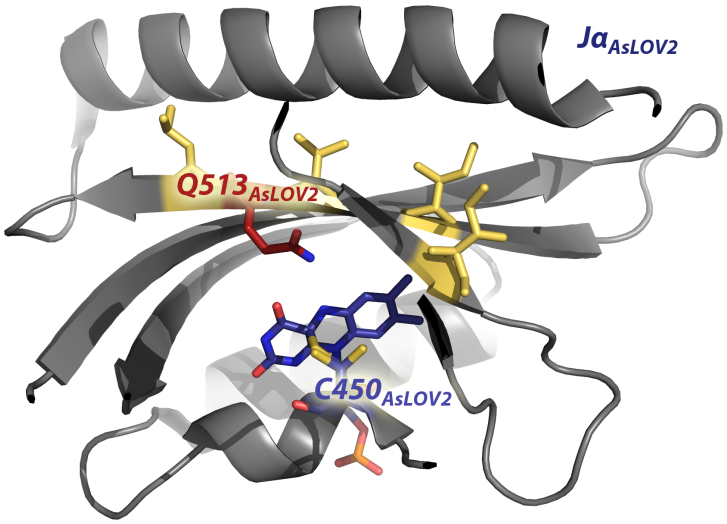

Figure 6.25: *Crystal structure 2V0W of the LOV2 domain from* Avena sativa *NPH1-1 phototropin by Halavaty & Moffat 2007[131]. The C4a–adduct is seen as one conformation for C450.*

By regarding different crystal structures of LOV[131,132,133,134] (figure 6.25 shows the 2V0W structure of *Avena sativa* LOV2), it becomes apparent that the beta sheet has a very similar apolar region as the BLUF domains. In the crystal structure of *Avena sativa* LOV2, a long helix (called the Jα) is positioned directly above, similar to the C-terminal tail in BLUF. In 2007, Halavaty and Moffat recorded conformational changes of this helix upon illumination[131], but the secondary structure broke at one point probably due to crystal contacts, which illustrates the power behind the potential conformational change. In the central beta strand below, they also saw a light induced changes of glutamine513$_{AsLOV2}$, which is at exactly the same position relative to the cofactor as Q51 in BlrB.

This whole configuration is a strong analogy to the BLUF structure, where M94 and Q51 both substantially affect the conformation of the helical C-terminal

tail. Figure 6.26 depicts an alignment of four LOV domains, showing its high degree of conservation. Right next to the strictly conserved $Q513_{AsLOV2}$, a mobile glycine hinge is found in same incidence, just like in the BLUF domain leverage system. This motive (including the surrounding apolar residues) is conserved throughout all LOV domains[131,135] and allows the Q51 analogon to straightforwardly impact the conformation of Jα upon formation of the C4a–adduct.

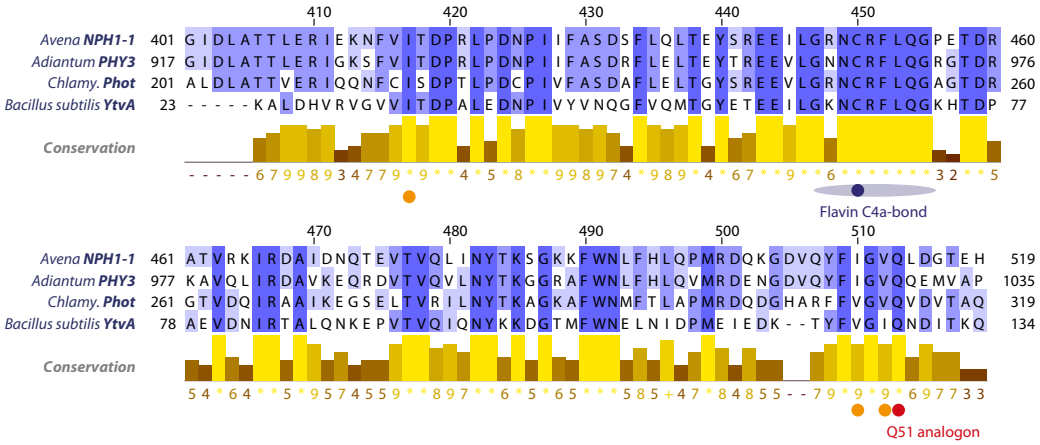

Figure 6.26: *Alignment for four LOV domains. The proteins with their accession code and PDB identifier:* Avena sativa *NPH1-1, LOV 2 [O49003, 2V0U/2V0W];* Adiantum capillus-veneris *Phy3, LOV 2 [Q9ZWQ6, 1G28];* Chlamydomonas reinhardtii *Phot, LOV 2 [Q8LPE0; 1N9O/1N9N for LOV 1];* Bacillus subtilis *pfyP/YtvA, LOV [O34627, 2PR5/2PR6].*

In the X-ray structure of YtvA LOV from *Bacillus subtilis*, the apolar region in the beta sheet serves as interface for a homodimer[134], while the Jα helix is turned away by 180°. The functional full length protein however, which contains an additional STAS domain at the C-terminus, has been found monomeric in solution[135]. Thus, the observed Jα orientation must stem from the truncation and indicates the presence of a wider interdependency moderated via the backbone, as it has been observed in this work for the BlrB BLUF domain. The different configuration for the cut-out LOV domain can be compared to the truncation experiments of Wu & Gardner on BlrB[54], leading to reduced or perished functionality in this case.

Further expansion of the compared organisms showed that for fungi, Zoltowski et al.[136] observed a light induced flip of the Q51 equivalent in the LOV re-

lated VVD photoreceptor of *Neurospora crassa* already in 2007. They proposed a model of the Q51 analogon relaying the effect of C4a–adduct formation to the hinged suspension of the C-terminal (in that specific organism N-terminal) helix region and thus effecting major conformational changes therein. This was fortified in 2009 by Alexandre et al. for plant phototropins, as they identified a conserved network of two asparagines and the Q51 equivalent to manifest relevant changes induced by the C4a–adduct formation with FTIR spectroscopy.

Given the strict conservation of both the binding pocket and the suspension of the C-terminal helices onto the hinge region next to the Q51 equivalent, and given conservation of the BLUF domain's analog and fundamental mechanism regardless of C-terminal configuration (as argued above), it is evident that this amplification of a small change within the flavin binding pocket into a large conformational shift on the backside of the beta sheet is also the prime mechanism of all LOV domains. The necessity of the backbone framework in BLUF and the contradicting results for cut-out LOV domains indicates a similar dependency on outside leverage. Restraining the view to the flavin side of the beta sheet does not reflect the whole picture, neither in BLUF nor in LOV.

6.3 Synopsis

Within this chapter, the ELDOR distance measurements on the *R. sphaeroides* BlrB BLUF protein could *directly* detect a significant conformational shift in its C-terminal tail region upon illumination. The exposure of central hydrophobic residues in the beta sheet is the consequence, and it leads to formation of a defined BlrB homodimer. *In vivo*, the formation of a heterodimer with activation of an unidentified partner protein is equally possible.

A model for the dependencies of the backbone interplay could be derived. The concerted mechanism of Q51 change and M94 translation by straight connection to both the cofactor and one-another within the active region of the binding pocket, as well as by the described far-reaching impact of backbone conformation, is a highly complex system of signal propagation and amplification through a beta sheet. As discussed, systems with one participant residue removed cannot support function.

The correlation to LOV domains with a more potent formation of a covalent flavin adduct pointed at an equivalent (but probably single tracked) mechanism with an identically functioning analogon to Q51. M94 has no direct counterpart in LOV, its necessity is probably based on the BLUF mechanism starting from a weaker initial effect (hydrogen bonds vs. covalent bond). The double effort is more complicated, but has better efficiency in spreading conformational change over wide regions of the protein.

Conclusion

Combining structural information from crystallography with the advantages of EPR and especially ELDOR spectroscopy has been proven by this work to be a very effective and reliable way of acquiring valid structural information for proteins in solution.

Not only could the tertiary structure from the crystal be supported in the disputed case of the DnaJ GF-domain free in solution as well as in interaction with the DafA substrate, but the reorientation of its quaternary structure was clearly documented. As many chaperones rely on amorphous hydrophobic interactions and can only be crystallized alone, but not with substrate, ELDOR analysis is a powerful method to research these mutual inter-protein reactions.

In the case of BlrB, the ELDOR method demonstrated its power to selectively monitor one interaction within a protein with no crystal constraints. It was thus possible to directly observe its C-terminal tail undergo a major conformational change upon illumination with blue light.

Here this leads to an exposed apolar interface region, creating a homodimer in solution *in vitro*. BlrB as an isolated BLUF domain must rely on inter-protein interaction for the further transduction of the light signal *in vivo*.

Correlation to literature data suggested that this kind of relayed conformational change could possibly be a very widespread mechanism, which has been less apparent than the intra-binding pocket interactions as it often cannot be detected by crystallography. In these cases as much as in general, only a combination of different spectroscopic methods leads to a consistent picture of a protein's function.

Bibliography

[1] **A. Möglich, X. J. Yang, R. A. Ayers and K. Moffat**. 2010. "*Structure and Function of Plant Photoreceptors*" Annual Review of Plant Biology **61** 21–47.

[2] **Erik Zuiderweg, Eric Bertelsen, Aikaterini Rousaki, Matthias Mayer, Jason Gestwicki and Atta Ahmad**. 2012. "*Allostery in the Hsp70 Chaperone Proteins*", chapter 1 of 1–55. Springer Berlin / Heidelberg.

[3] **T. R. M. Barends, E. Hartmann, J. J. Griese, T. Beitlich, N. V. Kirienko, D. A. Ryjenkov, J. Reinstein, R. L. Shoeman, M. Gomelsky and I. Schlichting**. 2009. "*Structure and mechanism of a bacterial light-regulated cyclic nucleotide phosphodiesterase*" Nature **459** (7249):1015–1018.

[4] **A. Jung, T. Domratcheva, M. Tarutina, Q. Wu, W. H. Ko, R. L. Shoeman, M. Gomelsky, K. H. Gardner and L. Schlichting**. 2005. "*Structure of a bacterial BLUF photoreceptor: Insights into blue light-mediated signal transduction*" Proceedings of the National Academy of Sciences of the United States of America **102** (35):12350–12355.

[5] **K. Motohashi, H. Taguchi, N. Ishii and M. Yoshida**. 1994. "*Isolation of the Stable Hexameric DnaK-DnaJ Complex From Thermus-thermophilus*" Journal of Biological Chemistry **269** (43):27074–27079.

[6] **Y. Kobayashi, A. Kume, M. Li, M. Doyu, M. Hata, K. Ohtsuka and G. Sobue**. 2000. "*Chaperones Hsp70 and Hsp40 suppress aggregate formation and apoptosis in cultured neuronal cells expressing truncated androgen receptor protein with expanded polyglutamine tract*" Journal of Biological Chemistry **275** (12):8772–8778.

[7] **L. Hendershot, J. Wei, J. Gaut, J. Melnick, S. Aviel and Y. Argon**. 1996. "*Inhibition of immunoglobulin folding and secretion by dominant negative BiP ATPase mutants*" Proceedings of the National Academy of Sciences **93** (11):5269–5274.

[8] **J.F. Simons, S. Ferro Novick, M.D. Rose and A. Helenius**. 1995. "*BiP/Kar2p serves as a molecular chaperone during carboxypeptidase Y folding in yeast.*" Journal of Cell Biology **130** (0021-9525 (Linking)):41-49.

[9] **J. P. Hendrick and F. U. Hartl**. 1993. "*Molecular Chaperone Functions of Heat-shock Proteins*" Annual Review of Biochemistry **62** 349–384.

[10] **X. B. Qiu, Y. M. Shao, S. Miao and L. Wang**. 2006. "*The diversity of the DnaJ/Hsp40 family, the crucial partners for Hsp70 chaperones*" Cellular and Molecular Life Sciences **63** (22):2560–2570.

[11] **J. P. Hendrick, T. Langer, T. A. Davis, F. U. Hartl and M. Wiedmann**. 1993. "*Control of Folding and Membrane Translocation By Binding of the Chaperone Dnaj To Nascent Polypeptides*" Proceedings of the National Academy of Sciences of the United States of America **90** (21):10216–10220.

[12] **A. K. Corsi and R. Schekman**. 1997. "*The lumenal domain of Sec63p stimulates the ATPase activity of BiP and mediates BiP recruitment to the translocon in Saccharomyces cerevisiae*" Journal of Cell Biology **137** (7):1483–1493.

[13] **P. Bork, C. Sander, A. Valencia and B. Bukau**. 1992. "*A Module of the Dnaj Heat-shock Proteins Found In Malaria Parasites*" Trends In Biochemical Sciences **17** (4):129–129.

[14] **A. J. Caplan, D. M. Cyr and M. G. Douglas**. 1993. "*Eukaryotic Homologs of Escherichia-coli Dnaj - A Diverse Protein Family That Functions With Hsp70 Stress Proteins*" Molecular Biology of the Cell **4** (6):555–563.

[15] **P. Walsh, D. Bursac, Y. C. Law, D. Cyr and T. Lithgow**. 2004. "*The J-protein family: modulating protein assembly, disassembly and translocation*" Embo Reports **5** (6):567–571.

[16] **B. Bukau and A. L. Horwich**. 1998. "*The Hsp70 and Hsp60 chaperone machines*" Cell **92** (3):351–366.

[17] **Y. Minami, J. Hohfeld, K. Ohtsuka and F. U. Hartl**. 1996. "*Regulation of the heat-shock protein 70 reaction cycle by the mammalian DnaJ homolog, Hsp40*" Journal of Biological Chemistry **271** (32):19617–19624.

[18] **A. W. Russell, A. F. Mehl and R. McMacken**. 1999. "*DnaJ Dramatically Stimulates ATP Hydrolysis by DnaK: Insight into Targeting of Hsp70 Proteins to Polypeptide Substrates*" Biochemistry **38** 4165-4176.

[19] **K. Motohashi, M. Yohda, M. Odaka and M. Yoshida**. 1997. "*K+ is an indispensable cofactor for GrpE stimulation of ATPase activity of DnaK center dot DnaJ complex from Thermus thermophilus*" Febs Letters **412** (3):633–636.

[20] **S. Popp, L. Packschies, N. Radzwill, K. P. Vogel, H. A. Steinhoff and J. Reinstein**. 2005. "*Structural dynamics of the DnaK-peptide complex*" Journal of Molecular Biology **347** (5):1039–1052.

[21] **D. Klostermeier, R. Seidel and J. Reinstein**. 1999. "*The functional cycle and regulation of the Thermus thermophilus DnaK chaperone system*" Journal of Molecular Biology **287** (3):511–525.

[22] **T. Laufen, M. P. Mayer, C. Beisel, D. Klostermeier, A. Mogk, J. Reinstein and B. Bukau**. 1999. "*Mechanism of regulation of Hsp70 chaperones by DnaJ cochaperones*" Proceedings of the National Academy of Sciences of the United States of America **96** (10):5452–5457.

[23] **D. M. Cyr, T. Langer and M. G. Douglas**. 1994. "*Dnaj-like Proteins - Molecular Chaperones and Specific Regulators of Hsp70*" Trends In Biochemical Sciences **19** (4):176–181.

[24] **M. E. Cheetham and A. J. Caplan**. 1998. "*Structure, function and evolution of DnaJ: conservation and adaptation of chaperone function*" Cell Stress & Chaperones **3** (1):28–36.

[25] **Y. Q. Hu, Z. M. Zhou, X. Y. Huang, M. Xu, L. Lu, Z. Y. Xu, J. M. Li and J. H. Sha**. 2004. "*Expression of a novel DnaJA1 alternative splicing in human testis and sperm*" International Journal of Andrology **27** (6):343–349.

[26] **K. Terada, K. Yomogida, T. Imai, H. Kiyonari, N. Takeda, T. Kadomatsu, M. Yano, S. Aizawa and M. Mori**. 2005. "*A type I DnaJ homolog, DjA1, regulates androgen receptor signaling and spermatogenesis*" Embo Journal **24** (3):611–622.

[27] **M. Pellecchia, T. Szyperski, D. Wall, C. Georgopoulos and K. Wuthrich**. 1996. "*NMR structure of the J-domain and the Gly/Phe-rich region of the Escherichia coli DnaJ chaperone*" Journal of Molecular Biology **260** (2):236–250.

[28] **T. Szyperski, M. Pellecchia, D. Wall, C. Georgopoulos and K. Wuthrich**. 1994. "*Nmr Structure Determination of the Escherichia-coli Dnaj Molecular Chaperone - Secondary Structure and Backbone Fold of the N-terminal Region (residues-2-108) Containing the Highly Conserved J-domain*" Proceedings of the National Academy of Sciences of the United States of America **91** (24):11343–11347.

[29] **Yan Qiu Qian, Dinshaw Patel, F. Ulrich Hartl and Damian J. McColl**. 1996. "*Nuclear Magnetic Resonance Solution Structure of the Human Hsp40 (HDJ-1) J-domain*" Journal of Molecular Biology **260** (2):224–235.

[30] **D. Wall, M. Zylicz and C. Georgopoulos**. 1994. "*The Nh2-terminal 108 Amino-acids of the Escherichia-coli Dnaj Protein Stimulate the Atpase Activity of Dnak and Are Sufficient For Lambda-replication*" Journal of Biological Chemistry **269** (7):5446–5451.

[31] **F. Hennessy, W. S. Nicoll, R. Zimmermann, M. E. Cheetham and G. L. Blatch**. 2005. "*Not all J domains are created equal: Implications for the specificity of Hsp40-Hsp70 interactions*" Protein Science **14** (7):1697–1709.

[32] **Jingzhi Li, Yunkun Wu, Xinguo Qian and Bingdong Sha**. 2006. "*Crystal structure of yeast Sis1 peptide-binding fragment and Hsp70 Ssa1 C-terminal complex*" Biochemical Journal **398** 353–360.

[33] **Junbin Hu, Yunkun Wu, Jingzhi Li, Xinguo Qian, Zhengqing Fu and Bingdong Sha**. 2008. "*The crystal structure of the putative peptide-binding fragment from the human Hsp40 protein Hdj1*" Bmc Structural Biology **8** 3.

[34] **K. Huang, J. M. Flanagan and J. H. Prestegard**. 1999. "*The influence of C-terminal extension on the structure of the J-domain in E-coli DnaJ*" Protein Science **8** (1):203–214.

[35] **K. Huang, R. Ghose, J. M. Flanagan and J. H. Prestegard**. 1999. "*Backbone dynamics of the n-terminal domain in E-coli DnaJ determined by N-15- and (CO)-C-13-relaxation measurements*" Biochemistry **38** (32):10567–10577.

[36] **W. L. Kelley**. 1998. "*The J-domain family and the recruitment of chaperone power*" Trends In Biochemical Sciences **23** (6):222–227.

[37] **W. Yan and E. A. Craig**. 1999. "*The glycine-phenylalanine-rich region determines the specificity of the yeast Hsp40 Sis1*" Molecular and Cellular Biology **19** (11):7751–7758.

[38] **D. Wall, M. Zylicz and C. Georgopoulos**. 1995. "*The Conserved G/f Motif of the Dnaj Chaperone Is Necessary For the Activation of the Substrate-binding Properties of the Dnak Chaperone*" Journal of Biological Chemistry **270** (5):2139–2144.

[39] **Ken Motohashi, Masafumi Yohda, Isao Endo and Masasuke Yoshida**. 1996. "*A Novel Factor Required for the Assembly of the DnaK and DnaJ Chaperones of Thermus thermophilus*" Journal of Biological Chemistry **271** (29):17343–17348.

[40] **S. Schlee and J. Reinstein**. 2002. "*The DnaK/ClpB chaperone system from Thermus thermophilus*" Cellular and Molecular Life Sciences **59** (10):1598–1606.

[41] **Y. Watanabe and M. Yoshida**. 2004. "*Trigonal Dnak-DnaJ complex versus free DnaK and DnaJ - Heat stress converts the former to the latter, and only the latter can do disaggregation in cooperation with ClpB*" Journal of Biological Chemistry **279** (16):15723–15727.

[42] **G. L. Dumitru, Y. Groemping, D. Klostermeier, T. Restle, E. Deuerling and J. Reinstein**. 2004. "*DafA cycles between the DnaK chaperone system and translational machinery*" Journal of Molecular Biology **339** (5):1179–1189.

[43] **P. J. Muchowski and J. L. Wacker**. 2005. "*Modulation of neurodegeneration by molecular chaperones*" Nature Reviews Neuroscience **6** (1):11–22.

[44] **Jennifer L. Wacker, Shao Yi Huang, Andrew D. Steele, Rebecca Aron, Gregor P. Lotz, QuangVu Nguyen, Flaviano Giorgini, Erik D. Roberson, Susan Lindquist, Eliezer Masliah and Paul J. Muchowski**. 2009. "*Loss of Hsp70 Exacerbates Pathogenesis But Not Levels of Fibrillar Aggregates in a Mouse Model of Huntington's Disease*" Journal of Neuroscience **29** (28):9104–9114.

[45] **Michael A. Horst and Klaas J. Hellingwerf**. 2003. "*Photoreceptor Proteins, Star Actors of Modern Times. A Review of the Functional Dynamics in the Structure of Representative Members of Six Different Photoreceptor Families*" Acc. Chem. Res. **37** (1):13–20.

[46] **A. Kita, K. Okajima, Y. Morimoto, M. Ikeuchi and K. Miki**. 2005. "*Structure of a cyanobacterial BLUF protein, Tll0078, containing a novel FAD-binding blue light sensor domain*" Journal of Molecular Biology **349** (1):1–9.

[47] **Q. Wu and K. H. Gardner**. 2009. "*Structure and Insight into Blue Light-Induced Changes in the BlrP1 BLUF Domain*" Biochemistry **48** (12):2620–2629.

[48] **S. Anderson, V. Dragnea, S. Masuda, J. Ybe, K. Moffat and C. Bauer**. 2005. "*Structure of a novel photoreceptor, the BLUF domain of AppA from Rhodobacter sphaeroides*" Biochemistry **44** (22):7998–8005.

[49] **J. S. Grinstead, S. T. D. Hsu, W. Laan, A. M. J. J. Bonvin, K. J. Hellingwerf, R. Boelens and R. Kaptein**. 2006. "*The solution structure of the AppA BLUF domain: Insight into the mechanism of light-induced signaling*" Chembiochem **7** (1):187–193.

[50] **H. Yuan, S. Anderson, S. Masuda, V. Dragnea, K. Moffat and C. Bauer**. 2006. "*Crystal structures of the Synechocystis photoreceptor Slr1694 reveal distinct structural states related to signaling*" Biochemistry **45** (42):12687–12694.

[51] **M. Iseki, S. Matsunaga, A. Murakami, K. Ohno, K. Shiga, K. Yoshida, M. Sugai, T. Takahashi, T. Hori and M. Watanabe**. 2002. "*A blue-light-*

activated adenylyl cyclase mediates photoavoidance in Euglena gracilis" Nature **415** (6875):1047–1051.

[52] **M. Gomelsky and S. Kaplan**. 1998. "*AppA, a redox regulator of photosystem formation in Rhodobacter sphaeroides 2.4.1, is a flavoprotein - Identification of a novel FAD binding domain*" Journal of Biological Chemistry **273** (52):35319–35325.

[53] **S. Masuda and C. E. Bauer**. 2002. "*AppA is a blue light photoreceptor that antirepresses photosynthesis gene expression in Rhodobacter sphaeroides*" Cell **110** (5):613–623.

[54] **Qiong Wu, Wen Huang Ko and Kevin H. Gardner**. 2008. "*Structural Requirements for Key Residues and Auxiliary Portions of a BLUF Domain*" Biochemistry **47** (39):10271–10280.

[55] **A. Jung, J. Reinstein, T. Domratcheva, R. L. Shoeman and I. Schlichting**. 2006. "*Crystal structures of the AppA BLUF domain photoreceptor provide insights into blue light-mediated signal transduction*" Journal of Molecular Biology **362** (4):717–732.

[56] **M. Gomelsky and G. Klug**. 2002. "*BLUF: a novel FAD-binding domain involved in sensory transduction in microorganisms*" Trends In Biochemical Sciences **27** (10):497–500.

[57] **H. Yuan and C. E. Bauer**. 2008. "*PixE promotes dark oligomerization of the BLUF photoreceptor PixD*" Proceedings of the National Academy of Sciences of the United States of America **105** (33):11715–11719.

[58] **P. Zirak, A. Penzkofer, T. Schiereis, P. Hegemann, A. Jung and I. Schlichting**. 2006. "*Photodynamics of the small BLUF protein BlrB from Rhodobacter sphaeroides*" Journal of Photochemistry and Photobiology B-biology **83** (3):180–194.

[59] **Stefan Weber, Claudia Schroeder, Sylwia Kacprzak, Tilo Mathes, Radoslaw M. Kowalczyk, Lars Oliver Essen, Peter Hegemann, Erik Schleicher and Robert Bittl**. 2011. "*Light-generated Paramagnetic Intermediates in BLUF Domains*" Photochemistry and Photobiology **87** (3):574–583.

[60] **M. Gauden, I. H. M. Stokkum, J. M. Key, D. C. Luhrs, R. Van Grondelle, P. Hegemann and J. T. M. Kennis**. 2006. "*Hydrogen-bond switching through a radical pair mechanism in a flavin-binding photoreceptor*" Proceedings of the National Academy of Sciences of the United States of America **103** (29):10895–10900.

[61] **Cosimo Bonetti, Manuela Stierl, Tilo Mathes, Ivo H. M. Stokkum, Katharine M. Mullen, Thomas A. Cohen Stuart, Rienk Grondelle, Peter Hegemann and John T. M. Kennis**. 2009. "*The Role of Key Amino Acids in the Photoactivation Pathway of the Synechocystis Slr1694 BLUF Domain*" Biochemistry **48** (48):11458–11469.

[62] **Tilo Mathes, Ivo H. M. Stokkum, Cosimo Bonetti, Peter Hegemann and John T. M. Kennis**. 2011. "*The Hydrogen-Bond Switch Reaction of the Blrb Bluf Domain of Rhodobacter sphaeroides*" J. Phys. Chem. B **115** (24):7963–7971.

[63] **T. Domratcheva, B. L. Grigorenko, I. Schlichting and A. V. Nemukhin**. 2008. "*Molecular models predict light-induced glutamine tautomerization in BLUF photoreceptors*" Biophysical Journal **94** (10):3872–3879.

[64] **Tilo Mathes, Jingyi Zhu, Ivo H. M. Stokkum, M. L. Groot, Peter Hegemann and John T. M. Kennis**. 2011. "*Hydrogen Bond Switching among Flavin and Amino Acids Determines the Nature of Proton-Coupled Electron Transfer in BLUF Photoreceptors*" J. Phys. Chem. Lett. **3** (2):203–208.

[65] **P. Zirak, A. Penzkofer, T. Schiereis, P. Hegemann, A. Jung and I. Schlichting**. 2005. "*Absorption and fluorescence spectroscopic characterization of BLUF domain of AppA from Rhodobacter sphaeroides*" Chemical Physics **315** (1-2):142–154.

[66] **Magdalena Gauden, Jeffrey S. Grinstead, Wouter Laan, Ivo H. M. Stokkum, Marcela Avila Perez, K. C. Toh, Rolf Boelens, Robert Kaptein, Rienk Grondelle, Klaas J. Hellingwerf and John T. M. Kennis**. 2007. "*On the Role of Aromatic Side Chains in the Photoactivation of BLUF Domains*" Biochemistry **46** (25):7405–7415.

[67] **Wouter Laan, Teresa Bednarz, Joachim Heberle and Klaas J. Hellingwerf**. 2004. "*Chromophore composition of a heterologously expressed BLUF-domain*" Photochem. Photobiol. Sci. **3** (11-12):1011–1016.

[68] **Vincent Massey and Graham Palmer**. 1966. "*On the Existence of Spectrally Distinct Classes of Flavoprotein Semiquinones. A New Method for the Quantitative Production of Flavoprotein Semiquinones*" Biochemistry **5** (10):3181–3189.

[69] **Erik Schleicher and Stefan Weber** 2012. "*Flavins & Flavoprotein Protocols*" Humana Press, Inc.

[70] **Winslow Briggs**. 2007. "*The LOV domain: a chromophore module servicing multiple photoreceptors*", Journal of Biomedical Science **14**: 499–504. Springer Netherlands.

[71] **Richard Brosi, Boris Illarionov, Tilo Mathes, Markus Fischer, Monika Joshi, Adelbert Bacher, Peter Hegemann, Robert Bittl, Stefan Weber and Erik Schleicher**. 2010. "*Hindered Rotation of a Cofactor Methyl Group as a Probe for Protein–Cofactor Interaction*" J. Am. Chem. Soc. **132** (26):8935–8944.

[72] **Manuela Stierl, Patrick Stumpf, Daniel Udwari, Ronnie Gueta, Rolf Hagedorn, Aba Losi, Wolfgang Gartner, Linda Petereit, Marina Efetova, Martin Schwarzel, Thomas G. Oertner, Georg Nagel and Peter Hegemann**. 2011. "*Light Modulation of Cellular cAMP by a Small Bacterial Photoactivated Adenylyl Cyclase, bPAC, of the Soil Bacterium Beggiatoa*" J. Biol. Chem. **286** (2):1181–1188.

[73] **Min Hyung Ryu, Oleg V. Moskvin, Jessica Siltberg Liberles and Mark Gomelsky**. 2010. "*Natural and Engineered Photoactivated Nucleotidyl Cyclases for Optogenetic Applications*" Journal of Biological Chemistry **285** (53):41501–41508.

[74] **Saskia Schroder Lang, Martin Schwarzel, Reinhard Seifert, Timo Strunker, Suneel Kateriya, Jens Looser, Masakatsu Watanabe, U Benjamin Kaupp, Peter Hegemann and Georg Nagel**. 2007. "*Fast manipulation of cellular cAMP level by light in vivo*" Nat Meth **4** (1):39–42.

[75] **A. Schweiger and G. Jeschke** 2001. "*Principles of pulse electron paramagnetic resonance*" Oxford University Press.

[76] **A. Carrington and A.D. McLachlan** 1979. "*Introduction to magnetic resonance: with applications to chemistry and chemical physics*" Chapman and Hall.

[77] **J.A. Weil and J.R. Bolton** 2007. "*Electron Paramagnetic Resonance: Elementary Theory and Practical Applications*" John Wiley & Sons.

[78] **Walther Gerlach and Otto Stern**. 1922. "*Der experimentelle Nachweis der Richtungsquantelung im Magnetfeld*" Zeitschrift für Physik A Hadrons and Nuclei **9** 349.

[79] **Pieter Zeeman**. 1897. "*On the influence of Magnetism on the Nature of the Light emitted by a Substance.*" Philosophical Magazine **43** 226.

[80] **Yevgeny K. Zavoisky**. 1945. "*Measurements on CuCl2·2H2O*" Journal of Physics USSR **9** 221.

[81] **Yevgeny K. Zavoisky**. 1946. "*Paramagnetic Absorption In Some Salts In Perpendicular Magnetic Fields*" Zhurnal Eksperimentalnoi I Teoreticheskoi Fiziki **16** (7):603–606.

[82] **B. Odom, D. Hanneke, B. D'Urso and G. Gabrielse**. 2006. "*New measurement of the electron magnetic moment using a one-electron quantum cyclotron*" Physical Review Letters **97** (3):030801.

[83] **E. L. Hahn**. 1950. "*Spin Echoes*" Physical Review **80** (4):580–594.

[84] **Charles P. Poole and Horacio A. Farach** 1971. "*Relaxation in Magnetic Resonance*" Academic Press, Inc..

[85] **A. Einstein**. 1916. "*Zur Quantentheorie der Strahlung*" Physikalische Gesellschaft Zürich, Mitteilungen **16** 47-62.

[86] **K. D. Bowers and W. B. Mims**. 1959. "*Paramagnetic Relaxation In Nickel Fluosilicate*" Physical Review **115** (2):285–295.

[87] **A. D. Milov, K. M. Salikohov and M. D. Shirov**. 1981. "*Application of Endor In Electron-spin Echo For Paramagnetic Center Space Distribution In Solids*" Fizika Tverdogo Tela **23** (4):975–982.

[88] **A. D. Milov, A. B. Ponomarev and Y. D. Tsvetkov**. 1984. "*Electron Electron Double-resonance In Electron-spin Echo - Model Biradical Systems and the Sensitized Photolysis of Decalin*" Chemical Physics Letters **110** (1):67–72.

[89] **A. D. Milov, A. B. Ponomarev and Y. D. Tsvetkov**. 1984. "*Modulation Beats of Signal of Double Electron-electron Resonance In Spin-echo For Biradical Systems*" Journal of Structural Chemistry **25** (5):710–713.

[90] **H. Hara, A. Kawamori, A. V. Astashkin and T. Ono**. 1996. "*The distances from tyrosine D to redox-active components on the donor side of Photosystem II determined by pulsed electron-electron double resonance*" Biochimica Et Biophysica Acta-bioenergetics **1276** (2):140–146.

[91] **A. V. Astashkin, Y. Kodera and A. Kawamori**. 1994. "*Distance Between Tyrosines Z(+) and D+ In Plant Photosystem-ii As Determined By Pulsed Epr*" Biochimica Et Biophysica Acta-bioenergetics **1187** (1):89–93.

[92] **R. E. Martin, M. Pannier, F. Diederich, V. Gramlich, M. Hubrich and H. W. Spiess**. 1998. "*Determination of end-to-end distances in a series of TEMPO diradicals of up to 2.8 nm length with a new four-pulse double electron electron resonance experiment*" Angewandte Chemie-international Edition **37** (20):2834–2837.

[93] **D. Margraf, B. E. Bode, A. Marko, O. Schiemann and T. F. Prisner**. 2007. "*Conformational flexibility of nitroxide biradicals determined by X-band PELDOR experiments*" Molecular Physics **105** (15-16):2153–2160.

[94] **A. D. Milov, A. G. Maryasov and Y. D. Tsvetkov**. 1998. "*Pulsed electron double resonance (PELDOR) and its applications in free-radicals research*" Applied Magnetic Resonance **15** (1):107–143.

[95] **B. E. Bode, D. Margraf, J. Plackmeyer, G. Durner, T. F. Prisner and O. Schiemann**. 2007. "*Counting the monomers in nanometer-sized oligomers by*

pulsed electron - Electron double resonance" Journal of the American Chemical Society **129** (21):6736–6745.

[96] **G.F. White, L. Ottignon, T. Georgiou, C. Kleanthous, G.R. Moore, A.J. Thomson and V.S. Oganesyan**. 2007. "*Analysis of nitroxide spin label motion in a protein–protein complex using multiple frequency EPR spectroscopy*" Journal of Magnetic Resonance **185** (2):191–203.

[97] **E. Bordignon**. 2012. "*Site-Directed Spin Labeling of Membrane Proteins*", chapter 5 of Topics in Current Chemistry **321**: 121–157. Springer-Verlag Berlin, Heidelberg.

[98] **G. Jeschke and Y. Polyhach**. 2007. "*Distance measurements on spin-labelled biomacromolecules by pulsed electron paramagnetic resonance*" Physical Chemistry Chemical Physics **9** (16):1895–1910.

[99] **G. Jeschke, V. Chechik, P. Ionita, A. Godt, H. Zimmermann, J. Banham, C. R. Timmel, D. Hilger and H. Jung**. 2006. "*DeerAnalysis2006 - a comprehensive software package for analyzing pulsed ELDOR data*" Applied Magnetic Resonance **30** (3-4):473–498.

[100] **S. Stoll and A. Schweiger**. 2006. "*EasySpin, a comprehensive software package for spectral simulation and analysis in EPR*" Journal of Magnetic Resonance **178** (1):42–55.

[101] **Y. Polyhach, E. Bordignon and G. Jeschke**. 2011. "*Rotamer libraries of spin labelled cysteines for protein studies*" Physical Chemistry Chemical Physics **13** (6):2356–2366.

[102] **W. B. Mims**. 1972. "*Envelope Modulation In Spin-echo Experiments*" Physical Review B-solid State **5** (7):2409–&.

[103] **E. T. Whittaker**. 1915. "*On the functions which are represented by the expansions of the interpolation theory*" Proceedings of the Royal Society A **35** 181-194.

[104] **A. D. Milov, Y. D. Tsvetkov, F. Formaggio, M. Crisma, C. Toniolo and J. Raap**. 2000. "*Self-assembling properties of membrane-modifying pep-*

tides studied by PELDOR and CW-ESR spectroscopies" Journal of the American Chemical Society **122** (16):3843–3848.

[105] **G. Jeschke, G. Panek, A. Godt, A. Bender and H. Paulsen**. 2004. "*Data analysis procedures for pulse ELDOR measurements of broad distance distributions*" Applied Magnetic Resonance **26** (1-2):223–244.

[106] **G. Jeschke, A. Koch, U. Jonas and A. Godt**. 2002. "*Direct conversion of EPR dipolar time evolution data to distance distributions*" Journal of Magnetic Resonance **155** (1):72–82.

[107] **A. G. Maryasov and Y. D. Tsvetkov**. 2000. "*Formation of the pulsed electron-electron double resonance signal in the case of a finite amplitude of microwave fields*" Applied Magnetic Resonance **18** (4):583–605.

[108] **A. D. Milov, B. D. Naumov and Y. D. Tsvetkov**. 2004. "*The effect of microwave pulse duration on the distance distribution function between spin labels obtained by PELDOR data analysis*" Applied Magnetic Resonance **26** (4):587–599.

[109] **J. E. Banham, C. M. Baker, S. Ceola, I. J. Day, G. H. Grant, E. J. J. Groenen, C. T. Rodgers, G. Jeschke and C. R. Timmel**. 2008. "*Distance measurements in the borderline region of applicability of CW EPR and DEER: A model study on a homologous series of spin-labelled peptides*" Journal of Magnetic Resonance **191** (2):202–218.

[110] **D.J. Schneider and J. H. Freed**. 1989. "*Calculating Slow Motional Magnetic Resonance Spectra*" Biological Magnetic Resonance **8** 1-76.

[111] **Gregor Hagelueken, Richard Ward, James Naismith and Olav Schiemann**. 2012. "*MtsslWizard: In Silico Spin-Labeling and Generation of Distance Distributions in PyMOL*" Applied Magnetic Resonance **42** 377-391.

[112] **W. L. DeLano**. 2012. "*The PyMOL Molecular Graphics System*" http://www.pymol.org **Version 1.4.1** .

[113] **W. Kabsch**. 1976. "*A solution for the best rotation to relate two sets of vectors*" Acta Crystallographica A **32** 922-923.

[114] **E. F. Pettersen, T. D. Goddard, C. C. Huang, G. S. Couch, D. M. Greenblatt, E. C. Meng and T. E. Ferrin**. 2004. "*UCSF chimera - A visualization system for exploratory research and analysis*" Journal of Computational Chemistry **25** (13):1605–1612.

[115] **K. Hinsen**. 2000. "*The molecular modeling toolkit: A new approach to molecular simulations*" Journal of Computational Chemistry **21** (2):79–85.

[116] **Wendy D. Cornell, Piotr Cieplak, Christopher I. Bayly, Ian R. Gould, Kenneth M. Merz, David M. Ferguson, David C. Spellmeyer, Thomas Fox, James W. Caldwell and Peter A. Kollman**. 1995. "*A Second Generation Force Field for the Simulation of Proteins, Nucleic Acids, and Organic Molecules*" J. Am. Chem. Soc. **117** (19):5179–5197.

[117] **M.A. Larkin, G. Blackshields, N.P. Brown, R. Chenna, P.A. McGettigan, H. McWilliam, F. Valentin, I.M. Wallace, A. Wilm, R. Lopez, J.D. Thompson, T.J. Gibson and Higgins D.G.**. 2007. "*Clustal W and Clustal X version 2.0*" Bioinformatics **23** 2947-2948.

[118] **Andrew M. Waterhouse, James B. Procter, David M. A. Martin, Michèle Clamp and Geoffrey J. Barton**. 2009. "*Jalview Version 2 – a multiple sequence alignment editor and analysis workbench*" Bioinformatics **25** (9):1189–1191.

[119] **G. L. Millhauser**. 1992. "*Selective Placement of Electron-spin-resonance Spin Labels - New Structural Methods For Peptides and Proteins*" Trends In Biochemical Sciences **17** (11):448–452.

[120] **W. L. Hubbell, H. S. Mchaourab, C. Altenbach and M. A. Lietzow**. 1996. "*Watching proteins move using site-directed spin labeling*" Structure **4** (7):779–783.

[121] **W. L. Hubbell, C. Altenbach, C. M. Hubbell and H. G. Khorana**. 2003. "*Rhodopsin structure, dynamics, and activation: A perspective from crystallography, site-directed spin labeling, sulfhydryl reactivity, and disulfide cross-linking*" Membrane Proteins **63** 243–290.

[122] **Hassane S. Mchaourab, Michael A. Lietzow, Kalman Hideg and Wayne L. Hubbell**. 1996. "*Motion of Spin-Labeled Side Chains in T4 Lysozyme. Correlation with Protein Structure and Dynamics*" Biochemistry **35** (24):7692–7704.

[123] **H. S. Mchaourab, K. J. Oh, C. J. Fang and W. L. Hubbell**. 1997. "*Conformation of T4 lysozyme in solution. Hinge-bending motion and the substrate-induced conformational transition studied by site-directed spin labeling*" Biochemistry **36** (2):307–316.

[124] **Christopher D. Putnam, Michael Hammel, Greg L. Hura and John A. Tainer**. 2007. "*X-ray solution scattering (SAXS) combined with crystallography and computation: defining accurate macromolecular structures, conformations and assemblies in solution*" Quarterly Reviews of Biophysics **40** 191-285.

[125] **Christian Altenbach, Ana Karin Kusnetzow, Oliver P. Ernst, Klaus Peter Hofmann and Wayne L. Hubbell**. 2008. "*High-resolution distance mapping in rhodopsin reveals the pattern of helix movement due to activation*" Proceedings of the National Academy of Sciences **105** (21):7439–7444.

[126] **Francis J. Anscombe**. 1973. "*Graphs in Statistical Analysis*" The American Statistician **27** 17–21.

[127] **Shinji Masuda, Koji Hasegawa, Hiroyuki Ohta and Taka aki Ono**. 2008. "*Crucial Role in Light Signal Transduction for the Conserved Met93 of the BLUF Protein PixD/Slr1694*" Plant and Cell Physiology **49** (10):1600–1606.

[128] **John M. Christie, Philippe Reymond, Gary K. Powell, Paul Bernasconi, Andrei A. Raibekas, Emmanuel Liscum and Winslow R. Briggs**. 1998. "*Arabidopsis NPH1: A Flavoprotein with the Properties of a Photoreceptor for Phototropism*" Science **282** (5394):1698–1701.

[129] **Michael Salomon, Wolfgang Eisenreich, Harald Dürr, Erik Schleicher, Elke Knieb, Vincent Massey, Wolfhart Rüdiger, Franz Müller, Adelbert Bacher and Gerald Richter**. 2001. "*An optomechanical transducer in the blue light receptor phototropin from Avena sativa*" Proceedings of the National Academy of Sciences **98** (22):12357–12361.

[130] **Maxime T.A. Alexandre, Rienk Grondelle, Klaas J. Hellingwerf and John T.M. Kennis**. 2009. "*Conformational Heterogeneity and Propagation of Structural Changes in the LOV2/Jα Domain from Avena sativa Phototropin 1 as Recorded by Temperature-Dependent FTIR Spectroscopy*" Biophys J **97** (1):238–247.

[131] **Andrei S. Halavaty and Keith Moffat**. 2007. "*N- and C-Terminal Flanking Regions Modulate Light-Induced Signal Transduction in the LOV2 Domain of the Blue Light Sensor Phototropin 1 from Avena sativa*" Biochemistry **46** (49):14001–14009.

[132] **Sean Crosson and Keith Moffat**. 2001. "*Structure of a flavin-binding plant photoreceptor domain: Insights into light-mediated signal transduction*" Proceedings of the National Academy of Sciences **98** (6):2995–3000.

[133] **Roman Fedorov, Ilme Schlichting, Elisabeth Hartmann, Tatjana Domratcheva, Markus Fuhrmann and Peter Hegemann**. 2003. "*Crystal Structures and Molecular Mechanism of a Light-Induced Signaling Switch: The Phot-LOV1 Domain from Chlamydomonas reinhardtii*" Biophysical Journal **84** (4):2474–2482.

[134] **Andreas Möglich and Keith Moffat**. 2007. "*Structural Basis for Light-dependent Signaling in the Dimeric LOV Domain of the Photosensor YtvA*" Journal of Molecular Biology **373** (1):112–126.

[135] **Valentina Buttani, Aba Losi, Thorsten Eggert, Ulrich Krauss, Karl Erich Jaeger, Zhen Cao and Wolfgang Gartner**. 2007. "*Conformational analysis of the blue-light sensing protein YtvA reveals a competitive interface for LOV-LOV dimerization and interdomain interactions*" Photochem. Photobiol. Sci. **6** (1):41–49.

[136] **Brian D. Zoltowski, Carsten Schwerdtfeger, Joanne Widom, Jennifer J. Loros, Alexandrine M. Bilwes, Jay C. Dunlap and Brian R. Crane**. 2007. "*Conformational Switching in the Fungal Light Sensor Vivid*" Science **316** (5827):1054–1057.

Supplementary

Protein sequences

***T. thermophilus* DnaJ** Uniprot:Q56237, molecular mass: 30.98 kDa

10	20	30	40	50	60
MAAKKDYYAI	*LGVPRNATQE*	*EIKRAYKRLA*	*RQYHPDVNKS*	*PEAEEKFKEI*	*NEAYAVLSDP*
70	80	90	100	110	120
EKRRIYDTYG	*TTEAPPPPPP*	*GGYDFSGFDV*	*EDFSEFFQEL*	*FGPGLFGGFG*	*RRSRKGRDLR*
130	140	150	160	170	180
AELPLTLEEA	*FHGGERVVEV*	*AGRRVSVRIP*	*PGVREGSVIR*	*VPGMGGQGNP*	*PGDLLLVVRL*
190	200	210	220	230	240
LPHPVFRLEG	*QDLYATLDVP*	*APIAVVGGKV*	*RAMTLEGPVE*	*VAVPPRTQAG*	*RKLRLKGKGF*
250	260	270	280		
PGPAGRGDLY	*LEVRITIPER*	*LTPEEEALWK*	*KLAEAYYARA*		

***E. coli* DnaJ** Uniprot:P08622, molecular mass: 41.10 kDa

10	20	30	40	50	60
MAKQDYYEIL	*GVSKTAEERE*	*IRKAYKRLAM*	*KYHPDRNQGD*	*KEAEAKFKEI*	*KEAYEVLTDS*
70	80	90	100	110	120
QKRAAYDQYG	*HAAFEQGGMG*	*GGGFGGGADF*	*SDIFGDVFGD*	*IFGGGRGRQR*	*AARGADLRYN*
130	140	150	160	170	180
MELTLEEAVR	*GVTKEIRIPT*	*LEECDVCHGS*	*GAKPGTQPQT*	*CPTCHGSGQV*	*QMRQGFFAVQ*
190	200	210	220	230	240
QTCPHCQGRG	*TLIKDPCNKC*	*HGHGRVERSK*	*TLSVKIPAGV*	*DTGDRIRLAG*	*EGEAGEHGAP*
250	260	270	280	290	300
AGDLYVQVQV	*KQHPIFEREG*	*NNLYCEVPIN*	*FAMAALGGEI*	*EVPTLDGRVK*	*LKVPGETQTG*
310	320	330	340	350	360
KLFRMRGKGV	*KSVRGGAQGD*	*LLCRVVVETP*	*VGLNERQKQL*	*LQELQESFGG*	*PTGEHNSPRS*
370					
KSFFDGVKKF	*FDDLTR*				

***R. sphaeroides* BlrB** Uniprot:Q3IYE4 , molecular mass: 15.63 kDa, cofactor: FMN (0.456 kDa), FAD (0.785 kDa) or riboflavin (0.376 kDa).

10	20	30	40	50	60
MDELVSLTYR	*SRVRLADPVA*	*DIVQIMRASR*	*VRNLRLGITG*	*ILLYNGVHFV*	*QTIEGPRSAC*
70	80	90	100	110	120
DELFRLISAD	*PRHQEILAFD*	*LEPITARRFP*	*DWSMRIVSRK*	*ELRALAPDLE*	*RLDLSGPEDV*
130	140				
AELHRTIAAS	*LSKGDADASG*				

BlrB, overall ELDOR modulation depths Δ

Construct	Mutation	$\Delta(\mathrm{BlrB}_{dark})$	$\Delta(\mathrm{BlrB}_{light})$
wildtype	Q74C/K100C	0.32	0.43
wildtype	Q74C/A104C	0.32	0.45
wildtype	Q74C/S115C	0.32	0.46
wildtype	Q74C/E118C	0.30	0.43
wildtype	S58C/A129C	0.35	0.47
W92N	S58C/A129C	0.38	0.29 (–)
wildtype	E110C/A129C	0.16	0.26
W92N	E110C/A129C	0.27	0.19 (–)
wildtype	V31C/S98C	0.21	0.28
wildtype	S58C/R95C	0.35	0.52
wildtype	Q74C	0	0.21
wildtype	S98C	0	0.02 (≈0)

Table 7.1: *List of the modulation depths Δ from all ELDOR measurements.*

List of Abbreviations

μ_B	Bohr magneton, $9.27400899(37) \times 10^{-24}\mathrm{JT}^{-1}$
μ_n	nuclear magneton, $5.05078317(20) \times 10^{-27}\mathrm{JT}^{-1}$
γ	gyromagnetic ratio of the electron (or nuclear) spin
g_e	Free electron g-factor, 2.0023193043737(82)
EPR	Electon Paramagnetic Resonance
cw-EPR	continuous wave EPR, gives the derivative of the FSE spectrum
FAD	Flavin Adenin Dinucleotide
FMN	Flavin Mononucleotide
FSE	Field Swept Echo (also called ESE - electron spin echo)
FWHM	Full Width Half Maximum
hfc	hyperfine coupling
MTSL	MethaneThioSulfonate Label (also MTSSL for 'SpinLabel')
srt	shot repetition time
S/N	signal to noise ratio
W-Band	micro wave frequency from 75 to 110 GHz, typically 94 GHz
WT	wildtype
X-Band	micro wave frequency from 8 to 12 GHz, typically 9.7 GHz

Danksagung

Wissenschaft betreiben. Für mich persönlich gründet dieses Phänomen auf dem inneren Antrieb und der Bereitschaft mancher Menschen, sich persönlich und intensiv mit komplexen Fragestellungen auseinanderzusetzen und selbsteigen dessen Lösung mit voranzutreiben, auch und im Besonderen, um das eigene Verständnis jener Sache zu erweitern.

Dieser Prozess des Verstehens ist ein langer Weg, der aber manche ausgesprochen genussvolle Momente beinhaltet, wenn man eine seiner schwierigeren Etappen gemeistert hat. Auf meinem Wegstück Wissenschaft haben mich viele Leute begleitet und unterstützt, denen ich hier danken möchte.

Susanne, vielen Dank für Deine Liebe und den Rückhalt, den Du mir gegeben hast.

Christopher, es war eine sehr angenehme Zeit mit Dir im Büro.

Christoph, Deine positive Lebenseinstellung färbt ab - voll gut!

Mit Euch beiden wie mit Susanne konnte ich anregende fachliche Gespräche führen, was ich sehr genossen habe.

Ich bedanke mich bei Robert Bittl für die Gelegenheit, in seiner Arbeitsgruppe dieses Promotionsvorhaben angehen zu können, und bei Peter Hegemann für die Bereitschaft, die Zweitbegutachtung zu übernehmen.

Sylvia Luther, Roswitha Brunn, Birgit Dabisch und Christian Teutloff danke ich für ihre vielfältige Arbeit, die diese Arbeitsgruppe oft auch unsichtbar unterstützt. Ihnen und vielen weiteren Mitgliedern der Arbeitsgruppe sowie ehemaligen Kollegen danke ich auch besonders für die angenehme Arbeitsatmosphäre über die Jahre.

Dem TTL, allen voran Herrn Streuber, Herrn Christiansen und Herrn Prüfer, danke ich für ihre große Hilfsbereitschaft, den wissenschaftlichen Betrieb durch Versorgung mit Kühlmittel und auch die Bereitstellung der Studentenwerkstatt zu unterstützen. Hier hat man sich sehr willkommen gefühlt.

Einen Gruß richte ich an Ilme Schlichting und ihre Arbeitsgruppe vom MPIMF, im Einzelnen an Anikó Udvarhelyi für zahlreiche fachliche Gespräche zu BlrB. Ich drücke Dir die Daumen für Deine Arbeit. Elisabeth Hartmann für die BlrB Proben; Thomas Barends, Andrea Steinmetz und Jochen Reinstein haben das DnaJ–Thema ermöglicht. Allen meinen herzlichen Dank.

Vielen Dank an Erik Schleicher und Adelbert Bacher für die Förderung der spannenden Arbeit am deuterierten LOV. Erik, Dein durchgängiges Interesse am Fortgang meiner Arbeit hat mich sehr motiviert.

Dank an Enrica Bordignon für hilfreiche Diskussion zum Ende hin und an Tilo Mathes für Schützenhilfe in meiner Anfangsphase.

Schließlich, vielen lieben Dank an meine Freunde und meine Familie. Victoria, Papa, Tante Heide, Heike und Andi und alle anderen: Eure Motivation und Unterstützung war sehr wertvoll.